Universität Rostock

Traditio et Innovatio

Development and validation of hybrid grid-based and grid-free computational VπLES method

Dissertation

zur

Erlangung des akademischen Grades

Doktor-Ingenieur (Dr.-Ing.)

der Fakultät für Maschinenbau und Schiffstechnik
der Universität Rostock

vorgelegt von Sina Samarbakhsh, M.Sc.

geboren am 21. March 1981

in Sary (Iran)

aus Rostock

Rostock, 2022

Gutachter:

1. Gutachter

    Prof. Dr.-Ing. habil. Nikolai Kornev

    Lehrstuhl für Modellierung und Simulation (LeMoS)

    Universität Rostock

2. Gutachter

    Apl. Prof. Dr.-Ing. habil. Suad Jakirlic

    Institute of Fluid Mechanics and Aerodynamics

    Technical University of Darmstadt

Datum der Einreichung: 23.05.2022

Datum der Verteidigung: 02.09.2022

Acknowledgements

I would like to express my deep thank of gratitude to my supportive dissertation adviser Prof. Nikolai Kornev for the incredible amount of fruitful discussion and feedback on the topic of this dissertation. His deep knowledge and long experience has been invaluable throughout this study. I would like to extend my sincere thanks to my dear colleagues at the chair of modeling and simulation (LeMoS) specially room 102 for having a friendly environment during my research work.

Abstract

This dissertation presents a novel hybrid grid-based and grid-free computational method for modeling of turbulent flow. Reproducing the fine vortex structures with high resolution accuracy in turbulent flows is one of the major problems in computational fluid dynamics (CFD) due to the strong artificial dissipation of grid-based solution. The most advanced and popular technique to resolve multi scale flow structures is the large eddy simulation (LES) which is based on the idea of scale decomposition into large and small ones. While the large eddies, which are not universal, are directly resolved on the grid, the effect of small scale vortices are taken into account through a subgrid stress (SGS) model. The subgrid motion is not resolved in LES but rather it is modelled using different functional and structural approaches. However, there are many problems which require direct representation of the subgrid motion to simulate, for instance, mixing or particle dynamics in turbulent flows. In this dissertation a novel hybrid grid-based and grid-free method which is called VπLES is proposed and validated over several benchmark cases. As soon as a typical size of any fine vortex structure becomes comparable with the cell size or less than it the structure disappears due to artificial or numerical viscosity. The purpose of the new proposed method is to protect such vortices from the artificial viscosity damping inherent to grid-based techniques.

VπLES splits the flow structures into large scale ones, resolved on the grid (Eulerian approach), and small scale ones, represented by vortex particles (Lagrangian approach). Two transport equations for grid and particle solution are derived which are dynamically coupled through existence of coupling terms in each of them. There exists a permanent exchange between these two transport equations. Vortex method which is used for resolving subgrid motions in the new proposed hybrid method is suitable for modeling of fine and fast vortices. Vortex methods possess a low artificial viscosity and preserve fine vortex structures from excessive diffusion and have less restrictions to Courant number. The grid-based techniques have strong advantages in the implementation of boundary conditions, possibility for local refinement especially close to walls and availability of codes with multi physics modeling. The method resembles LES with an effort to directly reproduce the subgrid motion at least in the statistical sense.

The potential of VπLES method validated for several wall-free and wall-bounded flow benchmark cases including decay of turbulence in the cubical box, free turbulent jet flow and channel flow. A very important conclusion of validation is that the coupling term in grid-based transport equation which describes the influence of fine scales on large ones, behaves as an energy drain transferring the energy of the grid-based motion into the fine scales energy. At coarse resolutions, this coupling term acts as a diffusive LES subgrid model resulting in a LES-like behavior of the whole method. When the resolution increases, the present method is consistent and converges to the DNS. The proposed VπLES method is capable of resolving scales much less than the grid cell size. In such a way, very fine scales can be resolved on coarse grids. In case of free turbulent jet, comparison with experiments for mean velocities and fluctuations shows that the VπLES simulation with 1.5×10^5 cells attains the similar accuracy as the LES with the dynamic Smagorinsky model on the Grid with 6.04×10^6 cells. Thus, a relatively high resolution of the flow can be attained at coarse grids. The model is capable of reproducing the backward energy transfer and anisotropy of fine scales velocities. VπLES is consistent to the laminar simulation through being automatically switched off when the flow is laminar. The superior potential of VπLES method in resolving energy content in high frequency scales even in the present of huge over dissipation of coarse grid is proved in the study of channel flow case. The proposed hybrid method is simple, straightforward and utilizes advantages of grid-based and grid-free simulations.

List of publications:

- Kornev, N., Denev, J., & **Samarbakhsh, S.** (2020). Theoretical Background of the Hybrid VπLES Method for Flows with Variable Transport Properties. Fluids, 5(2), 45.

- **Samarbakhsh, S.**, & Kornev, N. (2019). Simulation of a free circular jet using the vortex particle intensified LES (VπLES). International Journal of Heat and Fluid Flow, 80, 108489.

- Kornev, N., Shevchuk, I., Abbas, N., Anschau, P., & **Samarbakhsh, S.** (2019). Potential and limitations of scale resolved simulations for ship hydrodynamics applications. Ship Technology Research, 66(2), 83-96.

- Kornev, N., & **Samarbakhsh, S.** (2019). Large eddy simulation with direct resolution of subgrid motion using a grid free vortex particle method. International Journal of Heat and Fluid Flow, 75, 86-102.

Contents

List of Figures

List of Tables

Nomenclature

Abbreviations

GS Grid scale

SGS Sub-grid scale

$V\pi LES$ Vortex particle intensified LES

VM Vortex Method

VPM Vortex Particle-Mesh

Greek symbols

β	Overlapping ratio of vortex particles	$-$
ω	Vorticity vector	s^{-1}
α_p	Vortex particle strength vector	$\mathrm{m}^3\,\mathrm{s}^{-1}$
α_q	Strength vector of old vortex particle in remeshing step	$\mathrm{m}^3\,\mathrm{s}^{-1}$
Δ	Filter width, grid size	m
η	Kolmogorov length scale	m
γ	Parameter determining the size of mapped particle to grid	$-$
Γ_p	Circulation carrying by vortex particle	$\mathrm{m}^2\,\mathrm{s}^{-1}$
μ	Dynamic viscosity	$\mathrm{kg}\,\mathrm{m}^{-1}\,\mathrm{s}^{-1}$
μ_t	Turbulent dynamic viscosity	$\mathrm{kg}\,\mathrm{m}^{-1}\,\mathrm{s}^{-1}$
ω^g	Grid-based vorticity	s^{-1}
ω^h	Discrete vorticity field	s^{-1}
ω^v	Concentrated vorticity modelled by vortex particle	s^{-1}
ψ^n	Phase angle	rad
ρ	Density	$\mathrm{kg}\,\mathrm{m}^{-3}$
σ	Vortex blob radius	m
τ_{ij}	Stress tensor	$\mathrm{kg}\,\mathrm{m}^{-1}\,\mathrm{s}^{-1}$
θ	Initial momentum thickness at the jet exit	m

Roman Symbols

$\overline{u}$	time averaged velocity	$\mathrm{m}\,\mathrm{s}^{-1}$

C_s	Smagorinsky constant	$-$
E^g	Energy spectra of grid-based large scale motions	$\mathrm{m^3\,s^{-2}}$
E^v	Energy spectra of small scale vortex particles	$\mathrm{m^3\,s^{-2}}$
h	Grid spacing, vortex blob spacing	m
k	Turbulent kinetic energy	$\mathrm{m^2\,s^{-2}}$
L	Largest scale in the system	m
l	Length of vortex particle	m
N	Number of vortex particles	$-$
N_{pt}	Maximum allowed number of vortex particles per cell	$-$
N_p	Number of injected vortex particles in computational domain	$-$
R^v_{ij}	Reynolds stress components of velocity field $\mathbf{u}^v$	$\mathrm{m^2\,s^{-2}}$
S_{ij}	Strain rate tensor	$\mathrm{s^{-1}}$
u, v, w	velocity components	$\mathrm{m\,s^{-1}}$
V_p	Vortex blob volume	$\mathrm{m^3}$
$W(x)$	Interpolation kernel	$-$
X	Normalized distance between the vortex particle and the grid node	$-$
$\mathbf{u}^g$	Grid-based velocity	$\mathrm{m\,s^{-1}}$
$\mathbf{u}^v$	velocity induced by concentrated vorticity modelled by vortex method	$\mathrm{m\,s^{-1}}$
$\mathbf{u}_p$	velocity at particle location	$\mathrm{m\,s^{-1}}$
$\mathbf{x}_p$	Vortex particle position vector	m
$\mathbf{x}_q$	Distorted position vector of vortex particle	m

1 Introduction

1.1 Motivation

Computational fluid dynamics (CFD) is a branch of fluid mechanics that uses numerical analysis and data structures to analyze and solve problems that involve fluid flows. CFD is used in a broad range of research and engineering problems in several fields of research and industrial applications including aerodynamics and aerospace analysis, hypersonics, natural science, etc. Increasingly it is becoming a vital tool in the design of industrial products and processes. In a CFD analysis, the evaluation of fluid flow including its physical properties such as velocity, pressure, temperature, density and viscosity is performed. In CFD the computational domain is sub-divided into a several smaller, non-overlapping sub-domains which is called a grid of cells (or mesh). Several errors based on the mesh structure and resolution can result in a poor CFD result. In case of too coarse mesh the proper amount of physical and chemical phenomena in a single cell can not be resolved accurately and influence the overall result. Insufficient resolution of fine vortex structures in turbulent flows is one of the key problems in CFD. The most advanced and popular technique to resolve multi scale flow structures is the Large Eddy Simulation (LES) which is based on the idea of scale decomposition into large and small ones. While the large eddies which are not universal are directly resolved on the grid, the effect of small scale vortices are taken into account through a subgrid stress (SGS) model. Since the LES became a classical topic in CFD it has been described widely in the literature. An overview of LES approach is discussed in section (2.2.2) and detailed discussion of different SGS model is skipped in this thesis and the reader is referred to the references [11], [12], [13]. The subgrid motion is not resolved in LES but rather it is modeled using different functional and structural approaches. However, there are many problems which require direct representation of the subgrid motion to simulate, for instance, mixing or particle dynamics in turbulent flows. In this thesis a novel simulation technique is proposed resembling LES with an effort to directly reproduce the subgrid motion at least in the statistical sense. It is suggested to apply a hybrid grid-based and particle-based method (or grid-free) through a combination of the finite volume and computational vortex method (VM) methods. Section (2.3.2) is devoted to the extended discussion about grid-free vortex method. In this proposed hybrid grid-based grid-free method, similar to LES the large scale field is represented on the grid, whereas the small scale one (subgrid field) is calculated using the vortex method. The new method called VπLES (vortex particle intensified LES) is a purely Lagrangian one for small scale structures and purely grid-based one (Eulerian approach) for large scale structures.

1.2 The idea of VπLES method

Due to the flow instability, which is an inherent property of turbulent flows, small scales are generated inside the velocity field represented on the grid. Small vortices can experience stretching and reduce their size. As soon as a typical size of any fine vortex structure becomes comparable with the cell size or less than it the structure disappears due to artificial or numerical viscosity. The purpose of the development of new method is to protect such vortices from the artificial viscosity damping inherent to grid-based techniques. For that, the vortices are detected in small scale velocity field and converted to vortex particles which keep their identity and are advected according to transport equations written in vorticity velocity variables. There exists a permanent exchange and a strong coupling between grid and particles representing vortices (see Fig. (1.1)).

VπLES is designed in such a way that the strengths of grid-based and grid-free schemes are combined to become complementary. Vortex method is suitable for modeling of fine and fast vortices because it introduces a low artificial viscosity and keeps the vortex particles identity. Vortex method is less restricted by Courant number. Section (2.3.2) describes the Lagrangian vortex method briefly and includes its advantages and disadvantages. For an in-depth discussion it is referred to [14], [15] and [16]. The grid-based techniques have strong advantages in treatment of boundary conditions,

possibility for local refinement especially close to walls and availability of codes with multi physics modeling.
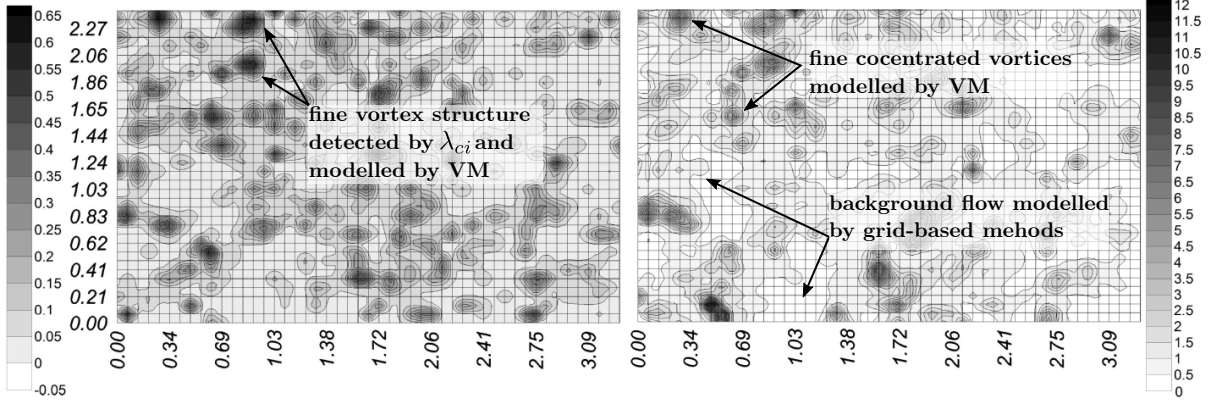
Figure 1.1: Snapshot of λ_{ci} filed (left) and the field of $\omega_z^2 / <\omega_z^2>$ within the measurement window in jet mixer, [1]. The averaged $<\omega_z^2>$ was $0.459 s^{-2}$ (right). Strong uneven distribution of ω_z^2 pointed out that the vorticity is concentrated in a relatively small number of spots or vortices.

In fact, the idea to combine the grid-based and grid-free vortex methods is not quite new. One of the most important trends in modern vortex method variants is their coupling with grid-based methods. While a part of vortex method community continue to use the traditional vortex method in a pure Lagrangian form (see e.g. [17], [18], [19], [20] and [21]), other groups (see e.g. [22], [23], [24], [25] and [26]) use hybrid vortex method with grid-based solver. This hybrid method is known as vortex-in-cell (VIC) method or vortex particle-mesh method (VPM) or semi-Lagrangian vortex method or remeshed vortex methods in various literature (see section (2.3.3) for extended description of hybrid vortex method). In VPM approach calculation of velocity from the Poisson equation, treatment of no slip boundary condition through the Brinkman penalization method and calculation of diffusion term are done using underlying grid. Only the convection of vortex elements is treated in a purely Lagrangian fashion. A uniform Cartesian grids are commonly used due to the application of Fast Fourier Transformation procedures and high order mapping (or interpolation) of flow variables from grid to particles locations and interpolation back (see Fig. (2.9)). The loss of the most important advantage of pure Lagrangian methods, i.e. the grid independence, raises discussions about the efficiency and competitiveness of VPM method with respect to common grid-based techniques which were brought to perfection by use of massive parallelism of computations. This major shift towards the use of grid is due the instability of pure Lagrangian VM simulations in three dimensional flows with concentrated vortices at high Reynolds numbers. The reason of the instability is an insufficient resolution of the vorticity enhancement and vorticity diffusion as two competitive physical processes determining the vortex dynamics. Another reason could be difficulties with efficient approximation of arbitrary vorticity fields with the bell-like or radial based functions commonly used in VM. The required number of such functions is just too high even for linearly distributed functions. As shown during the last three international conferences on vortex method in Rostock (2016), Xian (2018) and in Patras (2021) applications of the pure Lagrangian (VM) and vortex particle-mesh approaches (VPM) for viscous flows are still restricted to a narrow range of specific problems mostly at very small Reynolds numbers.

The method developed within this project is principally different from all vortex method (VM) and hybrid methods (VPM) mentioned above. In this new approach vortex method only plays a supporting role of the subgrid model and resolve only a small fraction of energetically weak vortices. Therefore, the requirements for accurate representation of vortices can be diminished in comparison with classical vortex method without any serious loss of the global accuracy of the simulation. Since the formalism is different from that of the classical vortex method method (VM and VPM), many

of vortex method weaknesses become irrelevant. The method, most similar to the present one, was proposed in [27]. The difference is that [27] considers the fine vortices as a passive phase driven by large scale motion without any interaction between them. The main objective of this thesis is to demonstrate the capability and efficiency of the $V\pi$LES method in the context of three-dimensional turbulent flow simulation resolving small scale structures. It requires the implementation the whole algorithm in OpenFOAM library which, as already demonstrated, is a high reliable open source library for CFD simulation.

1.3   Related works, Latest trends in computational vortex methods

The latest trends in the computational vortex methods were presented during 7th, 8th and 9th International Conference on Vortex Flows and Vortex Models held in Rostock-Germany 2016, Xian-China 2018 and Patras-Greece 2021 respectively. Several challenging topics in pure Lagrangian vortex method (VM) and vortex-particle mesh (VPM) and their corresponding progresses are summarized below:

1.3.1   The no-slip boundary condition

In viscous flows the solid boundaries are the key source of the creation of vorticity. Since boundary condition is typically unavailable in terms of vorticity, treating boundary condition in vortex method is complex. This issue is briefly discussed in section (2.3.2.4). Chorin in [28] and [29] presented and improved the first successful approach which is called vortex sheet/vortex blob method. This approach uses vortex splitting method in which vortex sheet creates at solid boundary to remove the slip velocity and to satisfy the no-slip boundary condition (see Fig. (2.5)). In the recent works on the vortex method presented in ICVFM conferences, the no-slip boundary condition (BC) is satisfied using the penalization technique which is based on introduction of additional artificial terms into the Navier-Stokes equation with a certain penalization parameter which should be specified from practical experience [30], [31]. The resulting equation is called the Brinkman Navier-Stokes equation. The method treats the solid and fluid in a unified and continuous manner and could be very efficient as an immersed boundary condition method for bodies with complicated geometry varying in time [32]. More traditional approach of boundary conditions implementation in vortex methods, based on original works of Wu [33] and developed later in many works (see for instance, [34]), was presented in ICVFM conferences in [35], [17], [36] and [37].

There are still remaining many problems of algorithmic and principal characters in the traditional vortex method. Among them are high costs of boundary element procedures necessary to calculate the vortex sheet on solid walls, especially in three dimensional case. With the development of penalization approach, the hybrid methods were sufficiently improved in [38], [39] and [40]. It was shown that it is possible to couple the Lagrangian and the Eulerian methods without the use of time consuming Schwartz iterative method. For that the vortex method is also used close to the wall. However employing of the vortex method close to the wall is not a proper way because of artificial noise caused by discretization of continuous vortex fields through elements which results in the spurious turbulence close to the wall. Far from the wall the discrete vortex elements are a proper and natural model for real vortex structures whereas close to the wall they could provoke nonphysical local separations. This method might work properly only at low laminar Reynolds numbers considered in the most of vortex method applications.

1.3.2   Hybrid grid-based / grid-free methods

While a part of vortex method community continue to use the traditional vortex method in a pure Lagrangian form (see e.g. [17], [18], [19], [20] and [21]) the other groups (see e.g. [22], [23], [24], [25] and [26]) consider the vortex method only with coupling with grid-based simulation within the Vortex in Cell (VIC) method or Vortex Particle mesh (VPM). This hybrid grid-based grid-free approach is discussed in details in section (2.3.3). The advantage of this technique is

that the computations of velocities are sufficiently accelerated due to application of the Poisson equation and Fast Fourier Transformation (FFT) instead of direct summation using the Biot-Savart integral, especially when Fast Multipole Method (FMM) is used only for determination of boundary conditions. Moreover, it was shown that VIC is even faster than FMM [41]. The last conclusion is important for this thesis. The scalability of the VIC method including remeshing and consideration of boundary conditions is estimated as $\mathcal{O}(N \log N)$ where N is the number of vortex particles [42]. However, the biggest weakness of this approach is the application of uniform $\Delta_x = const, \Delta_y = const, \Delta_z = const$ Cartesian grids. This contradicts to latest tendencies in grid-based method, like finite difference or finite volume ones, which are developing towards non-uniform and unstructured grids to handle flows with complex geometries. It is also proposed to map the data from uniform grids to non uniform ones when the latter is necessary, for instance, to couple with grid based solvers (in person discussion with Prof. Cottet during ICVFM2016 in Rostock/Germany). As it is known, mapping on unstructured grid is a big challenge from computational point of view and introduces additional errors. If the solution of Poisson equation (Eq. 2.91) is of the fourth order then the mapping algorithm should have the same order to keep the accuracy order of the overall procedure.

1.3.3 Stability of pure Lagrangian vortex method and the Remeshing methods

An important point of concern in vortex method is treating the term $(\boldsymbol{\omega} \cdot \nabla)\mathbf{u}$ (see Eq.(2.95)) in a pure Lagrangian way, since the analytical expressions for smoothed velocity distribution $\boldsymbol{u}$ is available and the strain rate tensor $\partial u_i / \partial x_j$ can also be calculated analytically. The term $(\boldsymbol{\omega} \cdot \nabla)\mathbf{u}$ plays a key role in the vortex dynamics and generation of the turbulence. Due to amplification mechanism this term is responsible for development of singularity $|\boldsymbol{\omega}| \to \infty$ within a finite time in inviscid vortex flows. Therefore, a correct treatment of this term in a non-diffusive way should be the key point in numerical simulations in which this term can be a source of instability and lead to breakdown of computations. High artificial viscosity of grid-based method helps to damp this instability whereas in pure Lagrangian method (VM) with low artificial viscosity it could become a big problem. One possible way to prevent the instability caused by vortex amplification is the incorporation of folding mechanism in some way into the vortex method. Due to the folding the stretched vortex filaments loss stability, create tangles and reduce their kinematic effect due to close approach of elements with opposite vorticity. This mechanism, predicted by Chorin [43], could be a reason why the kinetic energy can be kept constant despite of vorticity singularity. However, many experts of vortex methods decided to give up the idea of pure Lagrangian treatment of $(\boldsymbol{\omega} \cdot \nabla)\mathbf{u}$ and to apply the finite difference method of the fourth order on primitive uniform Cartesian grids in the context of remeshed VIC method [41]. In VπLES approach which is the main focus of this thesis the stretching equation is treated in a pure Lagrangian framework with low numerical diffusion.

1.3.4 The Remeshing methods

Remeshing is the process of redistribution of the particles, when required, to compensate for the Lagrangian distortion of the set of particles due to the high strain regions in the flow (see section (2.3.3.2.1) for more description of remeshing). It is done by interpolating the strength of vortex blobs from distorted Lagrangian grid onto a underlying uniform grid. High order remeshing is attained when it is done with Monaghan's interpolation formula M_4' [14] which can be applied only on uniform Cartesian grids, Eq. (2.90). It is claimed that the remeshing is non diffusive (see [42] and [41]). An alternative to remeshing on grid is a self-organizing adaptive resolution method (see [44] and [45]) which doesn't use a mapping into space of uniform resolution. Instead of remeshing the particles self-organize so that the position of new vortices is adjusted to approximately equidistribute the error of transport equation approximation. As mentioned in [31] the Lagrangian treatment of the convection term $\frac{D\boldsymbol{\omega}}{Dt}$, combined with the remeshing operation leads to a method with accurate treatment of the convection with negligible dispersion and excellent stability properties. Despite of the grid introduction the VIC method is classified as Lagrangian or semi-Lagrangian

approach, since the convection of vortices, i.e the terms $\partial\boldsymbol{\omega}/\partial t + (\boldsymbol{\omega}\cdot\nabla)\mathbf{u}$, are tracked in the Lagrangian way. However, the loss of the most important advantages of pure Lagrangian methods, i.e. grid independence, raises the big question about the efficiency and competitiveness of VIC with respect to common grid based techniques.

1.3.5 High Reynolds number flows

The dominating part of the vortex method application is still done for very low and moderate Reynolds numbers in laminar mode. For instance, the flow simulation around a sphere presented in [31] is performed at $Re = 1000$. The simulation, which are most interesting from the engineering point of view, were presented during ICVFM 2016 by Winckelmans and his group [40] who applied VIC for calculation of vertical axis wind turbines (VAWT). The vortex wake shed from a blade of VAWT interact with blades downstream like in case of rotor craft. Proper resolution of tip vortices is then very important to predict unsteady loadings on blades in wake. VAWT are now considered as a very promising application for vortex methods for which their advantages can play a deciding role to predict blade wake interaction.

For the overview of vortex particle-mesh (VPM) methods the reader is referred to works of Koumoutsakos [24], Cottet and Koumoutsakos [46], Winckelmans et al. (2016) [47], Mimeau [15] and Stock and Garakhani [39]. An extension of the VPM to multi phase flows can be found in Chen et al. [48]. The computational vortex particle method is far from new one and is still not so popular as other meshless and non-conventional methods like smooth partical hydrodynamics (SPH) and Lattice Boltzmann method (LBM) which made a serious progress in last decades even for engineering tasks because of availability of open-source codes. Applications of VPM for viscous flows is still restricted to a narrow range of specific problems mostly at small Reynolds numbers. Perhaps, one of the reasons is that computational particle methods generally require tuning in the process of numerical calculations, which is a know-how (Grigoryev et al., 2002 [49]) and usually not published. Instabilities and fluctuations of simulations belong to a substantial problem of particle methods, which according to Grigoryev et al. (2002) are connected with comparatively small number of model particles used in calculations. The instability of vortex method simulations of three dimensional flows with concentrated vortices at high Reynolds numbers is due to insufficient resolution of the vorticity enhancement and vorticity diffusion as two competitive physical processes determining the vortex dynamics.

In this thesis by developing a novel hybrid grid-based and grid-free Lagrangian vortex method several deficiencies of classical VM and VPM addressed earlier in section (1.3) will be solved. The newly proposed VπLES method is principally different in the mutual incorporation of grid and particle in hybrid algorithm from all existing vortex and hybrid methods. Theoretical background of VπLES method as well as its validation for several benchmark cases are described in the following chapters.

1.4 Scope of this work

A careful review of vortex method (VM) and vortex particle-mesh (VPM) showed that there is still some limitations in using vortex method for high Reynolds number in engineering applications. The main objective of this thesis is to demonstrate the capability and efficiency of the VπLES method as a novel hybrid grid-based and grid-free method with tackling the common issues in VM and VPM as mentioned in section (1.3). The demonstration is done in the context of three-dimensional turbulent flow simulation resolving small scale structures. The whole algorithm of VπLES method (see chapter 3) was implemented in OpenFOAM library which is known as high reliable open source library for CFD simulation.

This thesis is subdivided in seven chapters. First chapter is devoted to the introduction and the

motivation of this work addressing the current challenges in vortex method algorithm and the requirements of proposed new hybrid method. In the second chapter a brief review of turbulence closure modeling for numerical treatment of Navier-Stokes equation in gird-based methods is presented. Moreover the Eulerian (grid-based) and Lagrangian (grid-free) method as two numerical solution approaches of Navier-Stokes equation are reviewed. The algorithm of Lagrangian vortex method (VM) (i.e. point vortex method and vortex blob method) and vortex particle-mesh (VPM) method as popular Lagrangian (or semi-Lagrangian) approaches are presented and their main advantages and disadvantages are discussed. Third chapter describes the theoretical background and mathematical derivation of a proposed hybrid VπLES methods which is the main focus of this thesis. Fourth chapter validates VπLES method for the benchmark case of decaying of isotropic homogeneous turbulence in a cubic box and compares VπLES result with LES and under-resolved DNS. Some of the major properties of VπLES are discussed in this chapter. Fifth chapter deals with the simulation of turbulent circular jet flow using VπLES on relatively coarse grids and shows the superiority of VπLES over pure gird-based method on under-resolved grid. Chapter six evaluates VπLES method in the case of wall-bounded flows and compares the result of under-resolved grid with LES, VπLES and cases without turbulence models. The result of power spectrum shows the capability of VπLES for preserving the entity of high frequency scales in the region close to the wall. Chapter seven proposes an interesting application of VπLES method in combination with inflow generator in order to transport small scale turbulent structures to the far distance from inlet without decaying in total turbulent kinetic energy. The last chapter contains the review and conclusion about VπLES application in simulation of turbulent flows and outlooks for the future works and extensions.

2 Fundamentals of Computational Fluid Dynamics (CFD)

2.1 Governing equations: Navier-Stokes equations

Navier-Stokes equations are partial differential equations which governs the motion of viscous fluid substances. From mathematics point of view Navire-Stokes equations express the conservation of mass and conservation of momentum. They are accompanied some times by an equation of state relating pressure, temperature and density. Navier-Stokes equations describe the physics of many phenomena such as ocean current, flow around a wing, etc. By solving this equation one can obtain a flow velocity which is a vector field to every point in a fluid as well as pressure field. Experience shows that Navier-Stokes equations describe the flow of a Newtonian fluid accurately. In most cases even the simplified ones the analytical solution is not possible and one has to use numerical method. The Navier-Stokes equations are a system of nonlinear second order equations in four independent variables (velocity components u_x, u_y, u_z and pressure p) including time-dependent continuity equation for conservation of mass (Eq. (2.1)) and three time-dependent conservation momentum (Eqs. (2.2)). For a constant ν and incompressible Newtonian fluid it is given as:

$$\frac{\partial u_i}{\partial x_i} = 0 \tag{2.1}$$

$$\underbrace{\frac{\partial u_i}{\partial t}}_{\text{unsteady term}} + \underbrace{\frac{\partial (u_i u_j)}{\partial x_j}}_{\text{advection}} = \underbrace{-\frac{1}{\rho}\frac{\partial p}{\partial x_i}}_{\text{pressure gradient}} + \underbrace{\nu \frac{\partial}{\partial x_j}\left(\frac{\partial}{\partial x_j} u_i\right)}_{\text{diffusion}} + \underbrace{f_i}_{\text{external forcing}} \tag{2.2}$$

The advection term is nonlinear and must be treated with special care in numerical calculation. The diffusion term smooths out the velocity profile and has a stabilizing influence on the numerical computations. Pressure gradient includes forces on the fluid element due to spatial pressure difference and external forces consist of gravitational, electromagnetic forces,etc. The Navier-Stokes equation together with the continuity equation is a closed system of partial differential equations. The most elegant approach to solve Navier-Stokes equation is the direct numerical simulation (DNS). In order to solve equation (2.2) with DNS for a turbulent flow all flow scales from the smallest scale to the scale proportional to the physical dimensions of the problem domain must be resolved and the solution scheme is designed to minimize the numerical diffusion and dissipation error. The number of grid points in DNS is proportional to the L/η where L is the largest scale in the system and η is the Kolmogorov length scale. The resolution of time step must also be small enough to resolve the small scale fast motions. This leads to a huge computational resources and is not applicable in many industrial cases. The alternative approach to DNS is the large eddy simulation (LES) in which the contribution of large scale structures to the momentum equation is solved explicitly and the effect of small scale of turbulence is modeled (see section (2.2.2)). Hence LES can be used at much higher Reynolds numbers than DNS with less computational resources. However it still needs adequate fine grids. In most engineering application it is not required to resolve all details of the turbulent flow and information about the time-averaged properties of the flow is satisfactory. Hence, another approach specially in industrial applications of computational fluid dynamics is using time-averaged Navier-Stokes equations. In this approach the attention is paid to the numerical solution of the mean flow and the influence of turbulence on mean flow is modeled. This approach also referred as the Reynolds averaged Navier-Stokes (RANS) equations is discussed more in section (2.2.1).

2.2 Mathematical modeling of turbulent flow: Turbulence modeling

2.2.1 Reynolds Averaged Navier Stokes (RANS) equation

RANS equations are used for the approximation of the turbulent flows. It is a simplification of the Navier-Stokes equations in which each variable in the turbulent flow will be expressed as a sum

of a time-averaged value and its temporal variation. The equations are time averaged to get the equations in steady form. The time averaged value is defined as:

$$\overline{u}_i(t) = \frac{1}{2T} \int\limits_{-T}^{T} u_i dt \tag{2.3}$$

This is called Reynolds time averaging. In turbulent flow we can decompose the instantaneous variable into mean and fluctuating values:

$$u_i = \overline{u}_i + u'_i \tag{2.4}$$

$$p = \overline{p} + p' \tag{2.5}$$

Substitution of Eqs. (2.4) and (2.5) in Eq. (2.2) and use of the averaging rule results in the Reynolds averaged Navier-Stokes (RANS) equations in conservative form as follows:

$$\frac{\partial \overline{u}_i}{\partial x_i} = 0 \tag{2.6}$$

$$\rho \frac{\partial \overline{u}_i}{\partial t} + \rho \frac{\partial \overline{u}_i \overline{u}_j}{\partial x_j} = -\frac{\partial \overline{p}}{\partial x_i} + \frac{\partial}{\partial x_j} \left(\mu \frac{\partial \overline{u}_i}{\partial x_j} - \rho \overline{u'_i u'_j} \right) \tag{2.7}$$

A new term $-\rho \overline{u'_i u'_j}$ is called the Reynolds stress tensor. This is a time averaged rate of momentum transfer due to turbulence [50]. The tensor is symmetric (e.g. $\overline{u'_i u'_j} = \overline{u'_j u'_i}$) thus has six independent components and shows the correlations between velocity fluctuations. This term is unknown and thus the system of transport equations will be not closed any more. This is called the closure problem where number of unknowns are larger than the number of equations. A model must be developed for $-\rho \overline{u'_i u'_j}$ to close the system of equations for averaged flow quantities in Eq. (2.7). This model is called the closure model. The purpose of all turbulence models is to calculate the Reynolds stress tensor at all points in the flow field [50] [51] [52].

2.2.1.1 Closure models for RANS equations

Additional relations are necessary to express the Reynolds stress components through the velocities and pressure. The majority of RANS models used in engineering are based on the Boussinesq hypothesis which is the formal extension of the Newton hypothesis to turbulent flows. Boussinesq proposed to express the Reynolds stress through the strain rate tensor $S_{ij} = \frac{1}{2} \left(\frac{\partial \overline{u}_j}{\partial x_i} + \frac{\partial \overline{u}_i}{\partial x_j} \right)$ in the form of the Newton hypothesis. In the Boussinesq assumption a turbulent eddy viscosity ν_t is introduced to model Reynolds stresses [51]. The unknown Reynolds stresses are approximated by the Boussinesq hypothesis and with the help of the turbulent kinematic viscosity are expressed in the following form:

$$-\rho \overline{u'_i u'_j} = \rho \nu_t \left(\frac{\partial \overline{u}_j}{\partial x_i} + \frac{\partial \overline{u}_i}{\partial x_j} \right) - \frac{2}{3} \rho \delta_{ij} k \tag{2.8}$$

where ν_t is the turbulent viscosity or eddy viscosity. Turbulent viscosity depends on the turbulent state of the flow and is not homogeneous (i.e. it varies in space). The second term in the RHS is added to make it applicable to normal turbulent stress. δ_{ij} is the Kronecker delta and k is the turbulent kinetic energy. The turbulent closure model (Eq. (2.8)) is isotropic since the coefficient ν_t is equal for all matrix elements. Speziale and Launder constitutive relations are the extension of the Boussinesq approach for prediction anisotropic behavior in the turbulent flow [53]. The turbulence models based on this principle are called eddy viscosity models. Eddy-viscosity model are used widely in computational fluid dynamics since it is easy to implement in CFD solver. Turbulent

viscosity also contributes to the stability of the numerical simulation. Eddy-viscosity model can be categorized based on the number of the differential equations used to calculate ν_t in three different groups:

- Zero Equation Model

- One Equation Model

- Two Equation Model

The number of equations denotes the number of additional PDEs that are being to solve. Zero equation models (e.g. mixing length model) use only algebraic equations to correlate turbulent viscosity μ_t to the measured or calculated flow properties. They are suitable for the simplest flow (e.g. thin shear layer flows), easy to implement and the calculation times is short. The main problems with zero equation model are inability of describing flow where turbulent length scale varies (i.e. anything with separation or circulation) and ignoring history effects of turbulence (i.e they dont consider convective or diffusive transport of turbulence). They cannot switch from one type of region to another (e.g. from boundary layer to a free shear layer) within a single flow [54].

In one equation models one additional transport equation (PDE) and in two equation models two additional transport equations (PDEs) have to be solved. One equation models are popular in aerodynamics for computing the flow around plane wing, etc, but they show a weak performance for massively separated flows and complex internal flows. Two equation models are among the most popular turbulence models for scientific and engineering calculations. Two separate transport equations are solved to calculate the length and velocity scales. A transport equation for turbulent kinetic energy k is usually solved to determine velocity scale and any combination of k and l_0 (length scale) may be used as the second transport equation. Kolmogorov proposed a transport equation for $\sqrt{k}/l_0$ while Spalding proposed a transport equation for vorticity, k/l_0^2 [54]. The standard $k - \epsilon$ model [55] uses a transport equation for the turbulent dissipation ϵ and in $k - \omega$ model the transport equation is written for specific dissipation rate ω. Moreover, there are turbulence models which are not based on the eddy-viscosity model such as Reynolds stress models in which transport equations are solved for Reynolds stresses $\overline{u_i' u_j'}$. The most popular RANS eddy viscosity models in engineering applications are $k - \epsilon$ and $k - \omega$ SST models. A short review of $k - \omega$ SST model including its advantages and disadvantages are presented in the following section.

2.2.1.2 $k - \omega$ SST Model

Although the $k-\epsilon$ model is much less sensitive to the assumed values in the free stream, the result of $k-\epsilon$ model in near-wall region is unsatisfactory for boundary layers with adverse pressure gradient, [56] and [57]. Mentor in [56] proposed a hybrid model using $k - \omega$ model in the near-wall region and the standard $k - \epsilon$ model in the fully turbulent region away from the wall. The combination of the two models has been accomplished using a blending function. Achieving a proper blending requires a number of empirical functions such as wall-distance, which is not a desired model feature when dealing with flows in complex geometries [58]. The Reynolds stress computation and the k-equation are the same as in Wilcox 's original $k - \omega$ model, but the ϵ equation is written in terms of ω equation. The two-equation model written in conservative form reads [59]:
k-equation:

$$\frac{\partial(\rho k)}{\partial t} + \frac{\partial(\rho u_j k)}{\partial x_j} = P - \beta^* \rho \omega k + \frac{\partial}{\partial x_j}\left[(\mu + \sigma_k \mu_T)\frac{\partial k}{\partial x_j}\right] \tag{2.9}$$

ω-equation:

$$\frac{\partial(\rho \omega)}{\partial t} + \frac{\partial(\rho u_j \omega)}{\partial x_j} = \frac{\gamma}{\nu_t} P - \beta \rho \omega^2 + \frac{\partial}{\partial x_j}\left[(\mu + \sigma_m \mu_t)\frac{\partial \omega}{\partial x_j}\right] + 2(1 - F_1)\rho \sigma_{\omega^2} \frac{1}{\omega}\frac{\partial k}{\partial x_j}\frac{\partial \omega}{\partial x_j} \tag{2.10}$$

where:

$$P = min\left(\tau_{ij}\frac{\partial u_i}{\partial x_j}, 10\beta^* k\omega\right) \tag{2.11}$$

$$\tau_{ij} = \mu_t\left(2S_{ij} - \frac{2}{3}\frac{\partial u_k}{\partial x_k}\delta_{ij}\right) - \frac{2}{3}\rho k\delta ij \tag{2.12}$$

$$S_{ij} = \frac{1}{2}\left(\frac{\partial \overline{u}_j}{\partial x_i} + \frac{\partial \overline{u}_i}{\partial x_j}\right) \tag{2.13}$$

in SST model the eddy viscosity is limited in order to give improved performance in flows with adverse pressure gradients, airfoils and wake regions.

$$\mu_t = \frac{\alpha_1\rho k}{max(\alpha_1\omega, \Omega F_2)} \tag{2.14}$$

Switching between both turbulence models is done using the blending function. Without introducing a blending function there would be a numerical instability. This numerical instability results from the differences in the computed eddy viscosity away from the wall using $k - \epsilon$ model and near wall region using $k - \omega$ model. Blending functions make a smooth transition between the two models. The empirical constant β, σ_k, σ_ω are computed by a blend from the corresponding constants via the following formula.

$$\phi = F_1\phi_1 + (1 - F_1)\phi_2 \tag{2.15}$$

where ϕ_1 and ϕ_2 represent the coefficient of the $k - \epsilon$ and $k - \omega$ model respectively. Additional functions are:

$$F_1 = tanh(arg_1^4) \tag{2.16}$$

$$arg_1 = min\left[max\left(\frac{\sqrt{k}}{\beta^*\omega d}, \frac{500\nu}{d^2\omega}\right), \frac{4\rho\sigma_{\omega2}k}{CD_{k\omega}d^2}\right] \tag{2.17}$$

$$CD_{k\omega} = max\left(2\rho\sigma_{\omega2}\frac{1}{\omega}\frac{\partial k}{\partial x_j}\frac{\partial\omega}{\partial x_j}, 10^{-20}\right) \tag{2.18}$$

$$F_2 = tanh(arg_2^2) \tag{2.19}$$

$$arg_2 = max\left(\frac{2\sqrt{k}}{\beta^*\omega d}, \frac{500\nu}{d^2\omega}\right) \tag{2.20}$$

ρ is the density, ν_t is the turbulent kinematic viscosity, μ is the molecular dynamic viscosity, d is the distance from the nearest wall, F_2 is another blending function and $\Omega = \sqrt{2W_{ij}W_{ij}}$ is the vorticity magnitude with $W_{ij} = \frac{1}{2}\left(\frac{\partial u_i}{\partial x_j} - \frac{\partial u_j}{\partial x_i}\right)$. The constants are (They are revised compare to the standard $k - \omega$ model)[59]:

Table 1: Constants in $k - \omega$ SST model

β^*	β_1	β_2	σ_{k1}	σ_{k2}	$\sigma_{\omega1}$	$\sigma_{\omega2}$	α_1	k
0.09	0.075	0.0828	0.85	1.0	0.5	0.856	0.31	0.41

In spite of relative complexity and several empirical coefficients the SST model has been proved to perform well and has been adopted as a baseline eddy-viscosity model in commercial CFD package

(e.g Ansys CFX) [58]. The $k - \omega$ SST model is most general RANS model compare to Spalart-Allmaras, $k - \epsilon$ and $k - \omega$ model and test case studies show that it gives a superior performance for zero pressure gradient and adverse pressure gradient boundary layers, free shear layers and a NACA4412 airfoil [57]. The $k - \omega$ SST model is incapable of capturing the more detailed relationship between turbulent energy production and turbulent stresses caused by anisotropy of the normal stresses [57]. In order to improve the incapability of RANS models in capturing turbulent unsteadiness, there are some developments on the extending RANS closure model through formulating an instability-sensitive, eddy-resolving turbulence model on the second-moment closure level [60].

2.2.2 Large eddy simulation (LES)

In Reynolds averaged equations the resultant behavior of all eddies must be described by a single turbulence model. The smaller eddies are nearly isotropic with universal behavior (specially for high Reynolds number flows) while the large scale structures are more anisotropic and their behavior is a function of domain geometry, the boundary condition and body forces. A problem dependence of the largest eddies make it unsuccessful to achieve a general-purpose RANS model suitable for all practical applications. A different approach to overcome this deficiency is computing the larger eddies for each problem with a time-dependent simulation and modeling the smaller eddies. Considering nearly isotropic and universal behavior of small eddies makes it more amendable to predict them by a single model. This strategy is the concept of large eddy simulation (LES) approach to numerical simulation of turbulent flow [57].

LES is an intermediate technique between RANS and DNS methods. It was first proposed in 1963 by Joseph Smagorinsky [61] to simulate the atmospheric flows. In LES the large three-dimensional unsteady turbulent structures up to a given cut-off wavenumber which contain most of the energy and do most of the transporting are explicitly resolved whereas the effect of the smaller scales which have to some extent universal character are modeled. Since large scales are resolved explicitly in LES, it is expected to be more accurate than Reynolds-stress models for flows with large-scale unsteadiness motion [13].

Instead of time-averaging LES uses spatial filtering operation which is the basis rule for the separation of large (grid scale (GS)) and small scales (sub-grid scale (SGS)). The deleting small scales are said to have been cutoff and those are retained are called resolved. This filtering is a locally derived weighted average of flow properties over a fluid volume. In the following sections, a summary of the large and small scales separation, LES equations and SGS models will be presented.

2.2.2.1 Filtering

For the separation of the small dissipative scales from the large energetic turbulent structures, a spatial low-pass filtering is used. Low-pass filter removes small scale motions associated with high frequencies. The purpose of using low pass filter is smoothing high frequency turbulence smaller than a characteristic scale Δ and leaving low frequency motions which corresponds to large scales unchanged. The LES filter is a convolution filter defined for an arbitrary variable ϕ in a physical space as follow [11]:

$$\overline{\phi}(\mathbf{x}, t) = \int_{-\infty}^{+\infty} \int_{-\infty}^{+\infty} \phi(\boldsymbol{\zeta}, t') G(\mathbf{x} - \boldsymbol{\zeta}, t - t') dt' d^3 \boldsymbol{\zeta} \tag{2.21}$$

where G is the convolution kernel of the chosen filter and associated with the characteristic cutoff scale $\overline{\Delta}$ and $\overline{\tau}_c$. Δ is also called the filter width. The filtered variables are function of space and time. Similar to Reynolds's decomposition we can use filter function to decompose the arbitrary variable ϕ field. $\overline{\phi}(\mathbf{x}, t)$ is commonly known as the resolved part. $\phi'(\mathbf{x}, t)$ is the fluctuation about

this mean value and includes all scales that are smaller than the filter width Δ. $\phi'(\mathbf{x}, t)$ is commonly known as the unresolved part in LES:

$$\phi(\mathbf{x}, t) = \overline{\phi}(\mathbf{x}, t) + \phi'(\mathbf{x}, t) \tag{2.22}$$

Homogeneous filters must satisfy the following propeties when applied to the Navier-Stokes equations [11]:

- Conservation of constant, The filter doesn't change the value of a constant:

$$\overline{a} = a \iff \int_{-\infty}^{+\infty} \int_{-\infty}^{+\infty} G(\boldsymbol{\zeta}, t') dt' d^3\boldsymbol{\zeta} = 1 \tag{2.23}$$

- Linearity:

$$\overline{\phi + \psi} = \overline{\phi} + \overline{\psi} \tag{2.24}$$

- Commutation with the differentiation operator for the homogeneous filters:

$$\overline{\frac{\partial \phi}{\partial s}} = \frac{\partial \overline{\phi}}{\partial s} \tag{2.25}$$

Three most common classical filters for large eddy simulation are mentioned here. In one-dimensional case with cutoff length $\overline{\Delta}$ [11]:

- Box or top-hat filter: In finite volume method (FVM) Box-Filter is commonly used. Box filter in the physical space is defined as follows:

$$G(x - \zeta) = \begin{cases} \frac{1}{\overline{\Delta}}, & \text{if } |x - \zeta| \leq \frac{\overline{\Delta}}{2} \\ 0, & \text{otherwise} \end{cases} \tag{2.26}$$

- Gaussian filter, which has the advantage of being smooth and differentiable was introduced for LES in finite differences by the Stanford group and is written as:

$$G(x - \zeta) = \left(\frac{\gamma}{\pi \overline{\Delta}^2}\right)^{\frac{1}{2}} exp\left(\frac{-\gamma|x - \zeta|^2}{\overline{\Delta}^2}\right) \tag{2.27}$$

  where γ is a constant generally taken to be equal to 6.

- Spectral or sharp cutoff filter:

$$G(x - \zeta) = \frac{\sin(k_c(x - \zeta))}{k_c(x - \zeta)}, k_c = \frac{\pi}{\overline{\Delta}} \tag{2.28}$$

In principal the cutoff length (or cutoff width) $\overline{\Delta}$ can be chosen to have any size. The smaller the filter length is the more universal the properties of small eddies can be, but in CFD calculation with finite volume method it is meaningless to choose the cutoff length smaller than the grid size. Since in finite volume method each flow variable is calculated for each grid cell, any finer information is lost. The most common selection for cutoff length is the same order as the grid size. It is common to consider the cutoff length as a cube root of the grid cell volume thus in three dimensional computation with grid length Δx, width Δy and height Δz the cutoff width is calculated as (one choice) [57]:

$$\overline{\Delta} = \sqrt[3]{\Delta x \Delta y \Delta z} \tag{2.29}$$

The filtering process is usually acheived through the finite-volume discretization. This means no additional filtering step is done. This is called implicit filtering and the filtering is the same as the discretization. In other words the integration over the finite volume is equal to the filter volume [52].

2.2.2.2 Filtered unsteady Navier-Stokes equations

The equation of large eddy simulation is derived by applying a homogeneous filter with properties of linearity, conservation of constant and commutation with derivative to the Navier-Stokes equations. The filtered Navier-Stokes and continuity equations have the following form:

$$\frac{\partial \overline{u}_i}{\partial x_i} = 0 \tag{2.30}$$

$$\frac{\partial \overline{u}_i}{\partial t} + \frac{\partial (\overline{u}_i \overline{u}_j)}{\partial x_j} = -\frac{1}{\rho}\frac{\partial \overline{p}}{\partial x_i} + \nu \frac{\partial^2 \overline{u}_i}{\partial x_j \partial x_j} - \frac{\partial \tau_{ij}^{SGS}}{\partial x_j} \tag{2.31}$$

Eqs. (2.30) and (2.31) describe large scale motion. The contribution of small scales to the large scale transport equations appears through a subgrid scale (SGS) stress tensor τ_{ij}^{SGS} which is defined as:

$$\tau_{ij}^{SGS} = \overline{u_i u_j} - \overline{u}_i \overline{u}_j \tag{2.32}$$

Similar to RANS equations the filtered equations ((2.30) and (2.31)) are not closed and modeling the stress tensor τ_{ij}^{SGS} is necessary. The model must accurately predict the energy exchange between large and small scales that results from the interaction between different scale sizes.

2.2.2.3 The mechanism of energy exchange

In order to understand the interaction between resolved and model scales we consider the transport equation of resolved kinetic energy $k_{res} = u_i u_i$, which is a twice of total resolved energy [54]:

$$\frac{\partial \overline{k}_{res}}{\partial t} + \frac{\partial (\overline{k}_{res}\overline{u}_j)}{\partial x_j} = -2\frac{\partial \overline{pu_j}}{\partial x_j} + \frac{\partial}{\partial x_j}\left(\nu \frac{\partial \overline{k}_{res}}{\partial x_j}\right) - 2\frac{\partial \overline{\tau}_{ij}\overline{u}_i}{\partial x_j} - 2\nu \frac{\partial \overline{u}_i}{\partial x_j}\frac{\partial \overline{u}_i}{\partial x_j} + 2\tau_{ij}\overline{S}_{ij} \tag{2.33}$$

Eq. (2.33) shows that the resolved scales (grid scale) in a control volume exchange energy with the unresolved scales (subgrid scale) and surroundings. The mechanism of energy transfer includes advection (RHS), diffusion by pressure force, viscous diffusion, diffusion due to subgrid scale stresses, viscous dissipation and subgrid scale dissipation. The fourth term $(2\frac{\partial \overline{\tau}_{ij}\overline{u}_i}{\partial x_j})$ is a diffusion of resolved energy due to SGS stresses. The viscous diffusion term $(2\nu \frac{\partial \overline{u}_i}{\partial x_j}\frac{\partial \overline{u}_i}{\partial x_j})$ describes the resolved energy lost by viscous dissipation at the resolved scale level. The last term is a subgrid scale dissipation $(\epsilon_{sgs} = \tau_{ij}\overline{S}_{ij})$ which represents the net energy exchange between the resolved and the unresolved scales and can be positive (forward scatter) or negative (reverse cascade). Transfer of energy from the large scales to small scale motions is called forward scatter. In this case the subgrid scale model mimics the drain of energy from the large scales. When energy is transferred in the reversed direction $(\epsilon_{sgs} < 0)$ the backscatter happens [54]. Similar analysis will be performed for the newly developed multi-scale resolving $V\pi LES$ method in section (3.3).

2.2.2.4 Subgrid scale closure - Smagorinsky (1963) model

The Smagorinsky model is the extension of the Boussinesq approach. Smagorinsky (1963) was the first who suggested a model for anisotropic subgrid scale stresses. This model correlates τ_{ij}^{SGS} (Eq. 2.32) to the large scale strain rate tensor. The τ_{ij}^{SGS} is modeled with introducing ν_{SGS} instead of the turbulent kinematic viscosity:

$$\tau_{ij}^{SGS} - \frac{1}{3}\tau_{kk}^{SGS}\delta_{ij} \approx -2\nu_{SGS}\tilde{S}_{ij} \tag{2.34}$$

where $\tau_{kk} = \overline{u'_k u'_k}$ and $\tilde{S}_{ij} = \frac{1}{2}\left(\frac{\partial \overline{u}_j}{\partial x_i} + \frac{\partial \overline{u}_i}{\partial x_j}\right)$. Expression for the subgrid viscosity was obtained by Smagorinsky with the use of idea taken from the Prandtl mixing length theory. According to

Prandtl, the turbulent kinematic viscosity is proportional to the magnitude of strain rate tensor S_{ij} and to a certain length l_s squared:

$$\nu_{SGS} = l_S^2 |\tilde{S_{ij}}| \tag{2.35}$$

The length l_s is assumed to be proportional to the mesh size $l_s = C_s \Delta$. Here C_s is a Smagorinsky constant and Δ is the filter width or grid scale. Thus the SGS viscosity is evaluated as follows:

$$\nu_{SGS} = (C_s \Delta)^2 |\tilde{S_{ij}}| \tag{2.36}$$

This model relies on the local equilibrium of production dissipation of sub-grid scales. Lilly (1966, 1967) performed a theoretical analysis of the decay rates of isotropic turbulent eddies in the inertial subrange of the energy spectrum, which suggests values of C_s between 0.17 and 0.21 but there is no C_s universally applicable to different type of flow [57]. Difficulty with transitional (laminar) flows and necessity of adding a damping function in order to damp the SGS viscosity near the wall are the shortcoming of this model.

Very important characteristic of LES models is that they are consistent with the increasing of grid resolution (i.e $\Delta \to 0$). If the grid resolution is increased in order to resolve the smallest scale in motion the LES equation is converged to the original Navier-Stokes equations and the SGS stresses disappear. On the contrary the URANS simulation is not consistent when $\Delta \to 0$ and the Reynolds stress components do not disappear [51]. Similar to LES the same characteristic will be seen with VπLES approach and will be discussed in more details in section (4.5).

2.3 Numerical solution of governing equations

2.3.1 Grid-based Finite volume method (FVM)

This section briefly reviews the cell-centered finite volume (or control volume) method (FVM) which is used in grid-based solver as well as Eulerian part of hybrid Eulerian/Lagrangian solver of this thesis to solve conservation Eqs. (2.1) and (2.2) numerically. FVM is based on discretizing the integral form of the governing equations over each control volume. FVM method probably is the most popular approach for engineering applications compared to other approaches such as finite difference method (FDM), finite element method (FEM) and spectral method. Main advantages of FVM are the compatibility with unstructured grid in complex geometry and the integral formulation of conservation laws (the native form of conservation laws are integral). Moreover, FVM is the used method in the OpenFOAM toolkit. The procedure of the discretization can be split into two parts: discretization in time and space (temporal and spatial discretization) which has been thoroughly studied during the last decades. Therefore, only a small overview of this discretization will be provided in this section. The review of FVM discretization in the following section is mostly adopted from the work of Professor Jasak, one of the two original co-authors of OpenFOAM, [62]. The standard form of the generic transport equation of physical quantity ϕ (scalar) is defined as:

$$\underbrace{\frac{\partial \rho \phi}{\partial t}}_{\text{Temporal}} + \underbrace{\nabla \cdot (\rho \mathbf{U} \phi)}_{\text{Convection}} - \underbrace{\nabla \cdot (\rho \Gamma_\phi \nabla \phi)}_{\text{Diffusion}} = \underbrace{S_\phi(\phi)}_{\text{Source}} \tag{2.37}$$

where ϕ is the transported variable (e.g. velocity, pressure, mass, ...), ∇ is the Nabla operator, $\mathbf{U}$ is the velocity vector, Γ_ϕ is the diffusion coefficient and $S_\phi(\phi)$ is the source term. This is a second-order partial differential equation due to the second derivative of ϕ in space in the diffusion term. In the FVM, the transport equation (2.37) must be written in the integral form over control volume V_p around point P (see Fig. (2.1)) and time t:

$$\int_t^{t+\Delta t} \left[\frac{\partial}{\partial t} \int_{V_P} \rho\phi dV + \int_{V_P} \nabla \cdot (\rho \mathbf{U}\phi) dV - \int_{V_P} \nabla \cdot (\rho\Gamma_\phi \nabla\phi) dV \right] dt$$
$$= \int_t^{t+\Delta t} \left(\int_{V_P} S_\phi(\phi) dV \right) dt \tag{2.38}$$
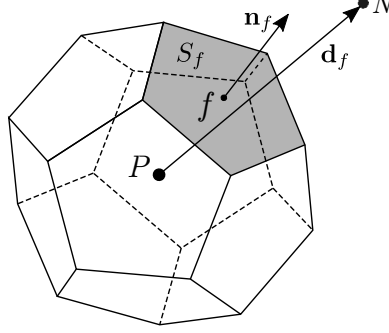
Figure 2.1: Polyhedral shaped control volume cell (adopted from [2]).

For a satisfying accuracy, it is very important that the order of the discretization be equal to or higher than the order of discretized equation. For the spatial discretization, the generalized form of the Gauss' theorem will be used, which reads:

$$\int_V \nabla\phi dV = \oint_{S_V} d\mathbf{S}\phi \tag{2.39}$$

$$\int_V \nabla \cdot \mathbf{a} dV = \oint_{S_V} d\mathbf{S} \cdot \mathbf{a} \tag{2.40}$$

where S_V is the closed surface bounding the volume V and $d\mathbf{S}$ presents an infinitesimal surface element with associated outward pointing normal on S_V. This equation can be transformed into a sum of integrals over all faces, taking into account that the control volume is bounded by a series of flat faces:

$$\int_{V_P} \nabla \cdot \mathbf{a} dV = \oint_{S_V} d\mathbf{S} \cdot \mathbf{a} = \sum_f \left(\int_f d\mathbf{S} \cdot \mathbf{a} \right) \tag{2.41}$$

whereas the subscript f represents the value of the variable (here, $\mathbf{a}$) in the middle of the face (see Fig. (2.1)). Assuming the linear variation of the function ϕ in time and space:

$$\phi(\mathbf{x}) = \phi_P + (\mathbf{x} - \mathbf{x}_P) \cdot (\nabla\phi)_P \tag{2.42}$$

$$\phi(t + \delta t) = \phi^t + \Delta t \left(\frac{\partial\phi}{\partial t} \right)^t \tag{2.43}$$

where:

$$\phi_p = \phi(\mathbf{x}_P) \tag{2.44}$$

$$\phi^t = \phi(t) \tag{2.45}$$

The face integral in the Eq. (2.41) can be written as:

$$\int_f d\mathbf{S} \cdot \mathbf{a} = \left(\int_f d\mathbf{S} \right) \cdot \mathbf{a}_f + \left[\int_f d\mathbf{S}(\mathbf{x} - \mathbf{x}_f) \right] : (\nabla\mathbf{a})_f = \mathbf{S} \cdot \mathbf{a}_f \tag{2.46}$$

15

and finally leads to:

$$\int_{V_p} \nabla \cdot \mathbf{a} dV = \oint_{S_V} d\mathbf{S} \cdot \mathbf{a} = \sum_f \left(\int_f d\mathbf{S} \cdot \mathbf{a} \right) = \sum_f \mathbf{S} \cdot \mathbf{a} \qquad (2.47)$$

In the rest of the text, the discretization of each term in the transport equation (2.37) will be briefly presented.

2.3.1.1 Discretization of the convection term

Using last Eq. (2.47), the approximation of the convective volume flux through the faces is defined as:

$$\int_{V_p} \nabla \cdot (\rho \mathbf{U} \phi) dV = \int_{S_V} d\mathbf{S} \cdot (\rho \mathbf{U} \phi) = \sum_f \mathbf{S} \cdot (\rho \mathbf{U} \phi)_f = \sum_f \mathbf{S} \cdot (\rho \mathbf{U})_f \phi_f = \sum_f F \phi_f \qquad (2.48)$$

where F is the mass flux through the faces of the control volume and is equal to:

$$F = \mathbf{S} \cdot (\rho \mathbf{U})_f \qquad (2.49)$$

It is assumed that F is calculated from the interpolated values of ρ and $\mathbf{U}$. The value of the variable ϕ at the faces is required in Eq. (2.48) and obtained with convection differencing scheme. A detailed review of convection differencing schemes and their properties such as accuracy and boundedness can be found in [57], [62] and [63]. The convection differencing scheme is going to calculate the value of ϕ at the face from the value in the cell centers. To overcome the requirement of high computational cost, the calculation of ϕ in differencing scheme is limited to only the nearest neighbors of the control volume.
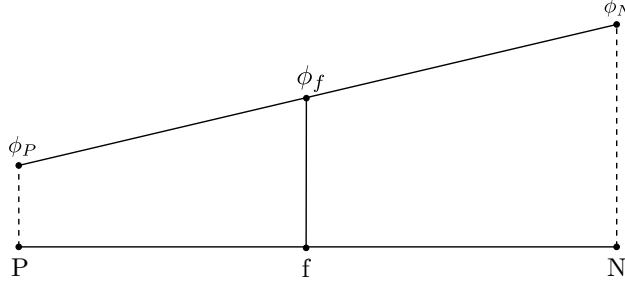
Figure 2.2: Face interpolation using central differencing scheme for the value ϕ.

Considering the linear variation of ϕ between neighboring point P and N in Fig. (2.2), the value of ϕ at face reads:

$$\phi_f = \phi_P \gamma_f + \phi_N (1 - \gamma_f) \qquad (2.50)$$

where γ_f is the interpolation factor and is defined for a one-dimensional case as:

$$\gamma_f = \frac{\mathbf{x}_N - \mathbf{x}_f}{\mathbf{x}_N - \mathbf{x}_P} \qquad (2.51)$$

The differencing scheme based on Eq. (2.50) is known as central differencing scheme (CDS). Ferziger and Péric (1996) [63] show that the CDS is of second-order accuracy and can be applied for structured and unstructured meshes. However, the CDS can reproduce unphysical oscillations when the convection is the dominate term in the problem. To avoid the unphysical large oscillations and keep the boundedness, the first-order schemes like the Upwind Differencing Scheme (UDS) in which the value ϕ_f is determined according to the direction of the flow is an alternative discretization scheme:

$$\phi_f = \begin{cases} \phi_f = \phi_P & \text{for } F \geq 0 \\ \phi_f = \phi_N & \text{for } F < 0 \end{cases} \tag{2.52}$$

The flow fields will be drastically smoothed due to the boundedness of the solution in UDS, which in turn leads to an increasing diffusion and that can violate the order of accuracy of the discretization and distort the solution. One way to avoid both the boundedness and the numerical oscillations is using the blended differencing scheme (BDS) which is a blend of UDS and CDS.

2.3.1.2 Discretization of the diffusion term

The diffusion term of the transport equation can be discretized in a similar way with the assumption of the linear variation of ϕ as follows:

$$\int_{V_p} \nabla \cdot (\rho \Gamma_\phi \nabla_\phi) dV = \int_{S_V} d\mathbf{S} \cdot (\rho \Gamma_\phi \nabla_\phi) = \sum_f \mathbf{S} \cdot (\rho \Gamma_\phi \nabla \phi)_f = \sum_f (\rho \Gamma_\phi)_f \mathbf{S} \cdot (\nabla \phi)_f \tag{2.53}$$

The surface normal gradient of ϕ can be calculated using the values at the points P and N of the neighboring cells for an orthogonal grid in which vector $\mathbf{d}$ and $\mathbf{S}$ in Fig. (2.3) are parallel, as follow:

$$\mathbf{S} \cdot (\nabla \phi)_f = |\mathbf{S}| \frac{\phi_N - \phi_P}{|\mathbf{d}|} \tag{2.54}$$
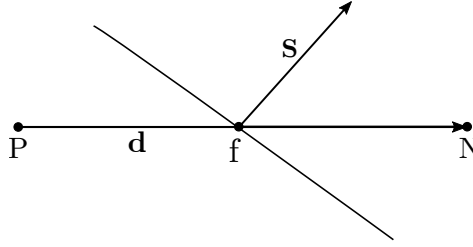
Figure 2.3: Representing vector $\mathbf{S}$ and $\mathbf{d}$ in non-orthogonal mesh

Above method is a second order accurate on orthogonal mesh. An explicit correction will be used in the calculation of the gradient of ϕ which is described in detail by Ferziger and Péric [63].

2.3.1.3 Discretization of the source term

All terms of the transport equation that cannot be classified as convective, diffusive or temporal terms, are consequently treated as sources. The source term should be linearized before the discretization:

$$S_\phi(\phi) = S_u + S_P \phi \tag{2.55}$$

where S_u and S_P can be a function of ϕ. Hence, the discretization of source term with using volume integral over a CV gives:

$$\int_{V_p} S_\phi(\phi) dV = S_u V_P + S_p V_P \phi_P \tag{2.56}$$

It is advised to treat source term in an implicit manner. Further discussion about proper treating source term is explained in [62].

2.3.1.4 Temporal discretization

So far only the spatial discretization were presented. With respect to Eqs. (2.53), (2.56) the Eq. (2.38) can be rewritten as:

$$\int_t^{t+\Delta t}\left[\left(\frac{\partial\rho\phi}{\partial t}\right)_P V_P + \sum_f F\phi_f - \sum_f(\rho\Gamma_\phi)_f\mathbf{S}\cdot(\nabla\phi)_f\right]dt$$
$$= \int_t^{t+\Delta t}(S_u V_P + S_P V_P\phi_P)dt \tag{2.57}$$

This equation is usually called the "semi-discretized" form of the generic transport equation. Assuming the linear variation of the function ϕ, the temporal integral and the time derivative can be written as:

$$\left(\frac{\partial\rho\phi}{\partial t}\right)_P = \frac{\rho_P^n\phi_P^n - \rho_P^o\phi_P^o}{\Delta t} \tag{2.58}$$

$$\int_t^{t+\Delta t}\phi(t)dt = \frac{1}{2}(\phi^o + \phi^n)\Delta t \tag{2.59}$$

where

$$\phi^n = \phi(t + \Delta t) \tag{2.60}$$

$$\phi^o = \phi(t) \tag{2.61}$$

By assumption of constant density and diffusivity in time:

$$\frac{\rho_P\phi_P^n - \rho_P\phi_P^o}{\Delta t}V_P + \frac{1}{2}\sum_f F\phi_f^n - \frac{1}{2}\sum_f(\rho\Gamma_\phi)_f\mathbf{S}\cdot(\nabla\phi)_f^n$$
$$+ \frac{1}{2}\sum_f F\phi_f^o - \frac{1}{2}\sum_f(\rho\Gamma_\phi)_f\mathbf{S}\cdot(\nabla\phi)_f^o \tag{2.62}$$
$$= S_u V_P + \frac{1}{2}S_p V_P\phi_P^n + \frac{1}{2}S_p V_P\phi_P^o$$

The above expression of the temporal discretization is called Crank-Nicholson method and is a second order accurate scheme in time. There are several explicit and implicit methods for the temporal discretization which can be found in [62]. In the case of the explicit time discretization, there is a limit to the applied time step which is restricted to Courant-Friedrichs-Lewy (CFL) number defined as [20]:

$$Co = \frac{\Delta t|u|}{\delta x} \tag{2.63}$$

This number is a criterion of the numerical stability, if Co number is larger than unity, the explicit system becomes unstable.

2.3.1.5 Finite volume method in OpenFOAM

The framework OpenFOAM (Open source Field Operation And Manipulation) is a free C++ library which developed primarily by OpenCFD Ltd at ESI Group since 2004. This framework is based on the object-oriented programming that can be used to develop wide range of computational solver for problems in continuum mechanics with a focus on finite volume discretization. OpenFOAM has a broad range of features to solve governing equations of complex fluid flow including turbulence and heat transfer. The best advantage of the OpenFOAM is the free access to the source

code in order to develop and implement new CFD algorithms. Therefore, one can easily modify the functions of any object, turbulence models, boundary conditions, numerical solvers ..etc, and then easily implement the new code using the present source and existing base classes in OpenFOAM. OpenFOAM uses operator overloading that allows algorithm to be expressed in the natural way. The discretization of transport equation for a generic scalar ϕ in OpenFOAM is expressed as:

$$\underbrace{\frac{\partial \rho \phi}{\partial t}}_{\text{Temporal}} + \underbrace{\nabla \cdot (U\phi)}_{\text{Convection}} - \underbrace{\nabla \cdot (\Gamma_\phi \nabla \phi)}_{\text{Diffusion}} = \underbrace{P\phi}_{\text{Source}} \tag{2.64}$$

```
(
          fvm::ddt(phi)
+         fvm::div(mDot, phi)
-         fvm::laplacian(Gammaphi, phi)
==
          fvm::Sp(P, phi)
);
```

The fvm::div operator consider the convective flux as a coefficient field over the faces of control volumes and generic variable phi as a cell centered variable and returns a system of equations including left hand side (LHS) matrix and right hand side (RHS) source as representation of the discretization of convection operator. Similar LHS matrices and RHS vectors are calculated for other operators and add or subtract to each other in order to create the final system of discretized algebraic equations defined over each control volume of the computational domain [64]. The above listing shows the flexibility and simplicity of the implementation and extension of new libraries in OpenFOAM. This makes OpenFOAM a superior choice for customization compared to other commercial CFD software packages. In this thesis OpenFOAM in addition to an extensive development for the Lagrangian treatment of the terms in Eq. (3.13) and coupling algorithm with grid-based solver is the main tool for the presented numerical results.

2.3.2 Grid-free Lagrangian vortex method

2.3.2.1 General definition and governing equations
Vortex method (VM) is a numerical approaches for solving Navier-Stokes equations in the velocity-vorticity form. It was first introduced for inviscid and unbounded flow problem and then extended to viscous and bounded flows. The development of vortex motion in fluid flow is responsible for some fascinating aspects of fluid mechanics, such as mixing, shearing, transport and hydrodynamics instability. Many incompressible flows can be characterized by regions of concentrated vorticity embedded in irrotational fluid. The inviscid motion of these concentrated vorticity in these regions is given by the local fluid velocity which in turn is determined kinematically from the vorticity field. Thus it is mathematically correct to consider inviscid fluid dynamics in terms of parcels of vorticity which induce motion on each other. The situation is analogous to the gravitational field induced by the planets. The mass of the solar system is concentrated in relatively few places and it is easier to focus on the position and strength of these masses at any time rather than calculating gravitational field at any point in space. This approach leads to reduction of mathematical description of essential components [65]. In a simple words if the flow is incompressible, knowledge of vorticity distribution is enough to determine the velocity field [66]. This is the principal idea behind the development of vortex methods and its consistent development as an alternative to Eulerian grid-based approach.

Traditionally flow is described by the Navier-Stokes equations in terms of flow velocity and pressure at any point. Vortex methods belong to Lagrangian methods (also called particle methods) and it is more convenient to solve compressible Navier-Stokes equations in velocity-vorticity formulation

19

where vorticity is defined as the curl of velocity, $\boldsymbol{\omega} = \nabla \times \mathbf{u}$. The velocity-vorticity formulation of the Navier-Stokes equation reads:

$$\frac{\partial \boldsymbol{\omega}}{\partial t} + \mathbf{u} \cdot \nabla \boldsymbol{\omega} - \boldsymbol{\omega} \cdot \nabla \mathbf{u} - \nu \Delta \boldsymbol{\omega} = 0 \tag{2.65}$$

$$\nabla . \mathbf{u} = \mathbf{0} \tag{2.66}$$

One of the advantages of this formulation is decoupling of pressure term from the evolution equation therefor the equations are only depends on velocity and vorticity.

2.3.2.2   Introduction to vortex method

Based on the idea behind vortex method the vorticity field can be approximated by a set of point elements. These point elements often referring to vortex particles (also known as vorton) carries around a given amount of vorticity. The continuous vorticity field $\boldsymbol{\omega}$ can be approximated by a discrete vorticity field $\boldsymbol{\omega}^h$ at time t as a sum of the vorticities of the vortex elements:

$$\boldsymbol{\omega}(\mathbf{x}, t) \approx \omega_0^h = \sum_p \boldsymbol{\alpha}_p \eta(\mathbf{x} - \mathbf{x}_p(t)) \tag{2.67}$$

where $\mathbf{x}_p$ is a position vector. $\boldsymbol{\alpha}_p$ is the initial local strength around particle p centered at $\mathbf{x}_p$ and is defined as the product of the vorticity by the particle volume $\boldsymbol{\alpha}_p = V_p \boldsymbol{\omega}_p$. The core function η has to satisfy the normalized distribution:

$$\int \eta(\mathbf{x}) d\mathbf{x} = 1 \tag{2.68}$$

The simplest model for core function is the delta-Dirac function δ. In spite of the simplicity of delta-Dirac function there is an issue of singularity when particles are very close to each other. To avoid this problem a smoothed finite sized particles with core size σ was introduced which is known as vortex blob method, originally introduced by Chorin and Bernard [28]. In this approach a vorticity of each particles distributed on a blob like a sphere (disk in 2D) with finite radius σ. For the vortex blob method the discrete vorticity is given by:

$$\boldsymbol{\omega}(\mathbf{x}, t) \approx \omega_0^h = \sum_p \boldsymbol{\alpha}_p \zeta_{\sigma_p}(\mathbf{x} - \mathbf{x}_p(t)) \tag{2.69}$$

Gaussian distribution is an ideal choice for smoothing function ζ_p (cutoff function), because of its smoothness property, its radial symmetry and its fast decay. Fig. (2.4) shows a two dimensional representation of ζ_p with Gaussian distribution given as:

$$\zeta_p(\mathbf{x}) = \frac{1}{k \pi \sigma^2} exp\left(-\frac{|\mathbf{x}|^2}{k \sigma^2}\right) \tag{2.70}$$

where the constant k is the width of cutoff function and is chosen between 1, 2 or 4.
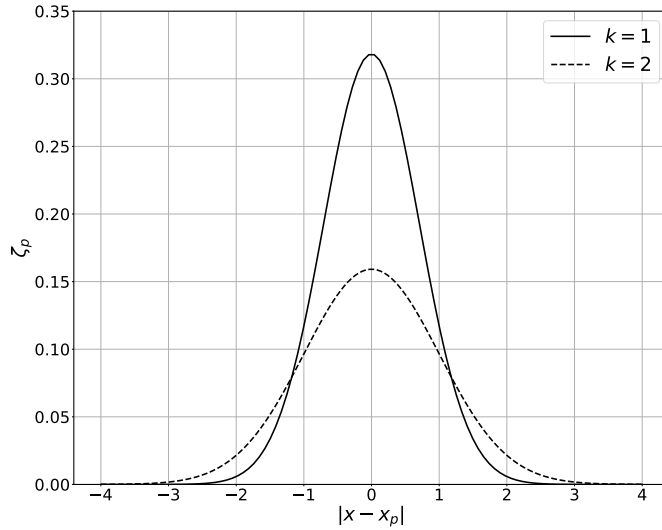
Figure 2.4: Gaussian distribution of smoothing function for k=2 and σ=1 (2D function)

In the majority of vortex methods it is assumed that the vortex element is being convected without deformation with the local velocity. In order to recover the velocity field from vorticity field the Biot-Savart integral is being used [67], [68]:

$$\mathbf{u}(\mathbf{x}, t) = \int (\nabla \times \mathbf{G})(\mathbf{x} - \mathbf{x}')\boldsymbol{\omega}(\mathbf{x}', t)d\mathbf{x}' \tag{2.71}$$

$$\mathbf{u}(\mathbf{x}, t) = \int \mathbf{K}(\mathbf{x} - \mathbf{x}')\boldsymbol{\omega}(\mathbf{x}', t)d\mathbf{x}' = (\mathbf{K} * \boldsymbol{\omega})(\mathbf{x}, t) \tag{2.72}$$

where $\mathbf{K} = \nabla \times \mathbf{G}$ is a Biot-Savart kernel, G is the Green 's function of three-dimensional Laplace operator and $*$ means convolution. The standard Bio-Savart law in three-dimension is written as follows:

$$\mathbf{u}(\mathbf{x}, t) = (\mathbf{k} * \omega)(\mathbf{x}, t) = \frac{1}{4\pi} \int \frac{\omega(\mathbf{x}', t) \times (\mathbf{x} - \mathbf{x}')}{|\mathbf{x} - \mathbf{x}'|^3} d\mathbf{x}' \tag{2.73}$$

Replacing the standard Biot-Savart kernel in Eq. (2.73) with the smoothed (mollified) kernel gives the following relations for calculating the discrete induced velocity field:

$$\mathbf{K}_\sigma = \mathbf{K} * \zeta_\sigma \tag{2.74}$$

$$\mathbf{u}(\mathbf{x}, t) = \sum_p \boldsymbol{\alpha}_p(t)\mathbf{K}_\sigma(\mathbf{x} - \mathbf{x_p(t)}) \tag{2.75}$$

The Lagrangian formulation of the (inviscid) vortex method in three dimensions is expressed with Eqs. (2.79) and (2.80). The numerical particle locations and the local strengths are obtained by solving the following ODEs [14], [16]:

$$\frac{d\mathbf{x}_p}{dt} = \mathbf{u}(\mathbf{x}, t) \tag{2.76}$$

$$\frac{d\boldsymbol{\alpha}_p}{dt} = \boldsymbol{\alpha}_p.\nabla\mathbf{u}(\mathbf{x}_p, t) \tag{2.77}$$

$$\mathbf{u} = \mathbf{K}_\sigma * \boldsymbol{\omega} \tag{2.78}$$

Since vortex methods are inherently inviscid some additional steps are needed to model viscosity. In a time marching method a common approach is to consider the inviscid and viscous parts of

the equation one after the other in substeps. This algorithm is known as viscous splitting. Prandtl introduced this classical concept for distinguishing the viscous and inviscid phenomena in the flow and Chorin formulated viscous splitting approach for vortex methods [14]. For an unbounded flow in the first substep vortices move with the local velocity which was obtained with the Biot-Savart law and the particles locations are updated. In this substep vortex stretching changes the vorticity carrying by each vortex particles. Diffusion effects are considered in the second substep. The viscous splitting algorithm in Lagrangian frame can be given as follow:

- convection:

$$\frac{d\mathbf{x}_p}{dt} = \mathbf{u}(\mathbf{x}, t) \tag{2.79}$$

$$\frac{d\boldsymbol{\alpha}_p}{dt} = \boldsymbol{\alpha}_p . \nabla \mathbf{u}(\mathbf{x}_p, t) \tag{2.80}$$

- diffusion:

$$\frac{d\mathbf{x}_p}{dt} = 0 \tag{2.81}$$

$$\frac{d\boldsymbol{\alpha}_p}{dt} = \nu \Delta \boldsymbol{\alpha}_p + B.C \tag{2.82}$$

The advantage of viscous splitting algorithm is that one can apply different models and approaches for each substeps while only investigate the phenomena involving in that specific substep.

2.3.2.3 Model of viscosity: Core spreading method (CSM)

In vortex method the viscous effect needs to be modeled explicitly. Several diffusion models have been developed so far in order to solve equation (2.82). According to Barba [67] at least seven different schemes were designed to add viscous diffusion effect in the context of Lagrangian framework to vortex method. As the most popular one random vortex method (RVM), core spreading method (CSM), particle strength exchange (PSE) and diffusion velocity method (DVM) can be named [16]. In this thesis core spreading model (CSM) has been used in the newly developed hybrid grid-based grid free method (VπLES) and explained shortly here.

The core spreading method use spreading Gaussian blobs around particles while their circulation remains constant. The core spreading method (core expanding) first presented by Kuwahara and Takami [69] and reformulated by Leonard [66] is a purely Lagrangian approach which considers the influence of viscosity by changing the core size of the particle. Core spreading method directly consider the exact solution of diffusion equation (Eq. (2.82)) given by the Green's function solution:

$$\boldsymbol{\omega}(\mathbf{x}, t) = \frac{\boldsymbol{\alpha}_p}{(4\pi\nu t)^2} exp\left(-\frac{|\mathbf{x} - \mathbf{x}_p|}{4\nu t}\right) \tag{2.83}$$

Diffusion equation can be discretized with the approximation of continuous vorticity field by superposition of discrete vortex blobs in which the cutoff function ζ_{σ_p} distributes the vorticity over blob size σ. If the Gaussian distribution is chosen for cutoff function ζ_p it gives:

$$\zeta_{\sigma_p}(\mathbf{x}) = \frac{1}{2\pi\sigma^2} exp\left(-\frac{|\mathbf{x}|^2}{2\sigma^2}\right) \tag{2.84}$$

then the discretized scheme in Eq. (2.69) reproduces the solution of diffusion equation (Eq. (2.82)). Comparing Eq. (2.84) with Green's function solution Eq. (2.83), the core spreading vortex method

is then formulated to satisfy identically the viscous part of the vorticity equation by expanding the Gaussian blob distribution in time according to $\sigma^2 = 2\nu t$. It means that in order to satisfy the diffusion equation the core of each particle must expand (spread out) at each time step at a rate of $\sqrt{\nu \Delta t}$. In the other word the diffusion of each vortex particle in this method is obtained by linear time growth of σ^2:

$$\frac{d\sigma^2}{dt} = 4\nu \tag{2.85}$$

and can be rewritten in following simple algorithm:

$$\sigma_i^2(t + \Delta t) = \sigma_i^2(t) + 2\nu\Delta \tag{2.86}$$

Core spreading method is inexpensive and simple for implementation, fully localized and grid free in nature and fully deterministic. This method is not necessarily rely on viscous splitting approach. However the original implementation of core spreading method was declared inconsistent and could only give a converged approximation of Navier-Stokes equations with a very restrictive limit of vanishing viscosity. The reason for this inconsistency is the growth of particle size at least to $\sqrt{\nu T}$ in a simulation until to a final time T which is not in agreement with the convergence criterion of vortex method. The convergence of vortex method depends on remaining core size σ as a small parameter. Rossi [70] developed a CSM with correction step and proposed vortex splitting and merging. The merging is a mean to control the problem size as splitting increases the vortex blob numbers. Yokota et al. [71] applied the CSM with correction for study of 3D isotropic turbulence [67], [16].

2.3.2.4   Boundary condition treatment

Application of vortex method for bounded flow needs the satisfaction of boundary condition at wall. No-slip boundary condition exerts a torque to the fluid elements adjacent to the wall leading to the rotational motion in the fluid. Hence in viscous flows the solid boundaries are the key source of the creation of vorticity. The challenge is that no-slip boundary condition is expressed based on the velocity field while vortex method is based on the vorticity formulation of Navier-Stokes equation. To formulate boundary condition for vortex method both Dirichlet formulation (wall vorticity) or Neumann formulation (wall-normal vorticity flux) is possible. Neumann $\frac{\partial \boldsymbol{\omega}}{\partial \mathbf{n}}$ is often preferred since it explicitly expresses the local production of vorticity at solid boundaries (walls) [14], [16]. According to [16] boundary condition can be categorized in three main groups. The first group belongs to pure Lagrangian methods and is based on viscous splitting and mimics the vortex creation at the interface by generation of vortex sheet. The other two groups include underlying grid thus often used with vortex-particle-mesh (VPM) approach. Chorin in [28] and [29] presented and improved the first successful approach which is called vortex sheet/vortex blob method. This approach uses vortex splitting method in which vortex sheet creates at solid boundary to remove the slip velocity and satisfy the no-slip boundary condition (see Fig. (2.5)). To do so the wall discretized into different segment. Each segment represents a local slip velocity where vortex element creating at each time steps is designed to remove this velocity. In the original version of Chorin 's approach [28] the removal of velocities at the walls was achieved by generating vortex blobs instead of vortex sheets. The vortex blob on the boundary introduces an artificial smoothing region for the vorticity field near the surface which increase remarkably the total numerical dissipation of the method. To reduce this problem Chorin [29] introduced vortex sheet method based on a coupling of the Prandtl boundary layer equation near the surface with Navier-Stokes equations away from it. One can mention the limitation of Prandtl approximation which is only valid for attached flows as the main limitation for Chorin 's Method. The details of vortex sheet/vortex blob algorithm and its improvement can be found in [14], [15], [28] and [29].
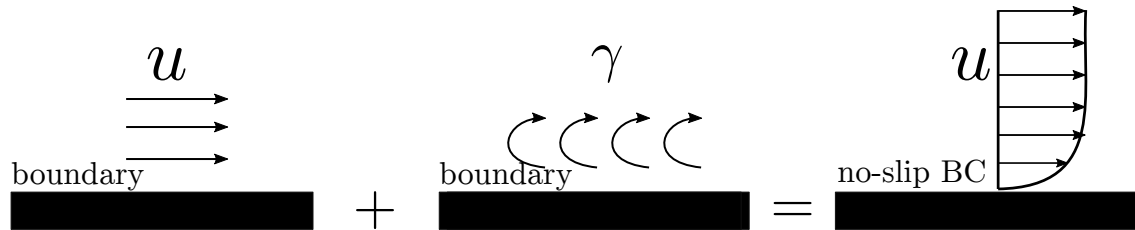
Figure 2.5: Schematic view of Chorin's vortex sheet method to mimic the no-slip boundary condition in vortex method.

2.3.2.5 Velocity computations in vortex methods: Biot-Savart integral solution approaches

The Biot-Savart integral equation (2.73) calculates the local velocity of each vortex particle using other particle locations and strength. It can be calculated in two different Lagrangian ways:
Direct calculation of Biot-Savart integral: Due to the global influence of vortex particles on the computational domain a direct integration is very time consuming and for N number of particles $\mathcal{O}(N^2)$ operations is required in each time step which has known as a N-body problem. This is inappropriate for large value of N which would be a case in three dimensional turbulence. One solution would be considering a cutoff distance and ignore the particles locating beyond this distance [72]. Although it reduces the number of operations, might be inconsistent in term of conserving total vorticity.

Fast Multiple Method (FMM): Greengard and Rokhlin [73] proposed a fast summation algorithm for particle simulations. The main idea behind FMM method is clustering particles at various spatial length and calculate the interaction between clusters which are located far away. Interaction between neighboring particles is treated directly. FMM algorithm reduces the number of direct particle particle interaction by replacing distant particles by multipole expansions of groups (see Fig. (2.6)). The algorithm divides a domain filled with particles scattered in arbitrary order in to the rectangular sub-domains. Each sub-domains again is divided into the smaller domains until each cell contains a given maximum number of particles. This approach is based on tree data structure and can reduce the computational cost to $\mathcal{O}(N)$. Parallel implememtation of FMM have widely developed and used with Lagrangian vortex methods [74]. FMM keeps the grid-free nature of vortex method at the cost of some complexity in implementation.
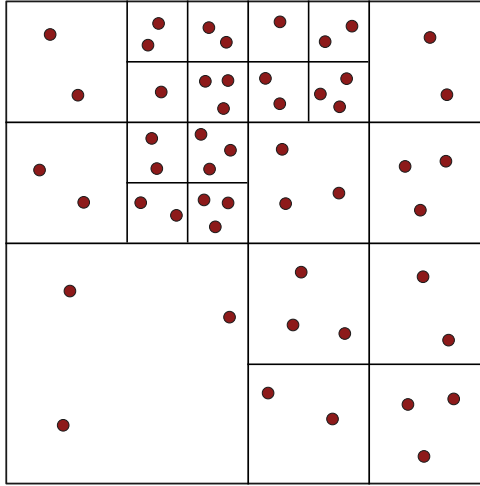
Figure 2.6: FMM block structure with the limit of maximum three particles per cell (adopted from [3]).

2.3.2.6 Basic building blocks of vortex method (VM)

Based on the description of vortex method algorithm in the previous sections the following diagram represents the flowchart of any viscous vortex method. The arrows shows the sequence of different steps in a time-marching algorithm:
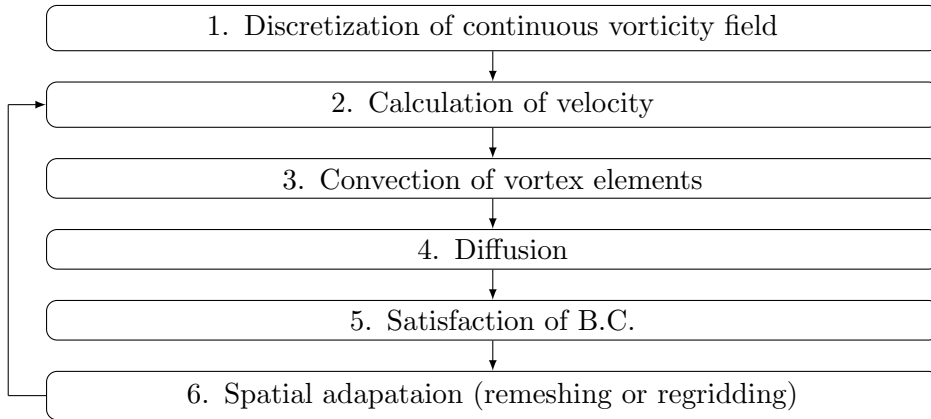
Figure 2.7: Basic steps of a viscous vortex method

The first step is dealing with the distribution of continuum vorticity field to the discrete vortex blobs (see section (2.3.2.2)). The next block is velocity evaluation by using discrete Biot-Savart law or FMM [73] as an efficient solution to N-body problem. Convection step is done in the Lagrangian fashion by accurate time dicretization scheme such as Runge-Kutta forth order scheme and choosing an appropriate time step with respect to the flow characteristic and required accuracy [67]. In order to model the viscous diffusion effect several models have been named in section (2.3.2.3) and CSM was reviewed shortly. Spatial adaption in vortex method would be necessary due to the clustering or dispersion of vortex particles. Spatial adaption in the form of remeshing will be discussed later in section (2.3.3.2.1).

Vortex method as was explained here have several advantages over traditional Euler (grid-based) scheme. As might be expected there are aslo several side effects or disadvantages cited in various literature [16], [67]. One can mention the following items as advantages of vortex method:

- Due to Lagrangian treatment of advection term the fine scale structures can often be convected accurately and preserved for a larger time step.

- In the vortex method formulation the pressure term is decoupled from the evolution equations in incompressible flow.

- Vorticity field is a compact field compared to the velocity field, this helps vortex method to focus on the areas of vorticity and saves resources from neglecting irrotational part of the domain.

- Vortex method is much less restricted by Courant-Friedrichs-Lewy (CFL) condition compared to the Eulerian method. Hence larger time step compared to grid-based method is allowed in vortex method. In vortex method time step is only related to velocity gradient $\Delta t \leq \frac{C}{||\nabla \mathbf{u}||_\infty}$, where C is a constant less than or equal to one [15].

- In vortex method far field boundary condition can be treated precisely and an accurate outflow boundary condition which is easy to implement is available [66].

Development and improvement in the original algorithm vortex methods have not been a standard or mainstream tools of CFD. The following points can be mentioned as main limitations for vortex method to be not involved in the mainstream of CFD community:

- High computational cost for calculating the velocity with Biot-Savart law referred to N-body problem discussed in section (2.3.2.5). Development of fast summation algorithm such as Fast Multiple Method (FMM) [73] requiring an amount of work proportional to N has treated this difficulty to some extent.

- Complexity of modeling viscous effect in a Lagrangian framework. Diffusion term is more appropriate to solve with grid-based methods.

- Lost of accuracy due to the distortion of vortex particle in high strain region of flow is often observed and the necessity of using spatial adaption scheme (or remeshing) at the cost of some numerical diffusion and appearance of oscillatory results is inevitable.

- Treatment of no-slip boundary condition is much more complex compared to grid-based method (section 2.3.2.4).

- Deficiency in high Reynolds number due to numerical instability which arises from treating stretching term in Lagrangian fashion. In order to converge the simulation the vorticity field must be redistributed to a large number of vortex particles and these particle must keep the overlapping for the all time of the simulation. The convergence condition $h = \mathcal{O}(\sigma)$ is observed by [75] in their investigation of propagation and stability of three dimensional vortex ring where h is the particle spacing and σ is the vortex blob radius. Thus in high Re number the simulation cost is more than available resources.

According to Leonard [66] it is up to the practitioner to make a benefit of the advantages while finding ways to tackle the disadvantages.

2.3.3 Hybrid Vortex method

Hybrid numerical method combines Lagrangian grid-free vortex methods with Eulerian grid-based method to various extent. In hybrid scheme Lagrangian and Eulerian framewrok are combined in the same or separate part of the domain. Each method with respect to its advantages and capabilities can be used to discretize different terms of governing equation. Also the numerical diffusion induced by grid improves the stability of the numerical simulation. Eulerian grid is used to take the benefit of the prescription of the no-slip boundary conditions as well as solving the velocity Poisson equation and modeling the diffusion term while the particle overlapping criteria

is ensured. Lagrangian framework is used for solving advection term. Main difference between various approaches in hybrid vortex method is based on how particle or grid contribute in the hybrid algorithm. Two types of hybrid Eulerian-Lagrangian method are reviewed in this chapter briefly.

2.3.3.1 Domain decomposition method

Based on the idea of using grid method and Lagrangian method in different part of the computational domain the popular domain decomposition method was first proposed by Cottet in 1991 [76]. Domain decomposition method uses grid-based scheme in the region close to the immersed obstacle in order to implement accurate constrains for boundary conditions. On the other hand the Lagrangian approach is applied in the remaining region of domain to accurate modeling of advection-diffusion effects. Farfield boundary conditions are also satisfied using vortex method. The coupling between subdomains relies on Schwartz alternating method where the boundary condition on each subdomain are obtained iteratively and transfer information between two frame work is being performed. Fig. (2.8) shows the schematic view of a typical domain decomposition method with overlapping. There are two overlapping domain Ω_1 for grid-based method and Ω_2 belongs to pure vortex method. S_1 and S_2 are the outer boundary of Ω_1 and inner boundary of Ω_2.
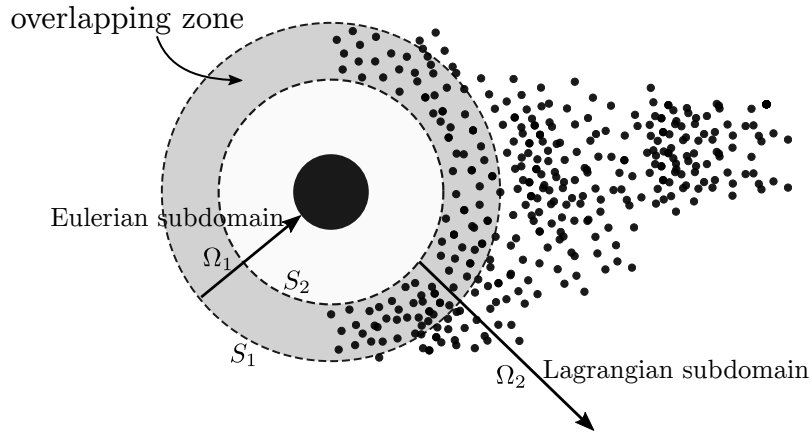
Figure 2.8: Domain decomposition method (adopted from [4]).

Based on [14] and [15] a very short description of the classical framework of domain decomposition techniques for partially overlapping domain is presented here. With respect to the viscous splitting in the first substep the Poison equation for the velocity $\Delta \psi = -\boldsymbol{\omega}$ and in the second subset the convection-diffusion equation are solved (Eq. (2.65)). It is assumed that the vorticity is known in both grid domain Ω_1 and on the particles in Ω_2 domain. In domain decomposition method the Schwartz alternating method is commonly used for solving Poisson equation. It solves alternatively the Poisson equation in Ω_1 and Ω_2. Each domain uses the stream function value obtained in the other domain at the preceding iteration as a boundary condition. It first calculate the solution of Poisson equation on Ω_1 with boundary condition on S_1 calculated in Ω_2 at the previous iteration and then calculate the solution in Lagrangian domain Ω_2 with boundary condition S_2 obtained in Ω_1 at the current iteration. After Schwartz algorithm convergence the convection-diffusion equation is solved in each domain. More comprehensive description of each steps of domain decomposition approach can be seen in [14], [15], [76], [77]. Another type of hybrid vortex method known as vortex-in-cell (VIC) method was first proposed by [78]. A review of main aspects of vortex-in-cell method is presented in the following section.

2.3.3.2 Vortex-in-cell method VIC

As an alternative method to pure Lagrangian vortex method Christiansen [78] proposed vortex-in-cell (VIC) method. VIC is so called hybrid Eulerian-Lagrangian approach using both framework according to their strengths. The Eulerian framework (underlying grid) is used to compute particle velocities and diffusion term and Lagrangian method is used for calculating the advection of particles. VIC calculates the velocity as a field from the Poisson equation instead of the individual element velocities as direct Biot-Savart integration would produce. Main four steps which are common in VIC methods include: particle to grid mapping (or assigning), solving equations on the underlying grid, grid to particle mapping (or interpolation) (see Fig. 2.9) and Lagrangian advection of particle. Based on the specific implementation the outline of VIC algorithm is summarized as follow:

1. **Solving Poisson equation using underlying grid:**

   (a) assigning (or redistributing) particle vorticity value to the underlying grid using particle to mesh mapping with any redistribution formula:

   $$\boldsymbol{\omega}_i = \frac{1}{V_i} \sum_p \boldsymbol{\Gamma}_p W\left(\frac{\mathbf{x}_p - \mathbf{x}_i}{h}\right) \tag{2.87}$$

   where $\mathbf{x}_p$ is the position of the particle carrying the circulation $\boldsymbol{\Gamma}_p$, $\mathbf{x}_i$ is the position of the ith interpolation node, V_i is the volume of the grid cell centered at x_i, $W(x)$ is the interpolation kernel whose properties determine the type and quality of the interpolation. The kernel must satisfy the conservation of the total circulation as measured on the particles and grid (Eq. (2.88)) and also conservation of linear and angular impulse (Eq. (2.89)).

   $$\sum_i \omega_i V_i = \sum_p \Gamma_p \tag{2.88}$$

   $$\sum_i W\left(\frac{\mathbf{x} - \mathbf{x}_i}{h}\right) \equiv 1$$

   $$\sum_i x_i W\left(\frac{\mathbf{x} - \mathbf{x}_i}{h}\right) \equiv x \tag{2.89}$$

   $$\sum_i x_i^2 W\left(\frac{\mathbf{x} - \mathbf{x}_i}{h}\right) \equiv x^2$$

   The third order accurate, piecewise smooth interpolation scheme which is known in literature as M_4' is widely used in VIC literature. The kernel is continuously differentiable and satisfies the conservation of first three moments of the particle distribution (total circulation, linear and angular impulse). Monaghan [5] proposed and improved this interpolation formula as:

   $$M_4'(X) = \begin{cases} \frac{1}{2}(2 - 5X^2 + 3X^3), & \text{if } 0 \leq X \leq 1 \\ \frac{1}{2}(1 - X)(2 - X)^2, & \text{if } 1 < X \leq 2 \\ 0 & \text{otherwise} \end{cases} \tag{2.90}$$

   where X is the distance between the particle and the grid node normalized by grid spacing, h. A fraction of the particle quantities which is assigned to the grid node is given by M_4'. The M_4' kernel has a width of four in 1D meaning that a particle information is being assigned onto four grid nodes. The extension of 1D representaion of equation (2.92) in 2D and 3D is performed with tensor product of 1D schemes in each direction $W(x) = \prod_{n=1}^d W(x_{(k)})$. As expected the use of such interpolation provide some numerical or subgrid dissipation which essentially remedied the divergence issue [14], [79], [38].

(b) computing the induced velocity by solving the Poisson equation on the grid:

$$\Delta \mathbf{u} = -\nabla \times \boldsymbol{\omega} \qquad (2.91)$$

2. **Lagrangian treatment of Advection**:

    (a) interpolating the calculated velocity field from grid to particles locations with formula:

    $$\mathbf{u}_p = \sum_p \mathbf{u}_i W \left(\frac{\mathbf{x} - \mathbf{x}_i}{h} \right) \qquad (2.92)$$

    (b) advection of particles in a Lagrangian fashion and calculate their new positions and vorticity:

    $$\frac{d\mathbf{x}_p}{dt} = \mathbf{u}_p \qquad (2.93)$$

    $$\frac{d\boldsymbol{\omega}}{dt} = 0 \qquad (2.94)$$

    (c) assigning (back interpolation) the vorticity values and vortex elements volumes to the grid using equation(2.87).

3. **Stretching or tilting of vortex particle vorticity**:

    (a) using underlying grid to solve the stretching term in the Eulerian framework:

    $$\frac{\partial \boldsymbol{\omega}}{\partial t} = (\boldsymbol{\omega}.\nabla)\mathbf{u} \qquad (2.95)$$

4. **Solving diffusion equation using Eulerian framework**

    (a) using underlying grid to solve the diffusion equation and update the vorticity field on the grid

    $$\frac{\partial \boldsymbol{\omega}}{\partial t} = \nu \Delta \boldsymbol{\omega} \qquad (2.96)$$

    (b) interpolate the updated vorticity from grid to particles using back interpolation.

The order of accuracy of VIC method rely on the order of accuracy of each scheme used for each sub-steps. The Poisson equation in step 1 is often handled with Fast Fourier Transform (FFT) method or Fast Multiple Method (FMM). VIC method also known nowadays as the vortex particle-mesh method (VPM) in the literature. After several time steps particles have a tendency to accumulate in area where velocity gradient is very high. This may lead to spurious vortex structure. The remeshing or regridding (see section (2.3.3.2.1)) relocates the particle in the grid points and solve this problem at the cost of adding interpolation error. VIC method variants uses different remeshing procedure. Remeshing can be done at each time step or every 5th, 10th, ... time steps.

As a summary it can be noticed that VIC has some advantages similar to vortex method such as less restriction to CFL condition and also treating the advection term in Lagrangian fashion. There are also some advantages in using VIC method over pure Lagrangian vortex method which is given as:

- Computation of viscous effect using grid-base schemes (e.g. finite difference method) is more accurate in comparison to Lagrangian model for viscous term.

- In VIC method Fast velocity evaluation is possible using fast Poison solver instead of direct summation with Biot-Savart integral.
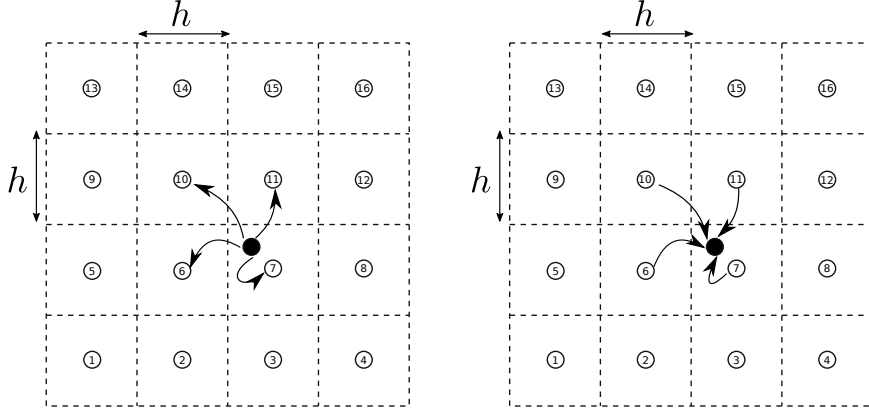
(a) particle to grid mapping (or assigning) (b) grid to particle mapping (or interpolation)

Figure 2.9: Communication of particle information with underlying grid.

2.3.3.2.1 Remeshing

In vortex method overlap criterion is defined as a ratio between particle spacing h and core size σ. According to convergence properties of vortex method with finite core it is essential that the particle must overlap ($h < \sigma$) at all times although it can be relaxed to some extent (see Fig. (2.11)). This condition might not hold in practice because of the clustering and dispersion of vortex blobs due to the high strain regions in the flow. This situation results in the loss of the accuracy in vortex method because of destroying the communication between particles. A common solution for this issue is regular spatial adaptation or remeshing (or regridding) of particles with conservation of physical invariants to retain the proper distribution. Remeshing restarts the particle field on a underlying Cartesian grid where the overlapping condition is satisfied. It is done by interpolating the strength of vortex blobs from distorted Lagrangian grid onto a underlying uniform grid [67], [14], [80]. The strength of the blobs on new grid α_p is obtained by interpolation of the circulation carried by the old particles as:

$$\boldsymbol{\alpha}_p = \sum_q \tilde{\boldsymbol{\alpha}}_q W \left(\frac{\mathbf{x}_p - \tilde{\mathbf{x}}_q}{h} \right) \tag{2.97}$$

With equation (2.97) new particles at location $\mathbf{x}_p$ on a uniform grid with spacing h and with strength $\boldsymbol{\alpha}_p$ are obtained from old particles with strength of blobs $\tilde{\boldsymbol{\alpha}}_q$ on the distorted Lagrangian grid $\tilde{\mathbf{x}}_q$. The interpolation kernel must satisfy the conservation of the first three moments of particle distribution (see Eqs. (2.88), (2.89)). M_4' interpolation kernel is widely used in literature for remeshing. Time scale for remeshing should be larger than the time step for the particle advection but in practice it is conducted every few time steps and often every time step [16]. Several side effects of remeshing techniques have also mentioned in literature. Remeshing induces some numerical errors in VIC approach. It is observed that the subgrid scale effect of remeshing facilitates underresolved calculations. Remeshed particle simulations in particular with high order finite difference schemes shows some problems related to oscillations in result. Some work such as [81] has been done for developing a non-oscillatory remeshing scheme for vortex particle.

(a) $h < \sigma$, overlap criterion has been fulfilled (b) $h > \sigma$, overlap criterion has been broken

Figure 2.10: The overlap criterion is essential for accuracy of vortex method.

(a)

(b)
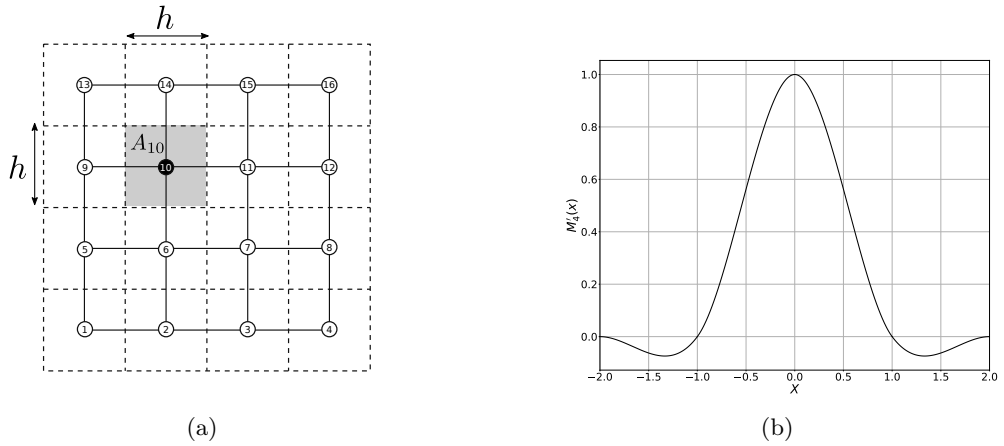
Figure 2.11: a) Grey area is the area assigned to the particle number 10, redistribution of particle 10 is done with M'_4 interpolation into 16 nodes in 2D Cartesian grid using Eq. (2.90). b)M'_4 interpolation scheme by Monagan [5]

2.3.3.2.2 Basic building blocks of VIC method

One time step in the original version of VIC by [78] can be summarized as Fig. (2.12) from step 1 to 5. In the improved version of VIC method in order to avoid the clustering and dispersion of vortex particles an addition step for spatial adaptation (remeshing or regridding) is necessary. The improved algorithm is also called remeshed VIC method in some literature.
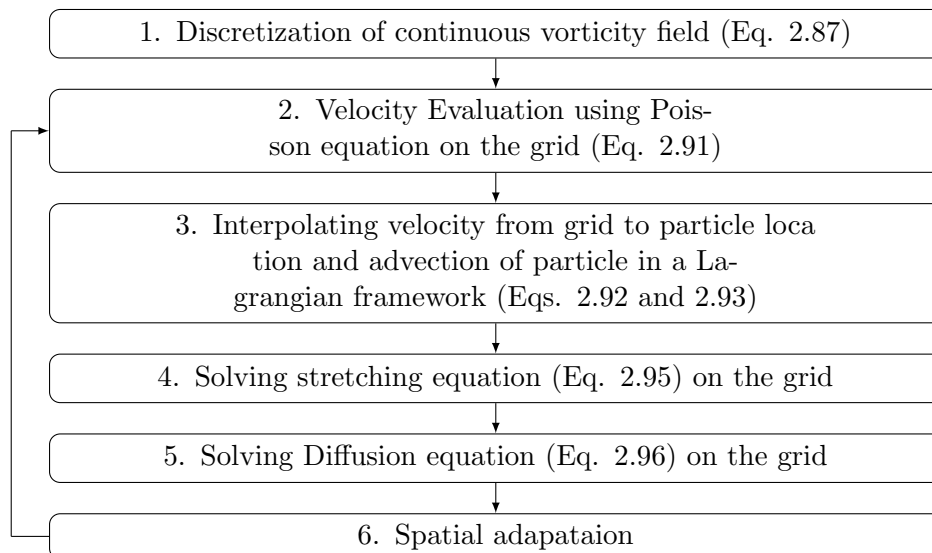
Figure 2.12: Basic steps of a viscous remeshed Vortex in Cell (VIC) method

In the next chapter a novel hybrid grid-based and grid-free method which is principally different form all other hybrid methods from point of view of combination of particle-based (or grid-free) and grid-based simulation is proposed and its physical and mathematical derivation is presented.

3 Hybrid grid-based and grid-free vortex method, VπLES

In this chapter a novel hybrid grid-based grid-free method is introduced. The method is based on the decomposition of the velocity and vorticity fields into the distributed large scale and concentrated small scale motions similar to the first step in LES approach. The large scale field is represented on the grid, whereas the small scale one is calculated using the grid-free computational vortex method. The method is a pure Lagrangian one for small structures and pure grid-based one for large scale structures. The simulation with vortex method (VM) is embedded into the grid-based simulation and are dynamically coupled. There exists a permanent exchange between grid and particle represented vortices. The idea of the method is illustrated in Fig. (3.1) where the vorticity squared ω_z^2 is presented for a confining jet flow. Study of turbulent structures was performed using high resolved PIV [82]. Regardless of initial conditions in turbulent flow and Reynolds numbers which were sufficiently different the following features of flow structures were documented in [82]:

- The vorticity is represented mostly by fine concentrated vortices and their clusters. Existence of large strong vortices was not observed. Only a small fraction of fine vortex structures contributes to the total enstrophy.

- Fine strong vortices of the turbulent flow at high Reynolds numbers are distributed very unevenly in space. They are approximately axisymmetric.

These facts confirm plausibility of the following concepts and assumptions for developing the new hybrid technology. With operator splitting method one can split a partial differential equation into less complex parts solved then sequentially. In the context of this novel hybrid method the Navier-Stokes equation is split with respect to the size of flow structure using velocity decomposition. The velocity decomposition techniques was already presented by Beale [83] in order to split the Navier-Stokes equation into the Stokes part and regular part. The idea behind the new proposed hybrid method is to decompose the velocity filed into the velocities induced by the concentrated vortex structure $\mathbf{u}^v$ and background (or grid-based) velocities $\mathbf{u}^g$.
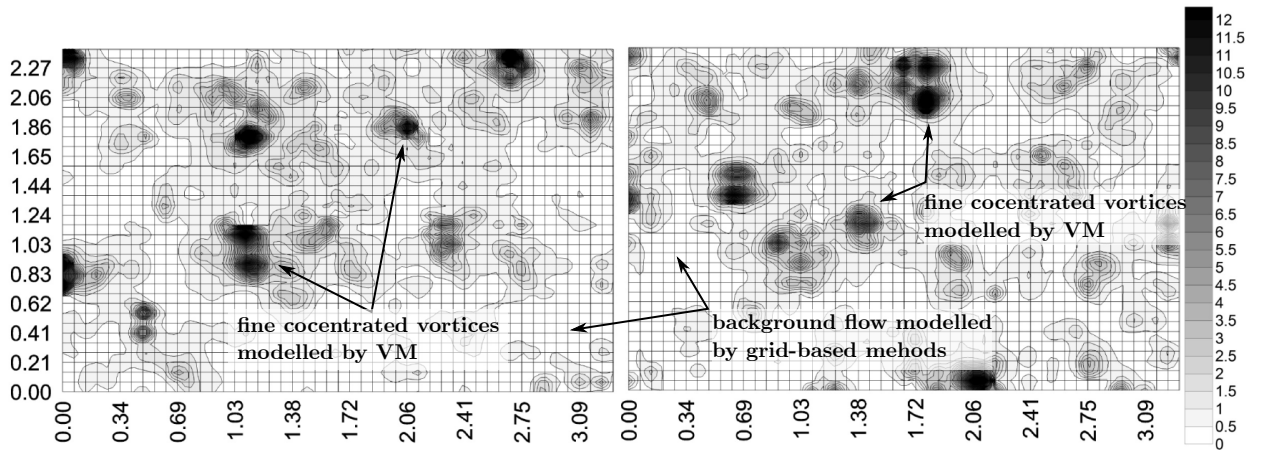
Figure 3.1: Snapshot of the field $\omega_z^2 / < \omega_z^2 >$ within the measurement window in jet mixer. The averaged $< \omega_z^2 >$ was $1.19s^{-2}$ and $0.459s^{-2}$, respectively [1].

3.1 Decomposition of Navier-Stokes equations

The governing equations are derived using the splitting procedure. The operator splitting method widely used in numerical analysis dates back to 1950th [84]. In the computational fluid mechanics splitting is commonly based on two principles [85]: splitting according to physical processes (consecutive individual treatment of convection, diffusion, pressure term, etc.) or splitting according to coordinate directions (see, for instance, alternating direction implicit ADI approach [86]). In this work the splitting of Navier Stokes equation into a system of two coupled transport equations

according to scales is proposed. Following this approach the Navier-Stokes equation can be split into a part which represent the concentrated vortex velocities solved by Lagrangian approach (or grid-free method) and a part for background velocities solved by Eulerian approach (or grid-based method) such as finite volume method. Based on physical concept which is illustrated in Fig. (3.1) velocity and vorticity field can be represented by a sum of concentrated (superscript v) and background part (superscript g):

$$\mathbf{u}(\mathbf{x}, t) = \mathbf{u}^g(\mathbf{x}, t) + \mathbf{u}^v(\mathbf{x}, t)$$
$$\boldsymbol{\omega}(\mathbf{x}, t) = \boldsymbol{\omega}^g(\mathbf{x}, t) + \boldsymbol{\omega}^v(\mathbf{x}, t) \tag{3.1}$$

Substituting the decomposed velocity and vorticity in to the vorticity transport equation (2.65) gives:

$$\frac{\partial(\boldsymbol{\omega}^g + \boldsymbol{\omega}^v)}{\partial t} + ((\mathbf{u}^g + \mathbf{u}^v) \cdot \nabla)(\boldsymbol{\omega}^g + \boldsymbol{\omega}^v) = ((\boldsymbol{\omega}^g + \boldsymbol{\omega}^v) \cdot \nabla)(\mathbf{u}^g + \mathbf{u}^v) + \nu\Delta(\boldsymbol{\omega}^g + \boldsymbol{\omega}^v) \tag{3.2}$$

equation (3.2) is split to the tranport equation for grid-based vorticity ω^g and vorticity transport equation for grid-free method ω^v:

$$\frac{\partial\boldsymbol{\omega}^g}{\partial t} + ((\mathbf{u}^g + \mathbf{u}^v) \cdot \nabla)\boldsymbol{\omega}^g = (\boldsymbol{\omega}^g \cdot \nabla)(\mathbf{u}^g + \mathbf{u}^v) + \nu\Delta\boldsymbol{\omega}^g \tag{3.3}$$

$$\frac{\partial\boldsymbol{\omega}^v}{\partial t} + ((\mathbf{u}^g + \mathbf{u}^v) \cdot \nabla)\boldsymbol{\omega}^v = (\boldsymbol{\omega}^v \cdot \nabla)(\mathbf{u}^g + \mathbf{u}^v) + \nu\Delta\boldsymbol{\omega}^v \tag{3.4}$$

original velocity $(\mathbf{u}^g + \mathbf{u}^v)$ transports the vorticity in both equation. Eq. (3.3) should be written in $u - p$ formulation in order to solve with traditional finite volume methods. Using vector identity as:

$$(\mathbf{u}^g \times \boldsymbol{\omega}^g) = \mathbf{u}^g \times (\nabla \times \mathbf{u}^g) = \frac{1}{2}\nabla(\mathbf{u}^g \cdot \mathbf{u}^g) - (\mathbf{u}^g \cdot \nabla)\mathbf{u}^g \tag{3.5}$$

$$\nabla \times (\mathbf{u} \times \boldsymbol{\omega}) = -(\mathbf{u} \cdot \nabla)\boldsymbol{\omega} + (\boldsymbol{\omega} \cdot \nabla)\mathbf{u} \tag{3.6}$$

The system of equation to be solved reads:

$$\frac{\partial\mathbf{u}^g}{\partial t} + (\mathbf{u}^g \cdot \nabla)\mathbf{u}^g = -\nabla p^g + \nu\Delta\mathbf{u}^g + \mathbf{u}^v \times \boldsymbol{\omega}^g \tag{3.7}$$

$$\frac{d\boldsymbol{\omega}^v}{dt} = (\boldsymbol{\omega}^v \cdot \nabla)(\mathbf{u}^v + \mathbf{u}^g) + \nu\Delta\boldsymbol{\omega}^v \tag{3.8}$$

$$\nabla \cdot (\mathbf{u}^g + \mathbf{u}^v) = 0 \tag{3.9}$$

By using the divergence free vortex element the induced velocity $\mathbf{u}^v$ will automatically fulfills the divergence free constraint. Thus the mass conservation equation only has to be valid for the grid velocities $\mathbf{u}^g$ and Eq. (3.9) is reduced to:

$$\nabla \cdot \mathbf{u}^g = 0 \tag{3.10}$$

Eqs. (3.7) and (3.8) are dynamically coupled. Eq. (3.7) is coupled with the Eq. (3.8) through the additional term $\mathbf{u}^v \times \boldsymbol{\omega}^g$ whereas the coupling of the second equation with the first one is due to the terms $(\mathbf{u}^g \cdot \nabla)\boldsymbol{\omega}^v$ and $(\boldsymbol{\omega}^v \cdot \nabla)\mathbf{u}^g$. Eqs. (3.7) and (3.8) are solved sequentially. Eq. (3.7) is solved using grid-based scheme whereas Eq. (3.8) is treated using the grid free computational vortex method. The sum of these two equations written in the same variables retrieves the original Navier–Stokes equation. The effect of small structures on gird based solution is taken by the term $\mathbf{u}^v \times \boldsymbol{\omega}^g$ into account. The physical meaning of this term can easily be explained when applying the curl operator:

$$\nabla \times (\mathbf{u}^v \times \boldsymbol{\omega}^g) = -(\mathbf{u}^v \cdot \nabla)\boldsymbol{\omega}^g + (\boldsymbol{\omega}^g \cdot \nabla)\mathbf{u}^v \tag{3.11}$$

The first term on the r.h.s. of Eq. (3.11) describes the transport of the grid based vorticity $\boldsymbol{\omega}^g$ by the velocity induced by small vortices $\mathbf{u}^v$, whereas the second term is responsible for the rotation and amplification of the grid based vorticity in field of $\mathbf{u}^v$. Since the vortices are getting small due to stretching of vortex lines and can become invisible on the grid, this term needs a special treatment.

3.2 Correction of governing equations

The term $\mathbf{u}^v \times \boldsymbol{\omega}^g$ in the grid-based equation (3.7) involves spatial and temporal scales which can be much less than the quantities represented on the grid. This can lead to the stiffness of the Eq. (3.7) which is a common problem in the modeling of multiscale physics. A common way to overcome this problem is the averaging of the terms representing fine scales [87]. Generally the term $\mathbf{u}^v \times \boldsymbol{\omega}^g$ can produce scales compared with grid size and beyond. To remedy the stiffness issue the system of Eqs. (3.7) and (3.8) are rewritten in the form:

$$\frac{\partial \mathbf{u}^g}{\partial t} + (\mathbf{u}^g \cdot \nabla)\mathbf{u}^g = -\nabla p^g + \nu \Delta \mathbf{u}^g + \overline{\mathbf{u}^v \times \boldsymbol{\omega}^g} \tag{3.12}$$

$$\frac{d\boldsymbol{\omega}^v}{dt} = (\boldsymbol{\omega}^v \cdot \nabla)(\mathbf{u}^v + \mathbf{u}^g) + \nu \Delta \boldsymbol{\omega}^v + \nabla \times [\mathbf{u}^v \times \boldsymbol{\omega}^g - \overline{\mathbf{u}^v \times \boldsymbol{\omega}^g}] \tag{3.13}$$

where $\overline{\mathbf{u}^v \times \boldsymbol{\omega}^g}$ is spatially filtered vector. Averaged terms are often used in transport equations describing multiscale processes to avoid stiffness. For instance, averaged source term is used in species transport equation in combustion, subgrid stresses in large eddy simulation (LES) equations, Reynolds stresses in RANS equations and etc. They cannot be calculated from transport equations for averaged quantities. They should be modelled and non-universality of these closure models is the biggest weakness of many theories. An important advantage of the current method is that the value of $\overline{\mathbf{u}^v \times \boldsymbol{\omega}^g}$ can be calculated directly since $\mathbf{u}^v$ and $\boldsymbol{\omega}^g$ are both known. Thus the system of Eq. (3.12) and (3.13) is closed and no closure model is necessary. Averaging is necessary to avoid numerical noise caused by irregular distribution of vortex elements inside of cells. This formalism doesn't use commutation of differencing and filtering operators which results in big difficulties in LES formalism.

3.3 Derivation of the equation for kinetic energy of grid-based velocity field

To understand the energy exchange between large scales on the grid and fine scales in Lagrangian framework the transport equation for kinetic energy should be analyzed. By multiplying Eq. (3.12) with u_i^g one obtains the equation of kinetic energy for grid-based velocity field $k^g = \frac{1}{2}u_j^g u_j^g$

$$\frac{\partial k^g}{\partial t} + u_j^g \frac{\partial k^g}{\partial x_j} = \frac{\partial}{\partial x_j}\left(p^g u_j^g + \nu \frac{\partial k^g}{\partial x_j}\right) + \mathbf{u}^g \overline{\mathbf{u}^v \times \boldsymbol{\omega}^g} \tag{3.14}$$

last term in Eq. (3.14) describes the contribution of fine scales to the energy of the grid based motion. It shows that the large scales resolved on the grid exchange energy with fine scale motions resolved with vortex method. The mechanism of energy exchange between scales is evaluated in the real case of three dimensional turbulence simulation in the following chapters (see section (4.4)).

3.4 Scale separation

The large scale flow field represented on the grid is separated from the small scale one to be represented by vortex elements using the filtration procedure taken from Large Eddy Simulation (LES) (see section (2.2.2.1)). First, the original velocity field $\mathbf{u}^g$ is filtered with some filter function:

$$\overline{\mathbf{u}}^g(\mathbf{x}, t) = \int_{-\infty}^{\infty} \mathbf{u}^g(\zeta, t) G(\mathbf{x} - \zeta) ds \tag{3.15}$$

where $G(\mathbf{x} - \zeta)$ is a certain filter function. The small scale velocity field $\mathbf{u}'$ calculated as the difference between the original and filtered fields equation. $\mathbf{u}'$ must be approximated by vortex particles in regions of concentrated vortices. The procedure for detecting concentrated vortices will be discussed in section (3.6) in details.

$$\mathbf{u}'(\mathbf{x}, t) = \mathbf{u}^g(\mathbf{x}, t) - \overline{\mathbf{u}}^g(\mathbf{x}, t) \tag{3.16}$$

3.5 Interaction between different flow scales

Eqs. (3.12) and (3.13) are dynamically coupled, i.e. the large scale motions influence the small scale ones and vice versa. All interaction mechanisms between scales can be mentioned as follow:

- Interaction through generation of small vortices due to evolution of large grid-based vorticity. Due to instability the vorticity represented on the grid tends to creation of concentrated vortex structures. As soon as the size of vortex is getting comparable with the cell size, small vortices are generated from large grid based ones according to the algorithm described in section 3.6.

- Influence of large grid based vortices on small vortices. This influence is taken by terms $(\mathbf{u}^g \cdot \nabla)\boldsymbol{\omega}^v$ and $(\boldsymbol{\omega}^v \cdot \nabla)\mathbf{u}^g$ in Eq. (3.13). The large vortices represented on grid contribute to the vortex convection, rotation and amplification of small vortices.

- Influence of small vortices on large ones by generation of additional small vortices in grid based field. This process is discussed shortly in section (3.1).

- Influence of small vortices on large ones by mapping of small vortices to grid. The mapping is performed in two cases:

    - Diffusion of small vortices according to Eq.(2.86) and mapping them back to the grid if they become large.
    - Fine vortices can create the clusters. For this case a special algorithm should be developed to recognize the clusters, their approximation and mapping them to the grid.

3.6 Approximation of small vortices by vortex elements: Algorithm of vortex cluster identification

Creation of small scale vortices occurs in the large scale flow due to natural instability. As described in [88], the first step of vortex identification is the computation of the pulsation velocity field as the difference between the original and filtered fields at each grid point (equation 3.16). Then the vortex identification criterion λ_{ci} [89] is applied to the pulsation field and generating the field λ_i. The cells at which $\lambda_i > \lambda_{ci,min}$ contain the vortices which in principle can be converted to vortex particles. Such cells are marked as active ones using the $\lambda_{i,active}$ field. $\lambda_{ci,min}$ is a certain small value introduced in order to limit the number of particles.

$$\lambda_{i,active} = \begin{cases} 1, & \text{if } \lambda_{ci} > \lambda_{ci,min} \\ 0, & \text{otherwise} \end{cases} \tag{3.17}$$

To keep the required computational resources on an acceptable level, only small vortices with size proportional to the local cell size Δ are to be converted to single vortex particles. It is supposed that the larger vortices with scales of a few Δ can accurately be represented on the grid. Therefore they should be identified and separated from small scale ones. According to designed algorithm, all neighboring cells of the i_{th} cell are checked for the condition $\lambda_{ci} > \lambda_{ci,min}$. If all neighbors fulfill this condition they are identified as a cell cluster which remains on the grid and all their cells become non-active $\lambda_{i,active} = 0$. Only activated vortices in cells with $\lambda_{i,active} = 1$ must be replaced by vortex particles. At the present stage of our development, the cluster identification

for the unstructured grids implemented in OpenFOAM is performed only for cells with joint faces marked by A in Fig. (3.2). The neighbors marked by B are converted to vortex particles. This means that the number of particles is a little bit larger than it could be. In the future, this shortage can be overcome by enlargement of the neighbor list, which can be pre-processed in OpenFOAM if it will be necessary. Thus, the vortices with scales of less than three cell sizes and some vortices located on clusters borders are converted to particles.

At each cell with $\lambda_{i,active} = 1$ the new vortex particle is introduced at the cell center if the permissible number of vortex particles per cell N_{pt} is not exceeded. Otherwise, the new vortex replaces the cell's weakest one. The number N_{pt} was introduced to keep the total number at a reasonable level. This restriction is conform with the concept that the largest contribution to the subgrid kinetic energy is made by a small fraction of the strongest vortices. The radius of the new vortex is set as $\sigma = \beta Vol_i^{1/3}$, where β is the overlapping ratio which is taken as $\beta = 2$ and Vol_i is the volume of the i-th cell. If the distance from the new particle to one already existing in the cell is smaller than some permissible distance $\alpha\Delta$, $\alpha \ll 1$ they are merged. The vortex particle strength is calculated as:

$$\boldsymbol{\alpha} = Vol_i\boldsymbol{\omega}^v = Vol_i(\nabla \times \mathbf{u}') \tag{3.18}$$

The velocity $\mathbf{u}^v(\mathbf{x}, t)$, induced by the vortex particles, is calculated at grid points $\mathbf{x}$ using the Biot-Savart law (equation (2.73)) and subtracted from the grid velocity $\mathbf{u}^{g,new} = \mathbf{u}^g - \mathbf{u}^v$. Thus, the total velocity at grid points $\mathbf{u}^{g,new} + \mathbf{u}^v = \mathbf{u}^g$ remains constant after the vortex particle generation procedure.
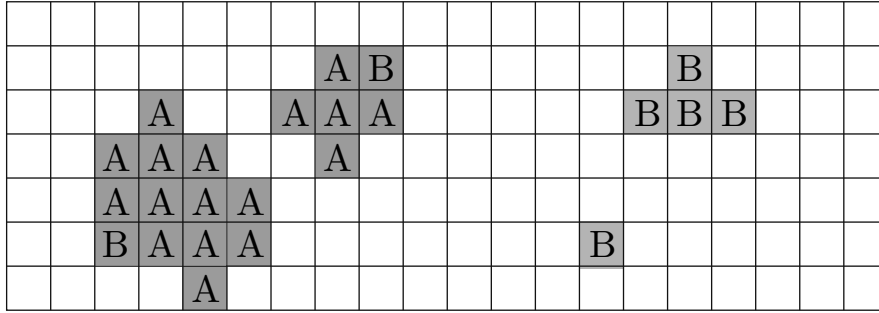
Figure 3.2: Cells with $\lambda_{ci} > 0$ (shadowed), cluster cells (A), cells with fine scale vortices converted to vortex particles (B).

3.7   A-priori test for JBC (Japan Bulk Carrier) benchmark case

Computation of the velocity induced by vortex particles is an acknowledged bottleneck of vortex methods (VM) (see section (2.3.2.5)). The problem can be reduced using either the vortex-in-cell (VIC) approach or the Fast Multipole Method (FMM). VIC has several limitations. First, common VIC application is based on simple Cartesian grids providing a sufficiently acceleration of computations due to employment of the Poisson equation and Fast Fourier Transformation (FFT). The biggest weakness of the Cartesian grids is the inability of an efficient local refinement to handle flows with complex geometries. The use of many overlapping Cartesian grids is, certainly, a not proper way. Extension of the VIC towards arbitrary grids needs development of procedures of vortex redistribution on unstructured grids which is a complicated problem for high order interpolations. Moreover, the resolution of the VIC method is determined by the resolution of the grid used to solve the Poisson equation. In this case the advantages of the vortex methods become questionable. The same limitations can be ascribed to FMM. To choose the optimal algorithm a kind of a-priori analysis has been done for the turbulent field behind the full-bottomed ship JBC (Japan Bulk Carrier) which is a new benchmark test designed by the National Maritime Research Institute in Tokyo to validate CFD in ship hydromechanics. This test case was selected for the analysis since high quality results for the prediction of the turbulent kinetic energy in the stern area of JBC

using grid-based finite volume method and hybrid URANS/LES turbulence model is available [90]. Therefore, it can be assumed that the vortex structures were also predicted with a high accuracy and can be considered for the analysis which was aimed at development of the following algorithms:

- Efficient algorithm to calculate velocities induced by small scale vortices which can be implemented in OpenFOAM library.

- Efficient algorithm to calculate $(\boldsymbol{\omega}^v \cdot \nabla)\mathbf{u}^g$ term in Eq. (3.13).

As described in section (3.4) the large scale flow field resolved on the grid is separated from the small scale one to be represented by vortex elements using the filtration procedure taken from Large Eddy Simulation (LES). First, the original velocity field $\mathbf{u}^g$ is filtered with some filter function. The small scale velocity field calculated as the difference between the original and filtered fields $\mathbf{u}^v(\mathbf{x},t) = \mathbf{u}^g(\mathbf{x},t) - \overline{\mathbf{u}}^g(\mathbf{x},t)$ is approximated by vortex elements. Identification of vortices corresponding to the velocity field $\mathbf{u}^v$ is performed using one of the vortex identification criteria, for instance Q, λ_2 of λ_{ci}. The details of this study can be found in [91]. The main conclusions is listed here:

- The correlation between the small scale vortices is weak.

- The velocity $\mathbf{u}^v$ induced by small scale vortices is much less than $\mathbf{u}^g$. The probability density function of of the ratio $|\mathbf{u}^v|/|\mathbf{u}^g|$ shows that the velocity $\mathbf{u}^v$ is in average less than one percent of $\mathbf{u}^g$. The maximum possible ratio is barely about ten percent.

- The velocity induced by vortices can be calculated accurately with the maximum error of less than five percent from Biot-Savart law taking into account only the induction of neighboring elements from adjacent two cell layers. Very laborious FMM and VIC procedures can be avoided without loss of accuracy. Strong decay of vortex induction is due to a strong decorrelation of fine scale vorticity, i.e. $\frac{\boldsymbol{\omega}(\mathbf{x})_i^v}{|\boldsymbol{\omega}(\mathbf{xx})_i^v|} \frac{\boldsymbol{\omega}(\mathbf{x+r})_i^v}{|\boldsymbol{\omega}(\mathbf{x+r})_i^v|}$, decaying very quickly when $\mathbf{r}$ grows.

- Enhancement of small scale vorticity is mostly due to enhancement $\boldsymbol{\omega}^v((\boldsymbol{\omega}^v \cdot \nabla)\mathbf{u}^g)$ caused by large scale motion whereas the contribution of fine scales $\boldsymbol{\omega}^v((\boldsymbol{\omega}^v \cdot \nabla)\mathbf{u}^v)$ is small.

Based on this analysis a modified algorithm has been proposed for VπLES and discussed in details in [91]. An important advantage of this algorithm is that it is based on the procedures which are already available in Lagrangian particle tracking routines of OpenFOAM.

3.8 Fukuda & Kamemoto algorithm for vortex tube in incompressible flow

Instability of numerical solution of the vorticity transport equation using vortex method (VM) caused by the stretching term $(\boldsymbol{\omega} \cdot \Delta)\mathbf{u}$ is the most important bottleneck of the vortex method along with the computation of the velocity $\mathbf{u^v}$. This problem was also described in section (2.3.3.2.2). In grid-based methods with low and moderate order schemes the action of the stretching is effectively counterbalanced by the numerical viscosity [92] which is very low in Langrangian vortex methods. The instability caused by this term is much stronger than that due to irregular distribution of vortex particles. Theoretically, a stable vortex method solution can be obtained by increase of the accuracy of the stretching and diffusion simulation which can be achieved by high number of vortex particles and high temporal resolution. Both make the method impractical at least for high Reynolds numbers. Another solution is using different algorithms containing inherent stabilization like remeshing (see section (2.3.3.2.1)) which became an inevitable part of the Vortex-Particle Mesh (VPM) method. The remeshing (or regriding) is based on the grid application and posses the effective resolution proportional to the cell size. The advantages of such a method in comparison with a common grid-based methods are questionable and are still being a point of active discussion among vortex method (VM) community. After a wide literature review an algorithm which was originally proposed in [93] was chosen for current research work to remedy the instability originated from $(\boldsymbol{\omega} \cdot \Delta)\mathbf{u}$ term. The proposed method by Fukuda and Kamemoto [93] is based on three conservation laws:
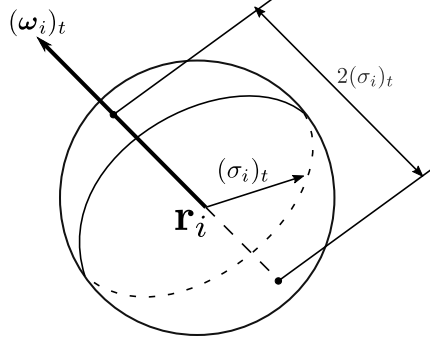
Figure 3.3: A symmetric vortex blob.

- the conservation of the vortex particle volume:

$$\sigma^2 l = const \tag{3.19}$$

where σ and l are the core radius and length of the particle respectively. From Eq. (3.19) it follows

$$\frac{d\sigma}{dt} = -\frac{\sigma}{2l}\frac{dl}{dt} \tag{3.20}$$

- the conservation of the circulation of the vortex tube if the viscosity is neglected

$$\sigma^2 |\boldsymbol{\omega}^v| = const \tag{3.21}$$

From Eq.(3.21) it follows:

$$\frac{d\sigma}{dt} = -\frac{\sigma}{2|\boldsymbol{\omega}^v|}\frac{d|\boldsymbol{\omega}^v|}{dt} \tag{3.22}$$

and

$$|\boldsymbol{\omega}^v(t + \Delta t)| = |\boldsymbol{\omega}^v(t)| \left(\frac{\sigma(t)}{\sigma(t + \Delta t)}\right)^2 \tag{3.23}$$

Multiplying Eq. (3.23) with the volume Vol ascribed to the vortex particle we obtain a simple equation for the magnitude of the vortex particle strength $\boldsymbol{\alpha}$

$$|\boldsymbol{\alpha}(t + \Delta t)| = |\boldsymbol{\alpha}(t)| \left(\frac{\sigma(t)}{\sigma(t + \Delta t)}\right)^2 \frac{Vol(t + \Delta t)}{Vol(t)} \tag{3.24}$$

Since the volume is proportional to σ^3 the last equation can be written in the form

$$|\boldsymbol{\alpha}(t + \Delta t)| = |\boldsymbol{\alpha}(t)| \frac{\sigma(t + \Delta t)}{\sigma(t)} \tag{3.25}$$

Stabilizing property of the scheme becomes obvious [93]. In case of stretching ($\frac{\sigma(t+\Delta t)}{\sigma(t)} < 1$) the strength of the particle decreases $\frac{|\boldsymbol{\alpha}(t+\Delta t)|}{|\boldsymbol{\alpha}(t)|} < 1$. To avoid the loss of the total vorticity the authors of [93] proposed to insert new vortex particles using the redistribution algorithm. This procedure simulates the vortex tube elongation described by the equation derived from Eqs. (3.20) and (3.21):

$$\frac{dl}{dt} = \frac{l}{|\boldsymbol{\omega}^v|}\frac{d|\boldsymbol{\omega}^v|}{dt} \tag{3.26}$$

The algorithm consists of the following substeps:

39

- Calculation of the change of the vorticity strength magnitude:

$$\frac{d|\boldsymbol{\omega}^v|}{dt} = \frac{\boldsymbol{\omega}^v}{|\boldsymbol{\omega}^v|}\frac{d\boldsymbol{\omega}^v}{dt} \tag{3.27}$$

  where $\frac{d\boldsymbol{\omega}^v}{dt}$ is calculated from (3.13) without viscous diffusion term. The term $(\boldsymbol{\omega}^v \cdot \nabla)\mathbf{u}^v$ is calculated taking into account adjacent vortex particles located only within one or two layers of neighboring cells.

- Calculation of the particle length from Eq. (3.26)

- Calculation of the particle core radius. First, the intermediate core radius σ^* is calculated from Eq. (3.22). The viscosity influence is modeled additionally by the core spreading method (CSM) (section 2.3.2.3). Thus, the updated radius is $\sigma(t+\Delta t) = \sigma^* + \sqrt{4\nu\Delta t}$. In contrast to, for instance Particle Strength Exchange (PSE) ([14]), CSM is the most suitable way within the general design of our method. If the vortices size grows due to viscosity and flow stagnation they are mapped back to the grid.

- Calculation of the new particle orientation:

$$\boldsymbol{\omega}^* = \boldsymbol{\omega}^v(t) + \frac{d\boldsymbol{\omega}^v}{dt}\Delta t \tag{3.28}$$

- Calculation of the particle strength magnitude from Eq. (3.25).

- Calculation of the new strength vector:

$$\boldsymbol{\alpha}(t+\Delta t) = |\boldsymbol{\alpha}(t+\Delta t)|\frac{\boldsymbol{\omega}^*}{|\boldsymbol{\omega}^*|} \tag{3.29}$$

- Redistribution.

  The method was successfully tested in [93] for the inclined collision of two vortex rings which is a popular test case in vortex method. A disadvantage of this model is an avalanche-like increase of the vortex particles number due to the redistribution when the stretching occurs. The growth of vortex particles number should be counterbalanced by a special elimination procedure of [93] based on a knowledge of a threshold for the dissipation rate which is difficult to set in a general flow case. To develop a robust algorithm, to obtain a stable solution and to keep the particle number in a reasonable range the redistribution procedure in the current research work has been avoided. Thus, the finest vortices are removed. This reduces the range of scales that must be resolved in a numerical calculation. Such a reduction, as pointed by [68], is a major goal of every turbulence model and is an immanent part of every turbulence model.

The particle displacement is calculated from the trajectory equation:

$$\frac{d\mathbf{r}_i}{dt} = \mathbf{u}_i^g + \mathbf{u}_i^v \tag{3.30}$$

The velocity $\mathbf{u}_i^v$ is calculated from the Biot-Savart law taking into account adjacent vortex particles located only within one or two layers ($L = 2$) of neighboring cells. The simple Euler method is used for the integration of differential equations.

3.9 Choice of vortex elements

The choice of vortex elements is dictated by requirements of simplicity of calculation of induced velocities and operators of convection and diffusion. The most comprehensive analysis of different vortex elements is given by [94]. The results presented in this thesis is based on the vortex particles (vortex blob) with mollified vorticity of:

$$\boldsymbol{\omega} = 3/(4\pi\sigma^3)\boldsymbol{\alpha}e^{-\xi^3/\sigma^3} \tag{3.31}$$

This smoothing function was proposed first by [95]. The velocity induced by this vortex particle (or vortex blob) and the strain rate tensor are given by:

$$\mathbf{u}_p^v = \frac{1}{4\pi}\frac{\boldsymbol{\alpha}\times\boldsymbol{\xi}}{\xi^3}(1 - e^{-\xi^3/\sigma^3}) \tag{3.32}$$

$$\frac{\partial u_i^v}{\partial x_j} = \frac{3}{4\pi\sigma^3}\frac{\xi_j(\boldsymbol{\alpha}\times\boldsymbol{\xi})}{\xi^5}(\xi^3 e^{-\xi^3/\sigma^3} + \sigma^3(e^{-\xi^3/\sigma^3} - 1)) - \frac{1}{4\pi}\varepsilon_{ijk}\alpha_k\frac{1 - e^{-\xi^3/\sigma^3}}{\xi^3} \tag{3.33}$$

where $\zeta = |\mathbf{x} - \mathbf{x}_p|$.

3.10 Rescaling

The computations shows that the velocity $\mathbf{u}^v$ calculated using Biot-Savart law and the strength γ is much less than target value of $\mathbf{u}'$. The reason is not only because a part of vortex particles belonging to clusters were eliminated in VπLES algorithm but also if vortex particles would be generated at each cell the velocity calculated from the Bio-Savart formula $\mathbf{u}^v$ differs from the expected $\mathbf{u}'$. The reason is that the identity:

$$\mathbf{u}^v(\mathbf{x}_j, \boldsymbol{\alpha}) = \frac{1}{4\pi}\nabla\times\sum_{i=1}^{M}\frac{(\nabla\times\mathbf{u}'(\mathbf{x}_i))Vol_i}{|\mathbf{x}_i - \mathbf{x}_j|} = \frac{1}{4\pi}\nabla\times\sum_{i=1}^{M}\frac{\boldsymbol{\alpha}_i}{|\mathbf{x}_i - \mathbf{x}_j|} \equiv \mathbf{u}'(\mathbf{x}_j) \tag{3.34}$$

is satisfied in computations only in the limit $M \to \infty$. This means there must be many vortex particles within each cell which remarkably increase the computational costs. To avoid this and to get a proper level of $\mathbf{u}^v$, it is suggested to recalculate the strengths using the rescaling procedure:

$$\boldsymbol{\alpha}_i^{rescaled} = \frac{|\nabla\times\mathbf{u}'(\mathbf{x}_i))|}{|\nabla\times\mathbf{u}^v(\mathbf{x}_i, \boldsymbol{\alpha})|}\boldsymbol{\alpha}_i \tag{3.35}$$

3.10.1 Description of one step of VπLES algorithm in explicit coupling

Implementation of the method into OpenFOAM was sufficiently simplified by the availability of many libraries developed in OpenFOAM for Lagrangian particle class. The class of *solidParticle* was used for representing vortex particles (vortex blobs). The routines for the interpolation of $\mathbf{u}^g$, $\partial u_i^g/\partial x_j$ and $\boldsymbol{\omega}^g = \nabla \times \mathbf{u}^g$ from grid points to particles, particle tracking, filtering procedure to calculate $\overline{\mathbf{u}^v \times \boldsymbol{\omega}^g}$ and the list of neighbors are available in OpenFOAM and effectively used to develop a fast working code. The flowchart of the whole algorithm is presented in Fig. (3.4), (3.5) and (3.6). Vortex particles identification procedure, computation of the source term $\overline{\mathbf{u}^v \times \boldsymbol{\omega}^g}$ and an OpenFOAM class for solving vortex transport equation (Eq.3.13) in Lagrangian fashion has been developed in this research. The term $\overline{\mathbf{u}^v \times \boldsymbol{\omega}^g}$ in (3.12) is treated in an explicit way. In the present version of VπLES library most of routines were parallalized excepting computation of $\mathbf{u}^v$ and $\partial u_i^v/\partial x_j$ both at particle centers and grid points which need to be parallelized in the future.

1. Calculation of velocities $\mathbf{u}^g$ and pressure p^g using Open-FOAM. $\overline{\mathbf{u}^v \times \boldsymbol{\omega}^g}$ is taken from the previous time step

2. Vortex particles identification (see Fig. 3.5)

3. Updating particle positions and strengths (see Fig. 3.6)

4. Computation of the term $\overline{\mathbf{u}^v \times \boldsymbol{\omega}^g}$ for each cell. $\boldsymbol{\omega}^g$ is from OF.

5. Mapping vortex particles onto grid if their size $> \gamma\Delta$
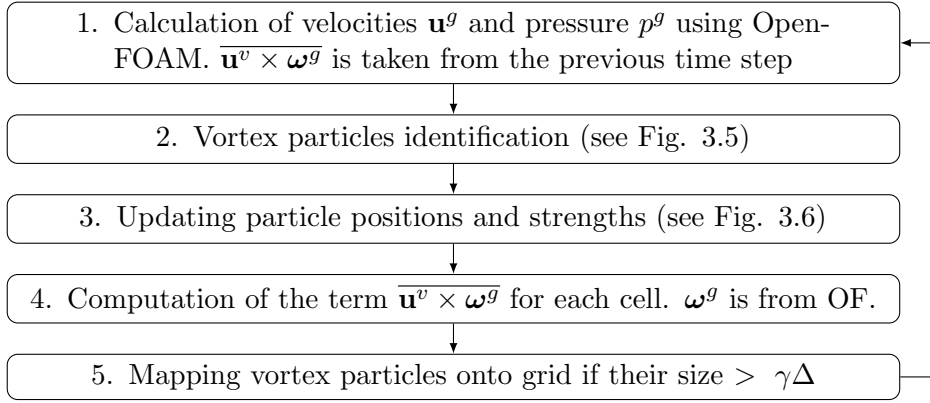
Figure 3.4: Outline of each time step of VπLES method. Steps 2-5 are newly developed routines implemented into OpenFOAM.

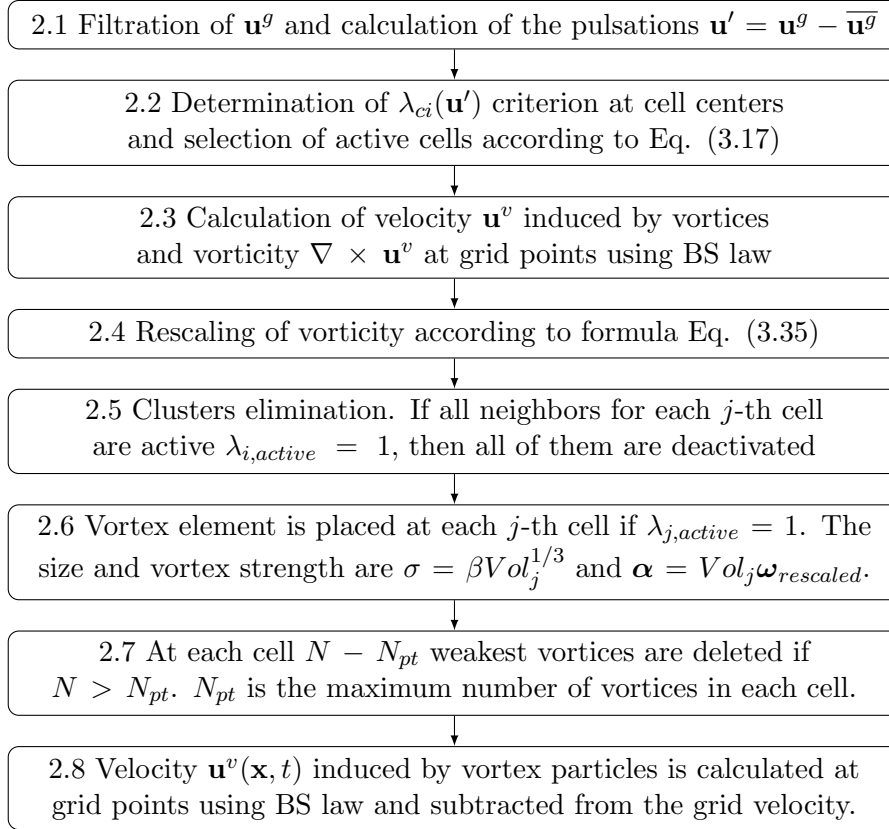2.1 Filtration of $\mathbf{u}^g$ and calculation of the pulsations $\mathbf{u}' = \mathbf{u}^g - \overline{\mathbf{u}^g}$

2.2 Determination of $\lambda_{ci}(\mathbf{u}')$ criterion at cell centers
and selection of active cells according to Eq. (3.17)

2.3 Calculation of velocity $\mathbf{u}^v$ induced by vortices
and vorticity $\nabla \times \mathbf{u}^v$ at grid points using BS law

2.4 Rescaling of vorticity according to formula Eq. (3.35)

2.5 Clusters elimination. If all neighbors for each j-th cell
are active $\lambda_{i,active} = 1$, then all of them are deactivated

2.6 Vortex element is placed at each j-th cell if $\lambda_{j,active} = 1$. The
size and vortex strength are $\sigma = \beta Vol_j^{1/3}$ and $\boldsymbol{\alpha} = Vol_j \boldsymbol{\omega}_{rescaled}$.

2.7 At each cell $N - N_{pt}$ weakest vortices are deleted if
$N > N_{pt}$. N_{pt} is the maximum number of vortices in each cell.

2.8 Velocity $\mathbf{u}^v(\mathbf{x}, t)$ induced by vortex particles is calculated at
grid points using BS law and subtracted from the grid velocity.

Figure 3.5: Flowchart of the vortex particle identification procedure. BS stands for Bio-Savart.

Algorithm for active vortices

Algorithm for passive vortices when
the inner interaction between vortices
is neglected

3.1 Velocities $\mathbf{u}^v$ and
tensor $\partial u_i^v / \partial x_j$ at vor-
tex centers from BS law

3.2 Velocities $\mathbf{u}^g$ and
tensor $\partial u_i^g / \partial x_j$ at vor-
tex centers from OF

3.3 Vortex displacement from
equation $d\mathbf{r}/dt = \mathbf{u}^v + \mathbf{u}^g$ (OF)

3.1 Velocities $\mathbf{u}^g$ and
tensor $\partial u_i^g / \partial x_j$ at vor-
tex centers from OF

3.4 Change of the vortic-
ity strength magnitude at
vortex centers from (3.27)

3.2 Vortex displacement from
equation $d\mathbf{r}/dt = \mathbf{u}^g$ (OF)

3.5 Particle length from (3.26)

3.6 Particle core ra-
dius from (3.20)

3.7 Calculation of the par-
ticle core spreading using
Core Spreading Method

3.8 New particle ori-
entation from (3.28)

3.9 Particle strength
magnitude from (3.25)

3.10 New strength
vector from (3.29)

3.11 At each cell $N - N_{pt}$ weakest
vortices are deleted if $N > N_{pt}$.

Figure 3.6: Flowchart of the updating procedure for the particle positions and strengths. OF stands for OpenFoam.

3.10.2 Free parameters of the method

VπLES method consists of a few free parameters which are:

- $\lambda_{ci,min}$ is a threshold to sort out weak fine scale vortices (see definition (3.17)).

- β is the overlapping ratio of vortex particles.

- γ is the parameter to map the large particles back to the grid. If a size of a vortex exceeds $\gamma\Delta$ it is mapped onto grid.

- N_{pt} is the permitted number of particles in cell.

Experience in practical applications shows that λ_{ci} is high at the vortex and then abruptly decays. That is why the results are relatively insensitive to the choice of $\lambda_{ci,min}$ if this parameter is smaller than, say, ten percent of the maximum λ_{ci} determined in the whole flow. The overlapping parameter β is a typical parameter widely used in vortex particle methods to attain a proper accuracy and stability of computations. Unfortunately, it is difficult to find any unambiguous recommendation for its choice. In this work $\beta = 2$ relying on the positive experience of [96] and [97] was chosen. Parameter γ is taken as four since all vortices with sizes larger than three cell sizes are not converted to the particles according to the algorithm described in section (3.10.1). N_{pt} is the most critical free parameter which influence is proven in section (4.10).

3.11 Treatment of no-slip boundary condition in VπLES for wall-bounded flow

The boundary conditions (BC) are explicitly formulated only for the grid solution. There are no boundary conditions for the vortex method. For instance, the no slip BC for the velocity can be written in the form:

$$\mathbf{u}^g + \mathbf{u}^v = 0 \leftarrow \mathbf{u}^g = -\mathbf{u}^v \tag{3.36}$$

The necessary and sufficient boundary condition for the pressure in incompressible case, which is used in the Poisson equation within pressure correction approaches, is the Neumann BC obtained by the projection of the Eq. (3.12) onto the normal direction $\mathbf{n}$ [88]:

$$\frac{\partial p^g}{\partial n} = -(\frac{\partial \mathbf{u}^g}{\partial t} + (\mathbf{u}^g \cdot \nabla)\mathbf{u}^g) + \overline{\mathbf{u}^v \times \boldsymbol{\omega}^g}\mathbf{n} \tag{3.37}$$

where the term proportional to the kinematic viscosity was traditionally neglected. Similar boundary condition can be derived for the scalar field and for flows with variable transport properties. In this thesis this boundary condition was not applied and the traditional ones for the grid-based solution was utilized based on the following considerations:

- Close to the wall the flow is rather smooth and the creation of energetically important concentrated fine structures is unlikely.

- Representation of the continuously spatially distributed structures by discrete particles with a primitive spatial spherical distribution of vorticity $\boldsymbol{\omega} = 3/(4\pi\sigma^3)\boldsymbol{\alpha}e^{(-r^3/\sigma^3)}$ results in a serious approximation error and cause numerical instability.

- This approximation can be not physical if the vorticity induced by a particle is not zero beneath the wall $\boldsymbol{\omega}(y < 0) \neq 0$, where y is the distance from the wall (see Fig. 3.7). This case takes place when the elongated cells with $\Delta x \gg \Delta y$, where x is the coordinate along the wall, are usually used. In this case the vortex radius $\sigma \approx \beta\Delta x = 2\Delta x \gg \Delta y$. If the vortex is located to the wall closer than $2\Delta x$ the particle approximation of vorticity is fully wrong.

To avoid these difficulties and taking into account the fact, that the influence radius of the vortex particle (area of a sufficient induced velocity) is approximately 2σ we don't allow the particle generation at the distances $y \leq 4\sigma$ introducing the security zone schematically shown in Fig. (3.8). The width of the zone depends on the grid and covers a few grid wall layers in vertical direction. Since the influence of particles at the boundary in such a way is avoided, we use traditional boundary condition for the grid part of the solution.
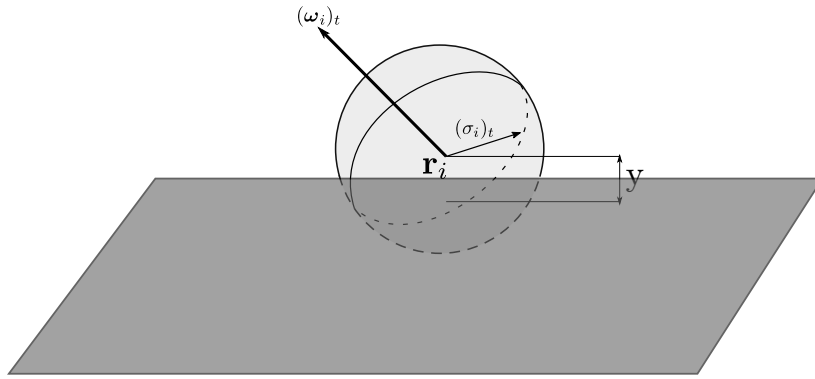
Figure 3.7: Wrong approximation of the vorticity by a vortex particle when the distance from the wall y is less than the vortex particle radius σ.
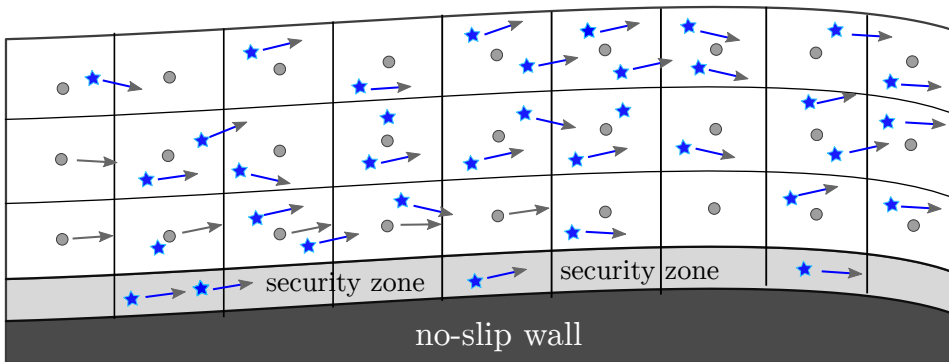

Figure 3.8: Vortex particles utilized in VπLES method. Filled circles are the vortices newly generated at a time instant at cell centers, filled star are the fine old vortices generated at previous time steps, the arrows show the velocities of vortices. In the security zone the generation of new particles is not allowed.

4 Decaying of homogeneous isotropic turbulence

Decaying of homogeneous isotropic turbulence has been a popular test case in the evaluation of SGS models. As a classical turbulence test case the decay of turbulence in a cubical box is investigated in this chapter using VπLES approach and compared with experimental data of Comte-Bellot & Corrsin [98]. Although the experiment of Comte-Bellot & Corrsin was performed in a wind tunnel flow, the result can be extended to the case of decaying homogeneous isotropic turbulence in a box [99]. This simple flow configuration is used to evaluate VπLES method through investigating the turbulent quantities.

In order to initialize turbulent structures, the energy spectrum in wavenumber space at the first location in Comte-Bellot & Corrsin experiment was generated artificially using spacial inverse Fourier transformation. According to [100] Inverse Fourier (IF) approach shows better agreement with experiment compared to Filtered noise and Diffused noise methods. In the context of this work a fully integrated tool in OpenFOAM was developed to construct a turbulent velocity field using random Fourier modes. This utility is based on the very popular method which was proposed by Kraichnan [101]. In this work further development by [102] and [103] and in particular [104] were considered for implementation in OpenFOAM. The measured energy spectrum was modeled by von Karman-Pao spectrum.

4.1 Numerical Setup

The numerical cubical domain have edge lengths of $L = 0.508m$. Grid resolution of 32^3, 64^3, 128^3 and 256^3 cells which consist of hexahedral elements with an equidistant grid spacing were generated using blockMesh utility of OpenFOAM. Periodic boundary condition was applied on each faces of cubical box to be isolated from near wall effect. In order to be consistent with experiment of Comte-Bellot & Corrsin [98] Taylor Reynolds number is chosen as $Re_\lambda = \frac{u_{rms}\lambda}{\nu} = 71.6$ with air kinematic viscosity of $1.5e - 5\frac{m^2}{s}$. Comte-Bellot & Corrsin measured turbulence properties at three different locations downstream of the grid at $\frac{tU_0}{M} = 42, 98$ and 171. These three locations can be transferred to three dimensionless times of $t = 0$, $t = 56$ and $t = 129$ by means of Taylor hypothesis [100]. Temporal evaluation of turbulence and passive scalar mixing properties at these dimensionless times were investigated in the current work using VπLES approach.

For time discretization a second order Cranck-Nickolson scheme was used. The spacial discretization of convective term is performed using several first and second order schemes to show the influence of discretization scheme on the decay of turbulent kinetic energy, auto-correlation function and scalar dissipation rate. CFL criterion is kept less than 0.1 and the time steps is calculated based on that. To initialize turbulent fluctuation at $t = 0$, IF-method is applied to generate a Fourier series of N modes at the arbitrary point x in space. According to [104] a total number of N=5000 modes is a value with minimum error in this case. The velocity field and spectra of generated synthetic turbulence is presented in Figure 4.2 and 4.3 for all mesh resolutions. The maximum resolved wavenumber is determined based on the grid spacing through $k_{max} = \frac{2\pi}{\Delta x}$. In order to have exactly the same root-mean-square velocity (u_{rms}) as in experiment, there is a scaling process which correct the prescribed u_{rms} with respect to desired one. Therefor for all grid resolution the initial u_{rms} is constant and equals $0.222m/s$. In order to be consistent with the experiment the integral length scale is set to 0.024m. A more comprehensive discussion about the synthesized turbulence generator used in this thesis is presented in section 4.2.

Figs. (4.2) and (4.3) show the x-components of generated turbulent velocity fields and the corresponding power spectra respectively. In Fig. (4.2) coherent structures can be distinguished as uniformly colored regions. Increasing the maximum resolved wave number through grid refinement is visible in Fig. (4.3). Fig. (4.4) shows the initialized longitudinal velocity correlations with respect to the grid resolution. In a very coarse grid (32^3) the autocorrelation function is over-

predicated whereas it matches well with experiment in case of fine mesh. In Fig. (4.2.a) colored large scale structures are visible in the case of 32^3 mesh cells. In this under-resolved grid there are not significant small scale structures compare to fine gird. Hence in coarse grid the correlation is stronger. By increasing the grid resolution small scale structures appear in the flow field and the homogeneous isotropic turbulence is being achieved. In this case the correlation of neighboring structures are weaker and match well with experiment.

4.2 Inverse Fourier (IF) approach for generating synthesized turbulent fluctuations

A fully integrated tool in OpenFOAM was developed to construct a turbulent velocity field using random Fourier mode. This utility is based on the very popular method which was proposed first by Kraichnan [101]. According to the theory an arbitrary spatially varying velocity field is given by N random Fourier modes as:

$$\mathbf{u}'_i(x_j) = 2 \sum_{n=1}^{N} \hat{u}^n cos(\mathbf{k}_j^n \mathbf{x}_j + \psi^n) \hat{\boldsymbol{\sigma}}_i^n \tag{4.1}$$

where N is the number of random Fourier modes, $\hat{u}^n$ is the amplitude, ψ^n and $\hat{\sigma}$ are phase angle and direction of the n_{th} mode associated with the n_{th} wave vector k^n . Equation (4.1) generates a Fourier series of N modes at the arbitrary point x in space. The notation used here follows that in [103]. For computing a synthesized turbulent velocity field using equation (4.1) the following steps are necessary [103], [104]:

(a) Random direction of a wave number vector k_i^n. The wave vector is characterized by its spherical coordinates (k_n, ϕ_n, θ_n)

(b) The unit vector σ_n is located in the (ζ_1^n, ζ_1^n) plane and is perpendicular to k_i^n. Its polar angle α_n has an arbitrary random orientation.
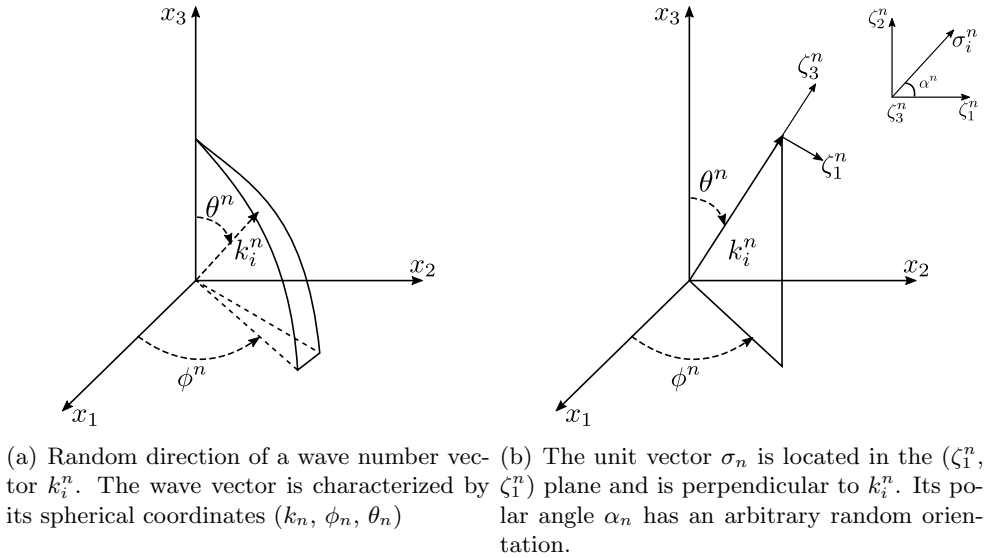
Figure 4.1: Wave vector geometry for the n_{th} Fourier velocity mode (adopted from [6]).

- For each Fourier mode n, compute the random angles ϕ^n, α^n and θ^n (see Fig. (4.1)) and random phase ψ^n.

- Compute the maximum wave number according to the mesh resolution $k_{max} = \frac{\pi}{\Delta x}$.

- Define the minimum wave number as $k_{min} = \frac{2\pi}{L}$, where L is the edge length of the cubical domain.

- Divide the wavenumber space (k_{max}-k_{min}) into N equidistant modes:

$$k_j^n = k_{min} + \frac{k_{max} - k_{min}}{N}(n-1) \tag{4.2}$$

- Compute the randomized wave number unit vector at random point on a unit sphere:

$$k_x^n = sin(\theta^n)cos(\psi^n)$$
$$k_y^n = sin(\theta^n)sin(\psi^n)$$
$$k_z^n = cos(\theta^n) \tag{4.3}$$

- In order to satisfy continuity the unit vector, $\boldsymbol{\sigma}_i$ has to be orthogonal to wave number vector $\mathbf{k}_j$.

- Compute the amplitude $\hat{u}^n$ of each mode from modified von Karman-Pao spectrum using:

$$\hat{u}^n = \sqrt{E(|k_j|)} \tag{4.4}$$

$$E(k) = \alpha \frac{u_{rms}^2}{k_e} \frac{(k/k_e)^4}{[1 + (k/k_e)]^{17/6}} e^{[-2(k/k_\eta)^2]} \tag{4.5}$$

where $\alpha \approx 1.453$ is a dimensionless constant, u_{rms} is the root-mean-square of the velocity fluctuation, k_e is the wave number where the spectrum reaches its maximum (most energetic eddies), k_η is Kolmogorov wave number (smallest turbulent structure). The algorithm implemented in OpenFOAM is closely similar to the work of [104]. The initialized velocity field and power spectra are presented in Figs. (4.2) and (4.3).

(a) grid resolution 32^3 (b) grid resolution 256^3
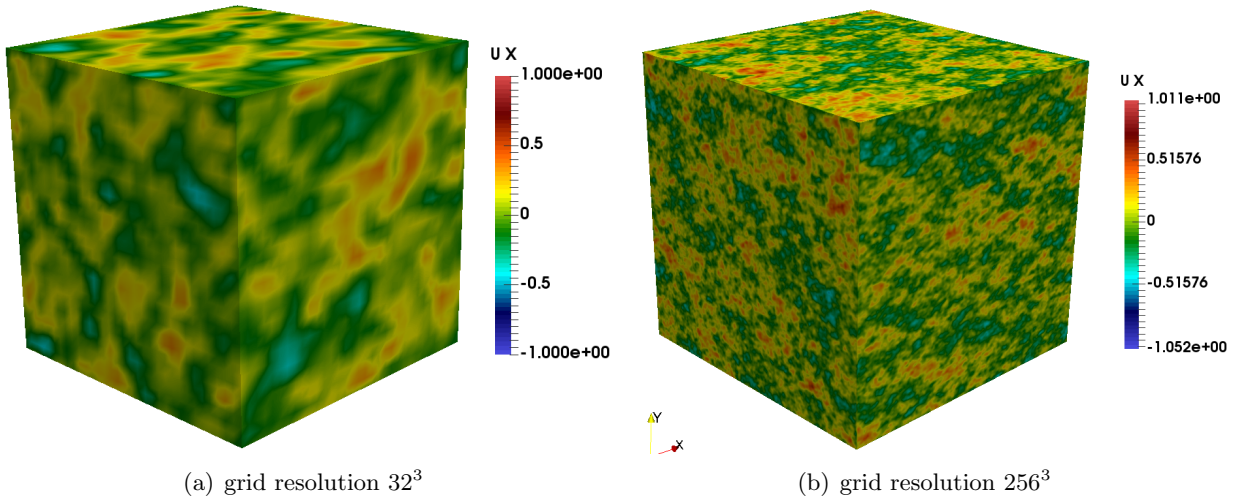
Figure 4.2: x-component of initialized velocity field using inverse-Fourier approach
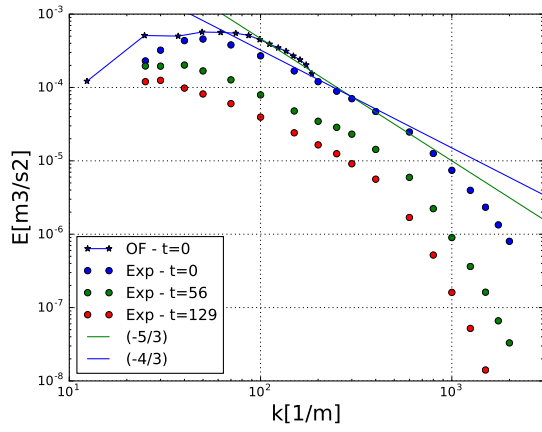
(a) grid resolution 32^3
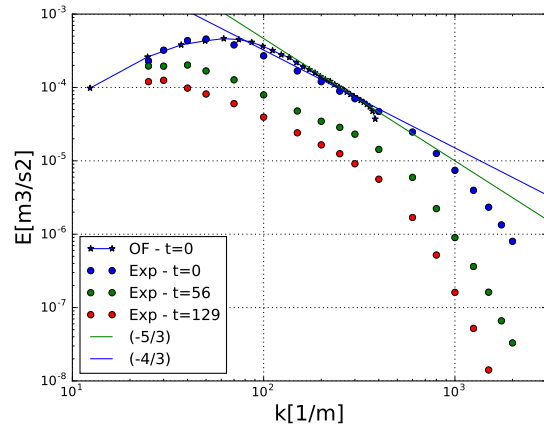
(b) grid resolution 64^3
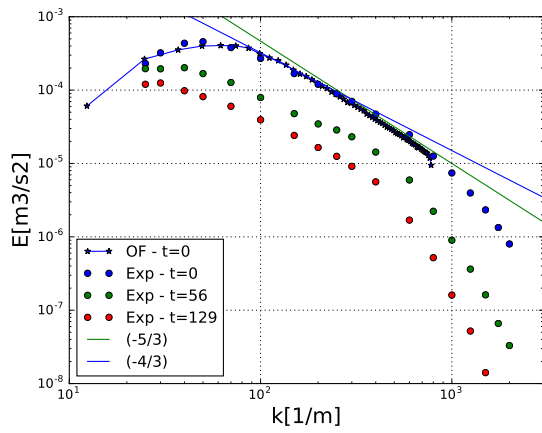
(c) grid resolution 128^3
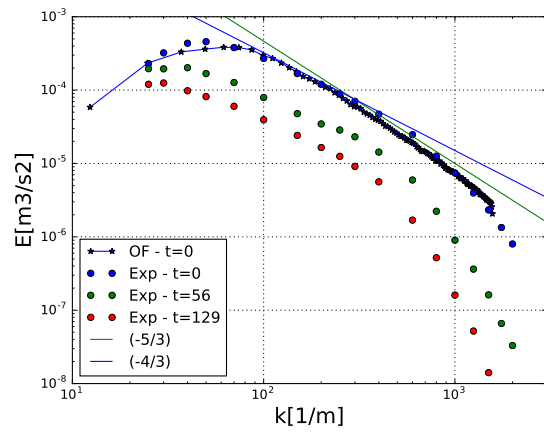
(d) grid resolution 256^3

Figure 4.3: Energy spectra of initialized velocity field by inverse Fourier method
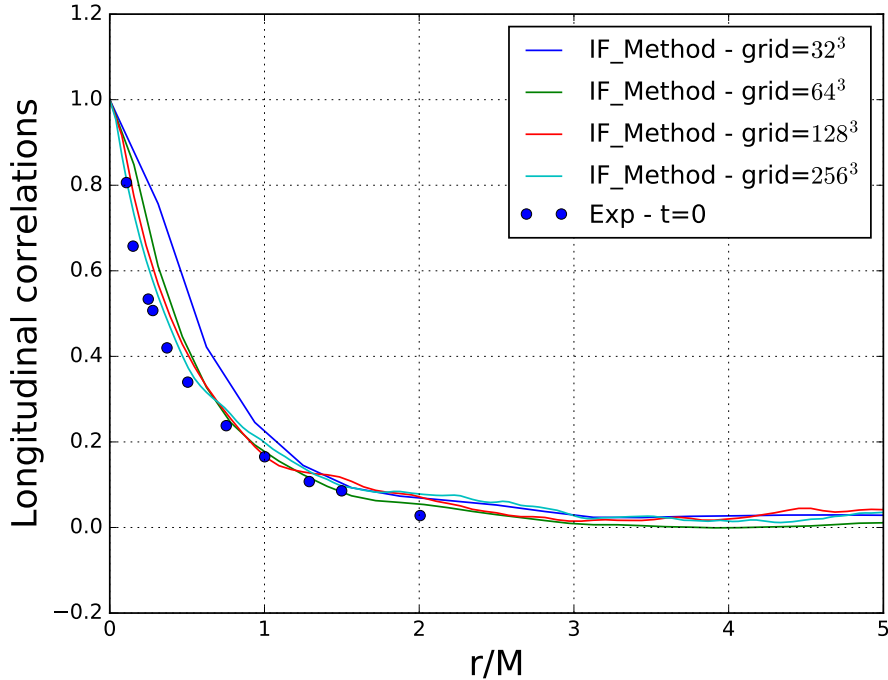
Figure 4.4: Autocorrelation function of initialized velocity field with respect to the grid resolution

4.3 Decay of Turbulent kinetic energy

Since in the case of homogeneous isotropic turbulence in cubical box there is no production of energy, the turbulent kinetic energy decays monotonically in time. This test case does not contain a global shear, strain rotation or near wall effects, therefore it is a proper test case to validate the performance of VπLES in prediction of energy cascading from large scale motion to small scales. Consequently it also shows the proper implementation of balancing between the stretching and diffusion model in the proposed SGS model (VπLES method).

Fig. (4.6) shows the decay of spatially averaged turbulent kinetic energy in a coarse mesh (32^3). The spacial discretization of convective term is performed using linear (central difference) scheme. In the case of coarse grid (32^3 and 64^3) without using any turbulence model, there is a strong over-prediction of turbulent kinetic energy at each time instance. It shows that the grid is too coarse to predict the energy cascading properly without any turbulence model. Since small scale are not resolved here, the dissipation of energy can not be reached with the physical decay. This over prediction issue can also be observed in Fig. (4.9) of the power spectra when less diffusive scheme such as linear scheme was applied for the discretization of convective term. Repeating similar simulation with two different SGS models one with Smagorinsky and one with resolving SGS term with vortex method (VπLES) shows that VπLES is in a pretty good agreement with experiment.

Two different constant C_s in Smagorinsky model were used in order to adjust to the decay properly. As it is observed $C_s = 0.2$ slightly increases the dissipation of kinetic energy k and follow well the decay of turbulence. This effect is similar to increasing the number of particles in VπLES simulation. In both cases of VπLES method and Smagorinsky model there is a clear discrepancy in the first time step. This deviation shows the insufficient amount of subgrid scale energy in VπLES and Smagorinsky at the beginning. Dietzel et al. [100] reports the same discrepancy in first time step.

51

4.4 Contribution of the term $\overline{\mathbf{u}^v \times \boldsymbol{\omega}^g}$ to the energy budget

In section (3.3) a transport equation for kinetic energy of grid-based velocity has been derived. In Fig. (4.7) the term $\mathbf{u}^g \, \overline{\mathbf{u}^v \times \boldsymbol{\omega}^g}$ from Eq. (3.14) is plotted to understand the energy exchange between large and fine scale motions. Fig. (4.7) shows a very important fact that the term $\overline{\mathbf{u}^v \times \boldsymbol{\omega}^g}$ behaves as an energy drain transferring the energy of the grid-based motion into fine scale energy. In the other words, it acts as a diffusive Large Eddy Simulation subgrid model. This is true only in the averaged sense because in contrast to pure diffusive models like the Smagorinsky one, the present term allows the energy back scattering, i.e. flux of the energy from fine scales to the large ones. Indeed, as mentioned above, this term reproduces amplification of the grid-based vorticity in field of $\mathbf{u}^v$ and can lead to a local increase of the kinetic energy. This is illustrated in Fig. (4.5). Fig. (4.7) shows that the energy drain gets larger when the number of particle per cell N_{pt} (see Section (4.10) for more detailes about free parameter N_{pt}) increases. This is a quite logic result, because the energy of fine scale motion grows when N_{pt} increases. The flux of energy, discussed above, is only a part of the total flux. Another part, which is definitely negative, is due to conversion of grid-based vorticity into vortex elements.
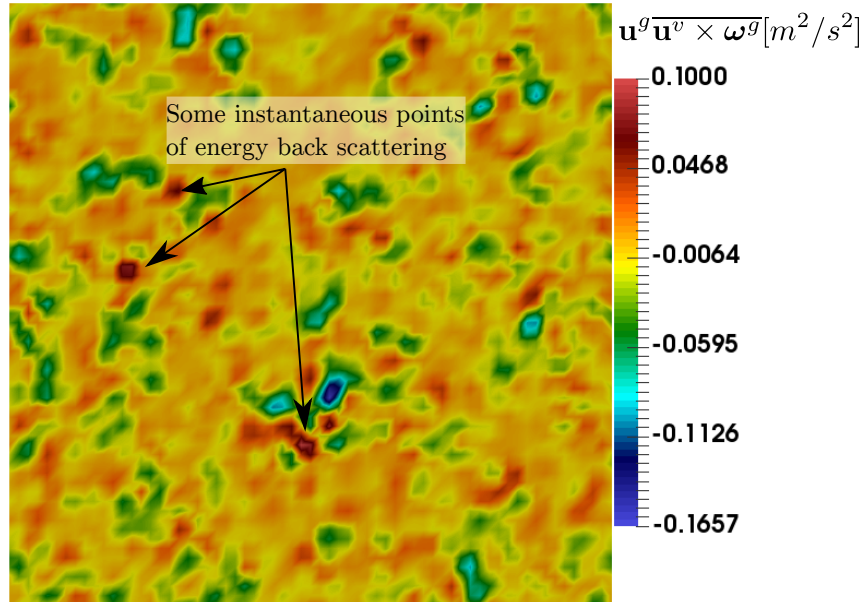
Figure 4.5: Instantaneous distribution of the energy production term $\mathbf{u}^g \, \overline{\mathbf{u}^v \times \boldsymbol{\omega}^g}$ in the middle plane of the computational box at $\tau = 56$. Positive values correspond to the energy increase, grid resolution 64^3.

4.5 LES like behavior and consistency of the model

As mentioned in section (4.4) the coupling term has the same property as the LES subgrid stress with respect to the energy budget. Fig. (4.8) is an additional confirmation of this property. For coarse resolution with 32^3 cells, the kinetic energy $k = \frac{1}{2}(\mathbf{u}_i^g + \mathbf{u}_i^v)(\mathbf{u}_i^g + \mathbf{u}_i^v)$ averaged on the box decays like in LES simulations performed with a simple Smagorinsky model with $C_s = const.$ and with the same resolution as VπLES . The pure grid simulations performed with OpenFOAM without any turbulence model indicate a delayed underestimated energy decay (red line). The lower picture illustrates a remarkable fact. When the resolution grows, the effect of the term $\overline{\mathbf{u}^v \times \boldsymbol{\omega}^g}$ reduces and VπLES method converges to the purely grid simulation (compare results for 32^3 and 128^3 cells grids). In the other words, the VπLES method is consistent and converges to the Direct Numerical Simulation (DNS) when the resolution increases. In all simulations there is a clear drop of the kinetic energy at the first time step reported also by [100]. When the resolution grows the drop slightly decreases but not sufficiently. The literature review shows that this is an artefact

which is specific for the method of artificial generation of initial turbulence used in this paper.
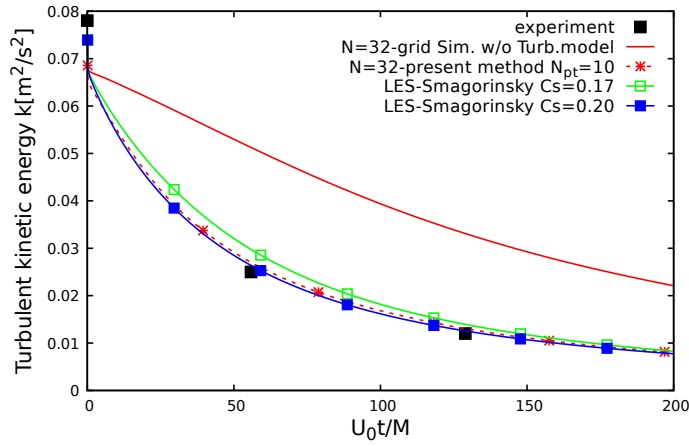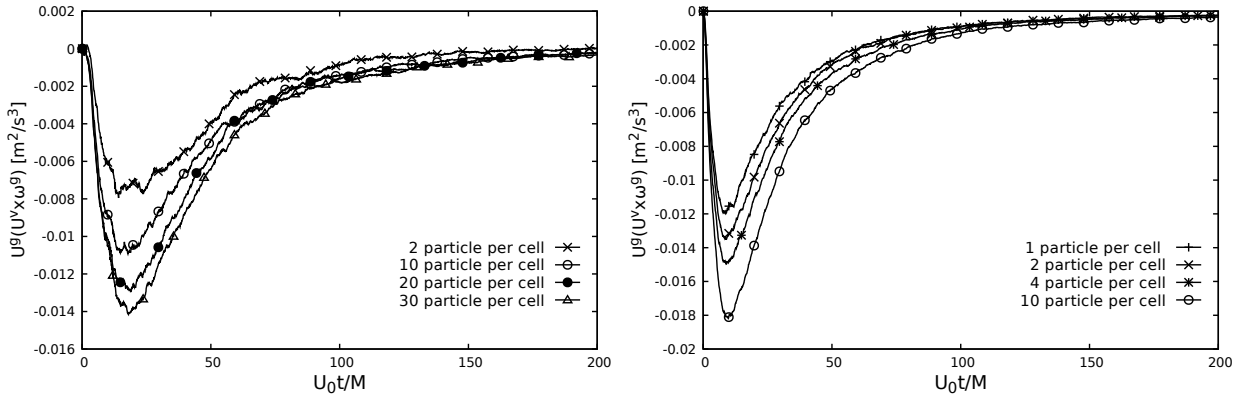

Figure 4.6: Decay of turbulent kinetic energy with and without SGS model - grid resolution 32^3.

(a) Energy drain from large structure in grid solution 32^3 cells

(b) Energy drain from large structure in grid solution 64^3 cells

Figure 4.7: Spatially averaged energy contribution of the term $\overline{\mathbf{u}^v \times \boldsymbol{\omega}^g}$.
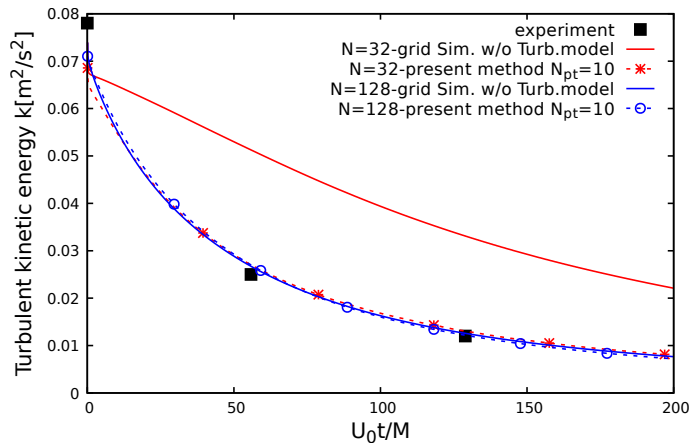

Figure 4.8: Consistency of VπLES to DNS with respect to grid resolution

4.6 Spectrum evolution

Fig. (4.9) shows the evolution of power spectra and growing velocity correlation at different dimensionless times for grid 32^3 without using any turbulence model (i.e. under-resolved DNS). The caption "pure grid simulation" means cases without using any turbulence model. Three different numerical schemes were applied for discretization of convection term in Eq. (2.2). It is observed that in the case of using linear scheme (CDS) with 2nd order of accuracy the energy at high wave numbers is over predicted. Since small scales are not resolved here and also there is no turbulence model to model the subgrid scales, the dissipation of energy can not be reached and kinetic energy will accumulate. In contrast to linear scheme a more diffusive scheme such as upwind or linearUpwind prevents the over-prediction at the middle scales but drastically damps the energy at small scales (Figs. (4.9.c) and (4.9.e)).

As already discussed the longitudinal velocity correlation of the initialized synthetic turbulence is not in good agreement with experiment for grid 32^3. Figs. (4.9.d) and (4.9.f) show cases in which more diffusive discretization schemes has been used. In these cases temporal evaluation of velocity correlation follows the experiment but the prescribed integral length scale is over predicted. The case with linear scheme does not predict the same tendency as in experiment and the growing of integral length scale is not physical (Fig. (4.9.b)).

Fig. (4.10) shows the influence of using SGS model on the temporal evolution of energy spectra in grid 32^3. The Smagorinsky model with a model constant of $C_s = 0.17$ and VπLES method with direct resolution of subgrid motion using vortex method are compared in Fig. (4.10). In both cases the evolution of energy spectra follow the experiment. In case of VπLES method there is no large over-prediction in middle scales and also energy at small scales are preserved. Fig. (4.11) shows the influence of number of particles per cell N_{pt} on the prediction of power spectra at each dimensionless time instance. Increasing number of allowed particles per cell N_{pt} from 2 to 10 leads to more accurate prediction of energy content at small scales. In fact it increases the resolution of VπLES model to predict small scale motions and consequently more physical diffusion rate. Increasing N_{pt} from 10 to 20 doesn't show remarkable changes in the result. This means new vortices which are allowed to add beyond 10 particles per cell in the numerical domain are very weak and do not have influence on the grid solution. It confirms the convergency of number of particles per cell to a specific value. It should be noted that this value might be different for various grid resolution. In Fig. (4.12) similar influence on power spectra can be seen by increasing Smagorinsky constant to $C_s = 0.2$. Sohm [99] also ended up with $Cs = 0.2$ for accurate prediction of decay of homogeneous isotropic turbulence.

Fig. (4.13) depicts the longitudinal autocorrelation function. When no turbulence model is used the growth of autocorrelation function (the increase of the integral length scale) is nonphysical (as time passes it shows decreasing in correlation). Using VπLES the autocorrelation function shows reasonably good agreement with experiment at short and long distances. Although this coarse grid can not resolve the integral length scale sufficiently, the growing of the integral length scale is predicted well with the similar trend as in experiment. It should be noted that although the physical growing of velocity correlation can be obtained by using low order numerical scheme (see Fig. 4.9.d and 4.9.f), there is a huge over dissipation of small scale structures in these cases (see Fig. 4.9.c and 4.9.e). VπLES method as well as Smagorinsky SGS model with $Cs = 0.17$ properly resolve the growth of velocity correlation while preserve the small scale motions from over dissipation (see Fig. (4.11)). This result confirms that the energy transfer between large and small scales is properly resolved with VπLES and LES with Smagorinsky model in this coarse grid. Similar result for LES Smagorinsky were presented in [99] and [100].
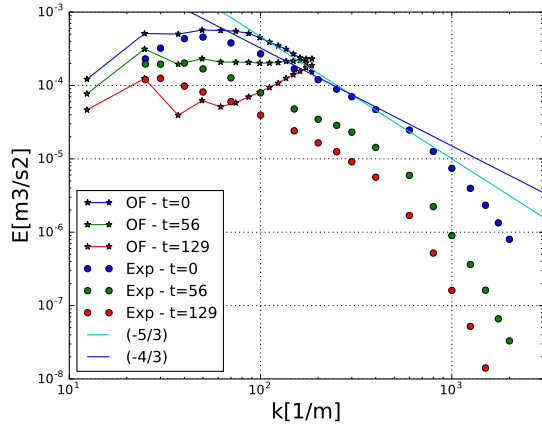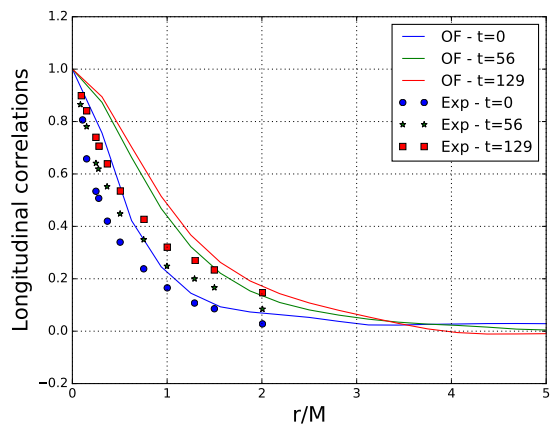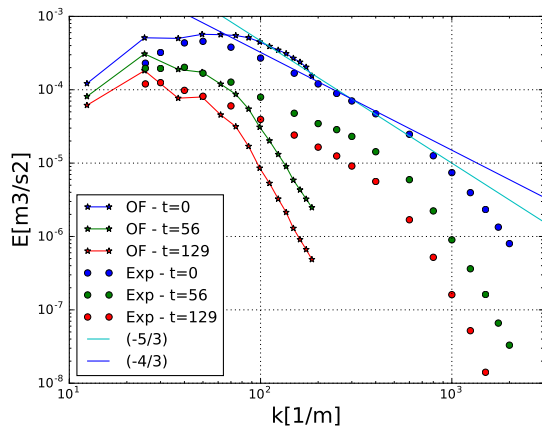
(a) pure grid simulation (32^3) - linear scheme
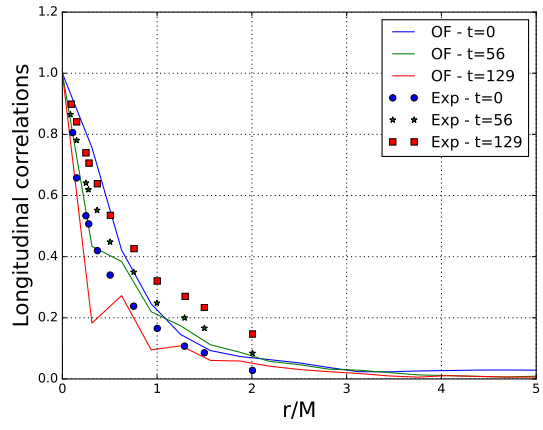
(b) pure grid simulation (32^3) - linear scheme
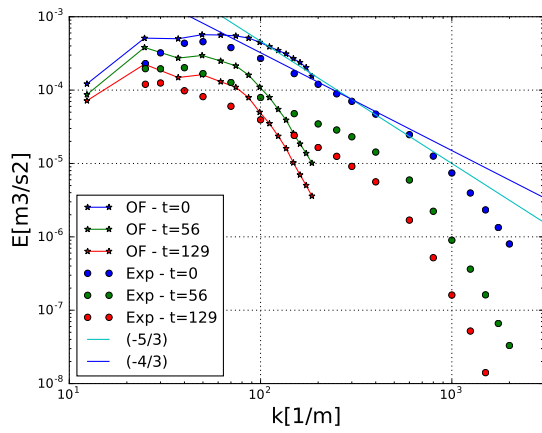
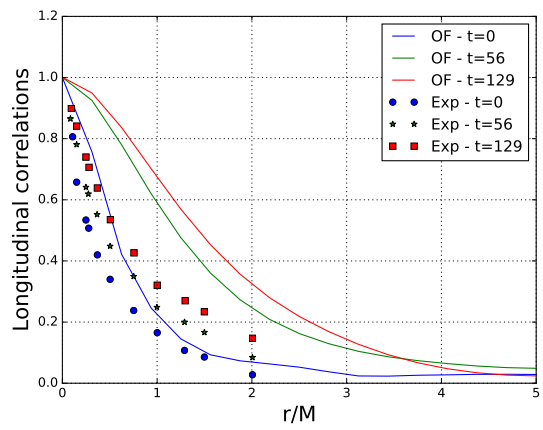(c) pure grid simulation (32^3) - linearUpwind scheme
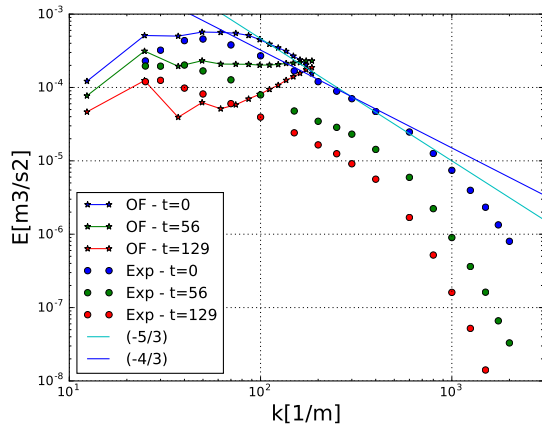
(d) pure grid simulation (32^3) - linearUpwind scheme
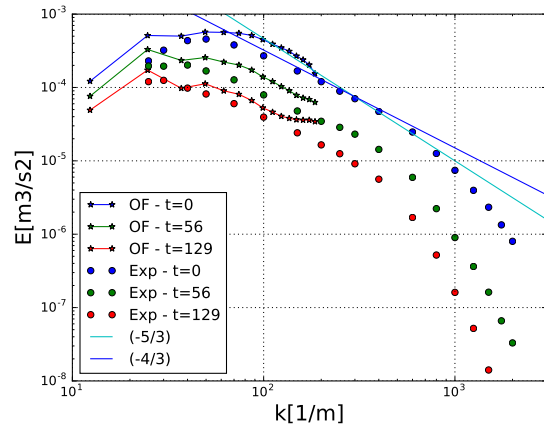
(e) pure grid simulation (32^3) - upwind scheme
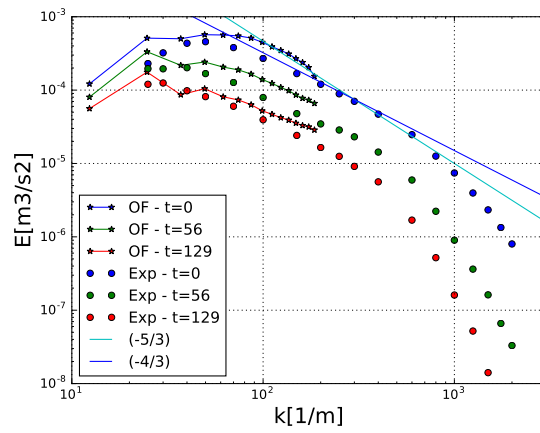
(f) pure grid simulation (32^3) - upwind scheme

Figure 4.9: Comparison of energy spectra of experiment and simulation for linear, linearUpwind and upwind scheme without using any turbulence model - grid resolution is 32^3.

(a) pure grid simulation (32^3) - linear scheme

(b) VπLES simulation (32^3) - linear scheme -2pt
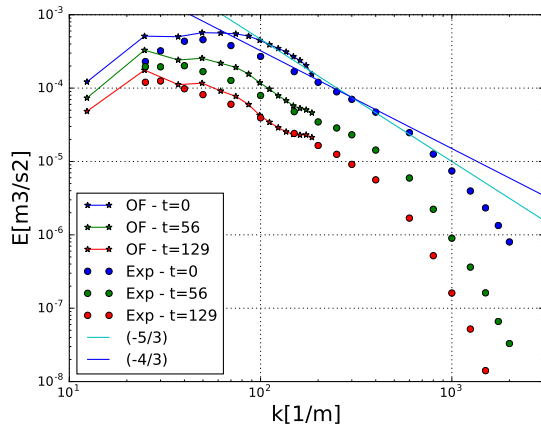

(c) LES Cs=0.17 - simulation (32^3) - linear scheme

Figure 4.10: Comparison of energy spectra of experiment and simulation with and without SGS model - grid resolution is 32^3.
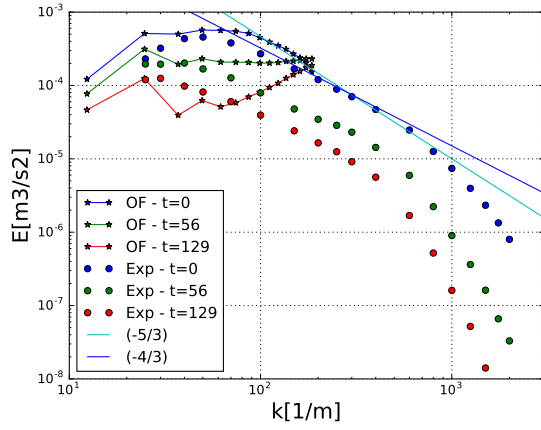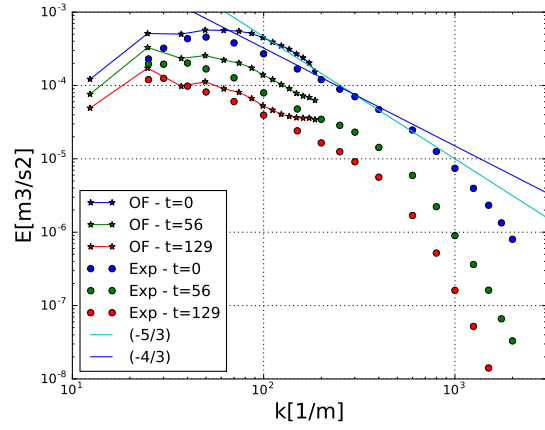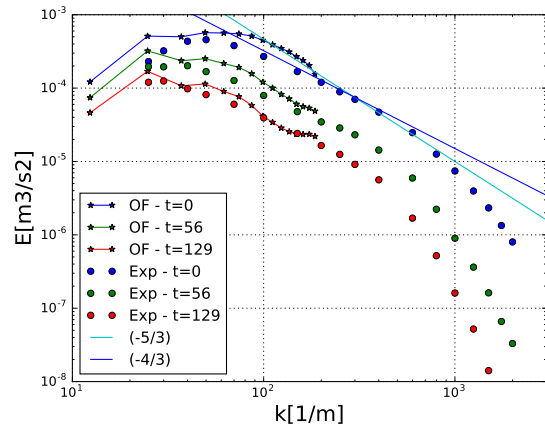
(a) pure grid simulation (32^3) - linear scheme
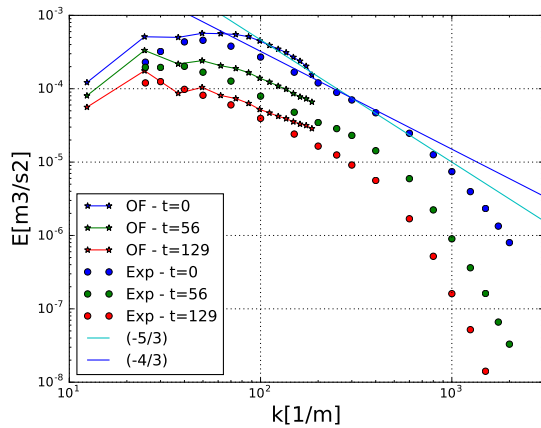

(b) VπLES simulation (32^3) - linear scheme -2pt
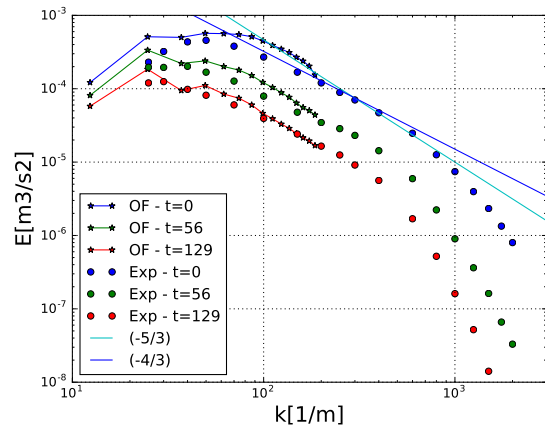

(c) VπLES simulation (32^3) - linear scheme -10pt

(d) VπLES simulation (32^3) - linear scheme -20pt

Figure 4.11: Investigating the influence of number of particles in each cell on the energy spectra evolution - grid resolution is 32^3.
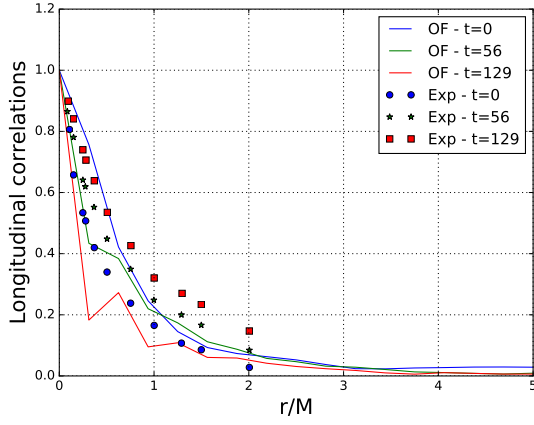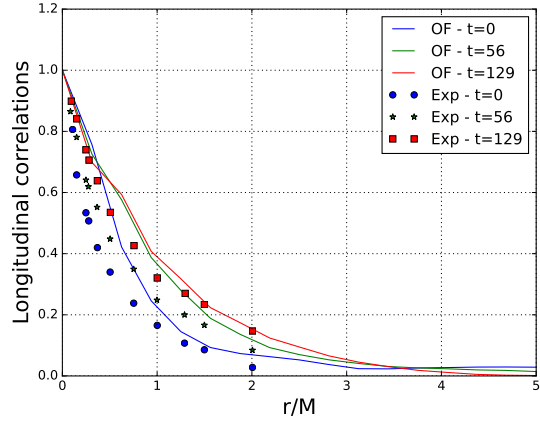

(a) LES Cs=0.17 - simulation (32^3) - linear scheme

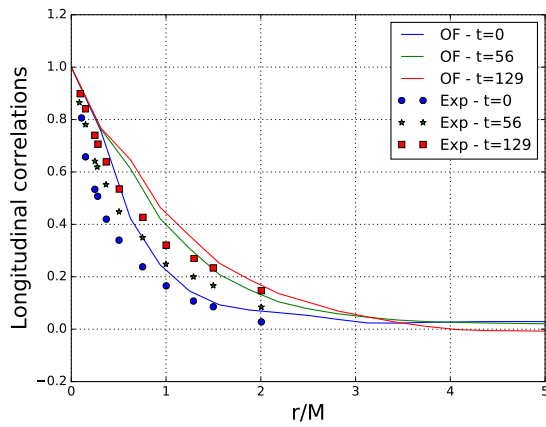(b) LES Cs=0.20 - simulation (32^3) - linear scheme

Figure 4.12: The influence of Smagorinsky constant C_s on the predication of the evolution of energy spectra - grid resolution is 32^3.
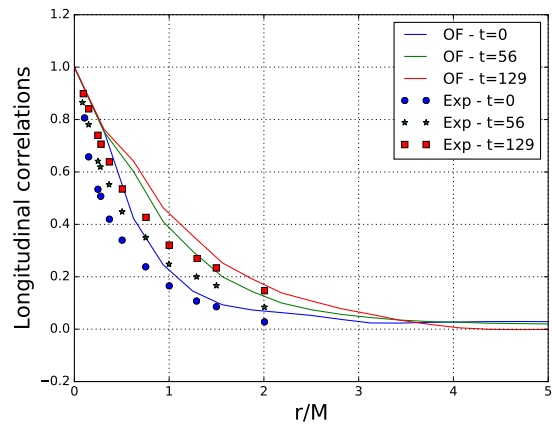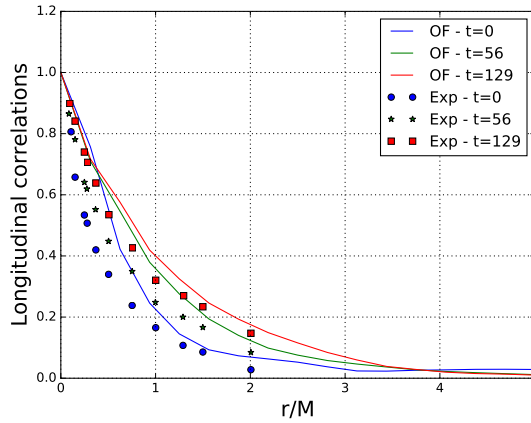
(a) pure grid simulation (32^3) - linear scheme

(b) VπLES simulation (32^3) - linear scheme -2pt

(c) VπLES simulation (32^3) - linear scheme -10pt

(d) VπLES simulation (32^3) - linear scheme -20pt

(e) LES Cs=0.17 - simulation (32^3) - linear scheme

Figure 4.13: Growing longitudinal velocity correlation - grid resolution is 32^3.

4.7 Influence of Grid Resolution

In this section VπLES method and LES Smagorinsky model are used with the cases with high grid resolution. Fig. (4.14) shows the decay of turbulent kinetic energy using grid resolution 64^3 with and without SGS model. The legend "pure grid simulation" means not using any turbulence model. Fig. (4.15) shows energy spectra evolution in grid resolution 64^3. In a case of not using any turbulence model (Fig. (4.15.a-b)) the energy spectra and autocorrelation growth are nonphysi-

cal and as time passes it shows decreasing in the velocity correlation. As already discussed this under-resolved grid can not resolve the subgrid scales and proper dissipation of energy can not be achieved. Consequently the accumulation and over prediction of kinetic energy happens at high frequency scales. Using subgrid scale model either through LES Smagorinsky model or VπLES drain energy from large scales in order to mimic the effects of the dissipation scales. Figure 4.14 shows the drain of energy from grid-based solution (large scales) using VπLES method for grid resolution 64^3.

As can be seen in Fig. (4.15.c-d) energy spectra is in a good agreement with experiment in inertial and dissipation range with using VπLES method. At the highest wave number the decay of energy does not follow the experiment exactly. The reason can be due to the simple diffusion model which is implemented in VπLES from work of Fukuda (see section (3.8)) in combination with CSM (see section (2.3.2.3)). Fig. (4.17) describes this pile-up with deeper investigation of energy exchanges of different scales. As it is shown the curve of energy of small scale vortex particles E^v growth with k when their size decreases due to the stretching. Further improvement of the result is possible by using more realistic diffusion model and more proper criterion for mapping back particles to the grid.

Figs. (4.16) and (4.18) show the energy spectra and autocorrelation function for cases with 128^3 and 256^3 grid cells without using turbulence model. Influence of VπLES method in fine grid is neglectable. In fine grid with 256^3 cells although the energy spectra follows well the experiment in dissipation range as well as inertial range, correlation of velocity doesn't grow well with physical rate. In the other word the lack of any numerical viscosity due to fine resolution and less diffusive scheme as well as not using any turbulence model result in a nonphysical and negligible growth of integral length scale in case of 256^3 grid cells.
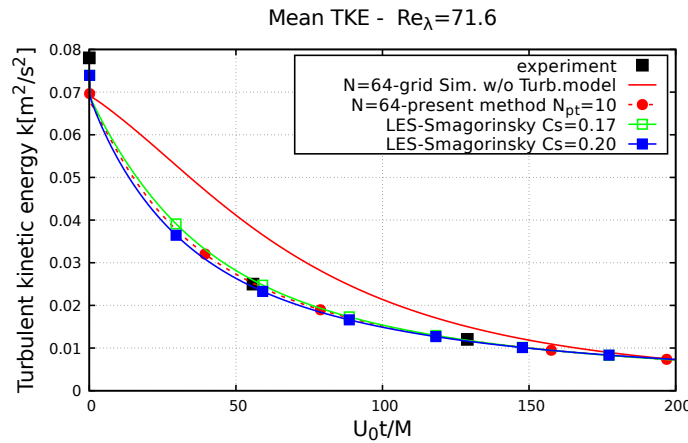

Figure 4.14: Decay of spatially averaged turbulent kinetic energy - grid resolution 64^3
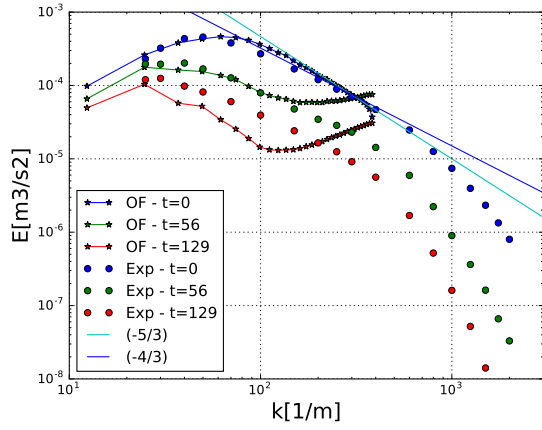
(a) pure grid simulation (64^3) - linear scheme
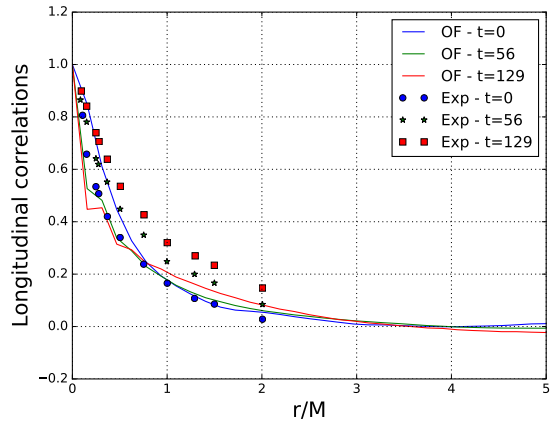
(b) pure grid simulation (64^3) - linear scheme
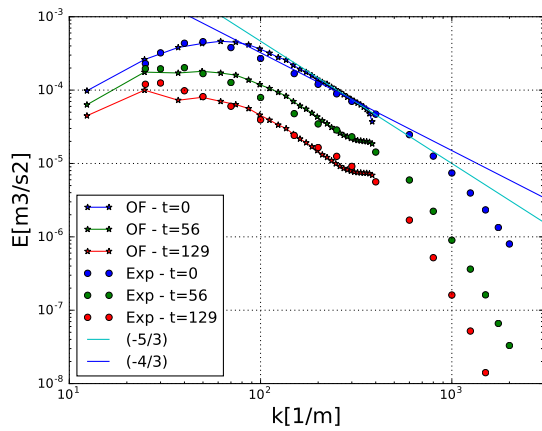
(c) VπLES simulation (64^3) - linear scheme -1pt
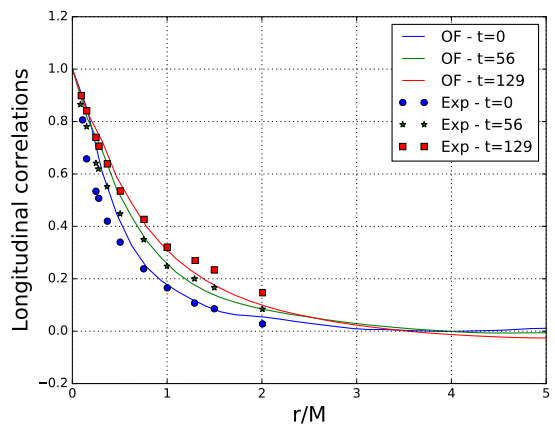
(d) VπLES simulation (64^3) - linear scheme -1pt

(e) LES Cs=0.17 - simulation (64^3) - linear scheme

(f) LES Cs=0.17 - simulation (64^3) - linear scheme

Figure 4.15: Energy spectra during decay of turbulence in a cubical box - grid resolution 64^3 cells

(a) pure grid simulation (128^3) - linear scheme

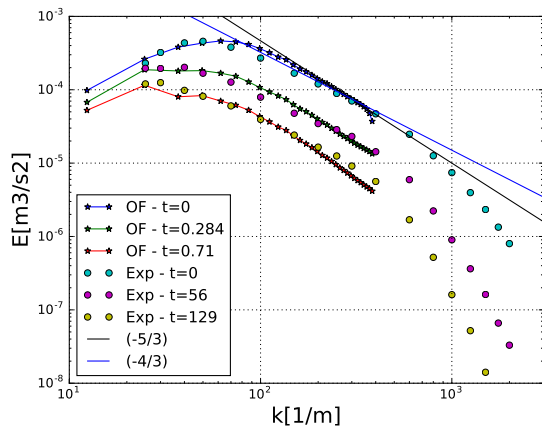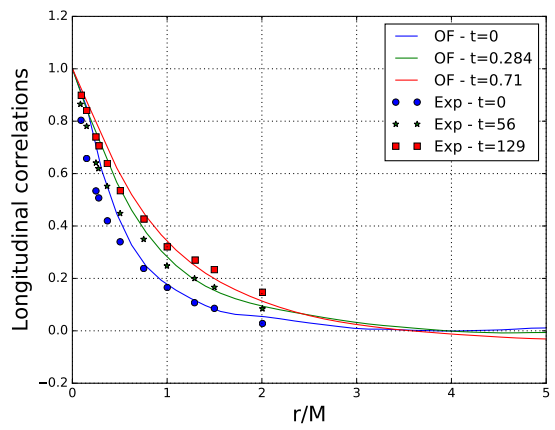(b) pure grid simulation (128^3) - linear scheme

(c) VπLES simulation (128^3) - linear scheme -1pt
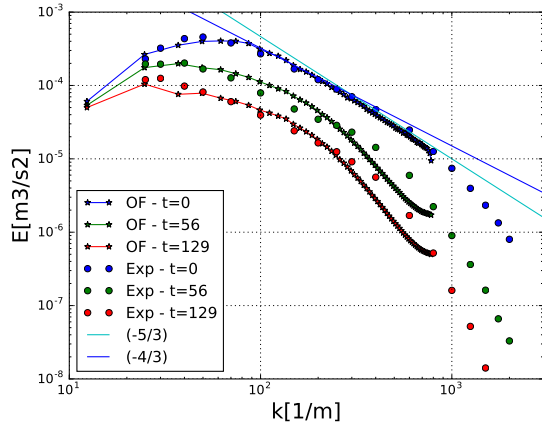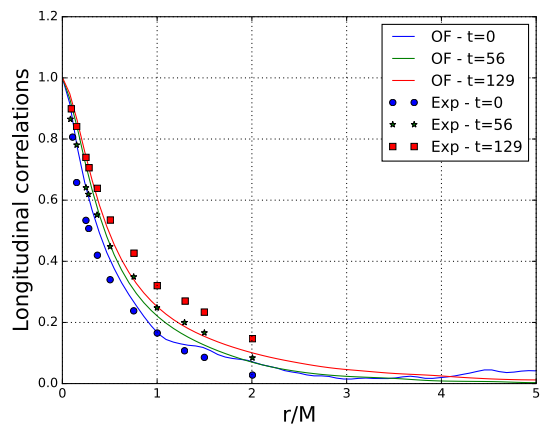
(d) VπLES simulation (128^3) - linear scheme -1pt
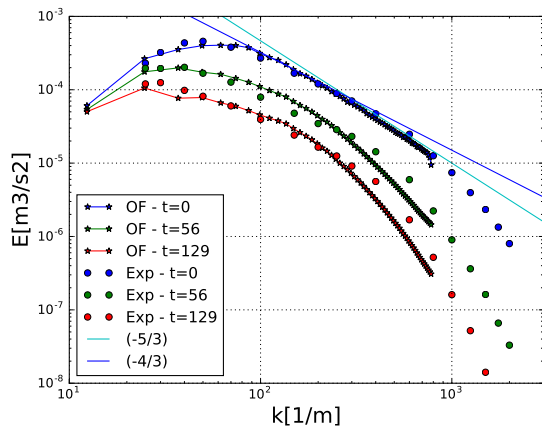
(e) LES Cs=0.17 - simulation (128^3) - linear scheme
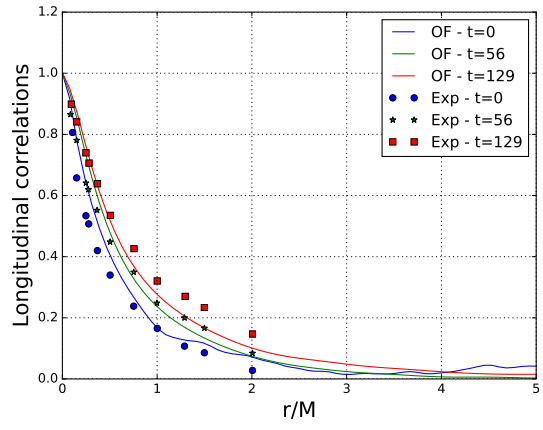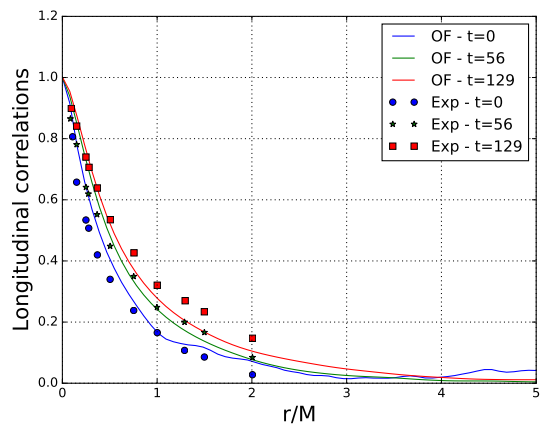
(f) LES Cs=0.17 - simulation (128^3) - linear scheme

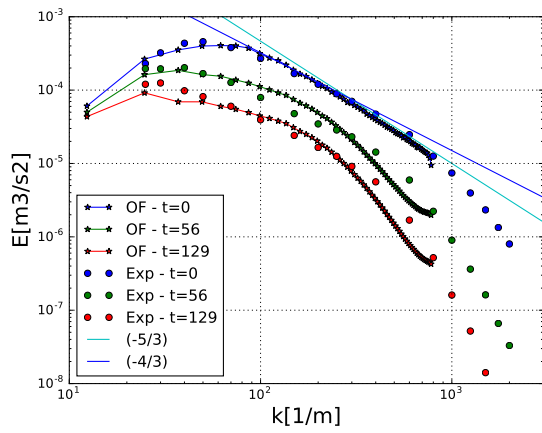Figure 4.16: Energy spectra during decay of turbulence in a cubical box - grid resolution 128^3 cells
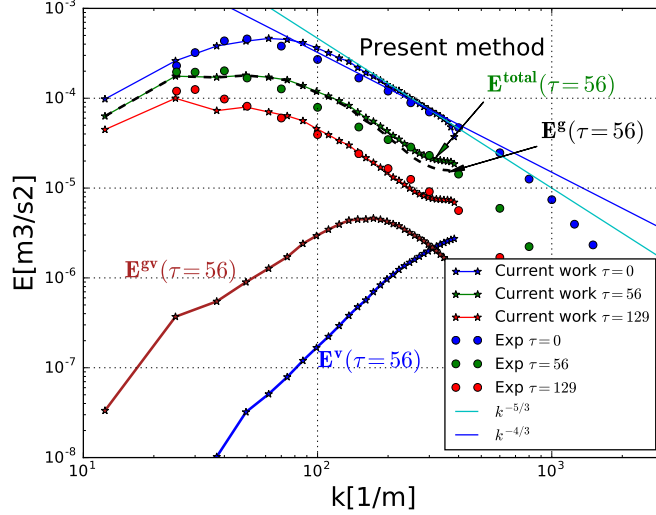
(a)

Figure 4.17: Spectrum E obtained using three different methods with grid resolution 64^3. $E^g = \frac{1}{2}(\mathbf{u}^g\mathbf{u}^g)$, $E^v = \frac{1}{2}(\mathbf{u}^v\mathbf{u}^v)$ and $E^{gv} = E - E^g - E^v$ are different contributions to the spectrum (middle picture).
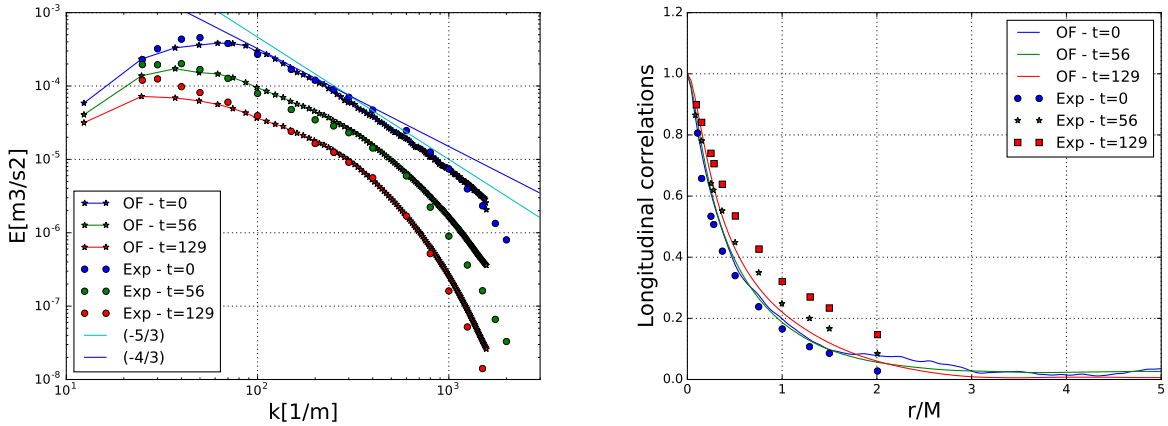
(a) pure grid simulation (256^3) - linear scheme

(b) pure grid simulation (256^3) - linear scheme

Figure 4.18: Energy spectra during decay of turbulence in a cubical box - grid resolution 256^3 cells

## 4.8 Capturing fine scales

Probability density function of the vortex sizes σ is presented in Fig. (4.19) at different time steps. As seen, there is a big variety of fine vortices with sizes ranging from 0.1Δ to Δ. This is an illustration of the fact that the VπLES method is capable of resolving scales an order less than the grid cell size even at small $N_{pt} = 4$. The vortices smaller than 0.1Δ are excluded by selection of strongest vortices in cells and restriction of N_{pt}. In principle, they could be much smaller. The only restriction is the computational time and memory space. Resolution of the vortices with $\sigma \approx 0.1\Delta$ in pure grid-based methods would require grids with number of cells at least 10^4 larger than in the VπLES simulations provided each vortex would be represented only by three cells. The largest vortex size of 4Δ is a specific feature of the present algorithm, because if $\sigma > 4\Delta$ the vortex particle is mapped back to the grid. The p.d.f distribution is shifted towards larger σ in time. This tendency is due to temporal growth of the structures in the grid based flow which is in accordance with widening of the autocorrelation function (e.g. fig. (4.15)) and increase of the integral length.
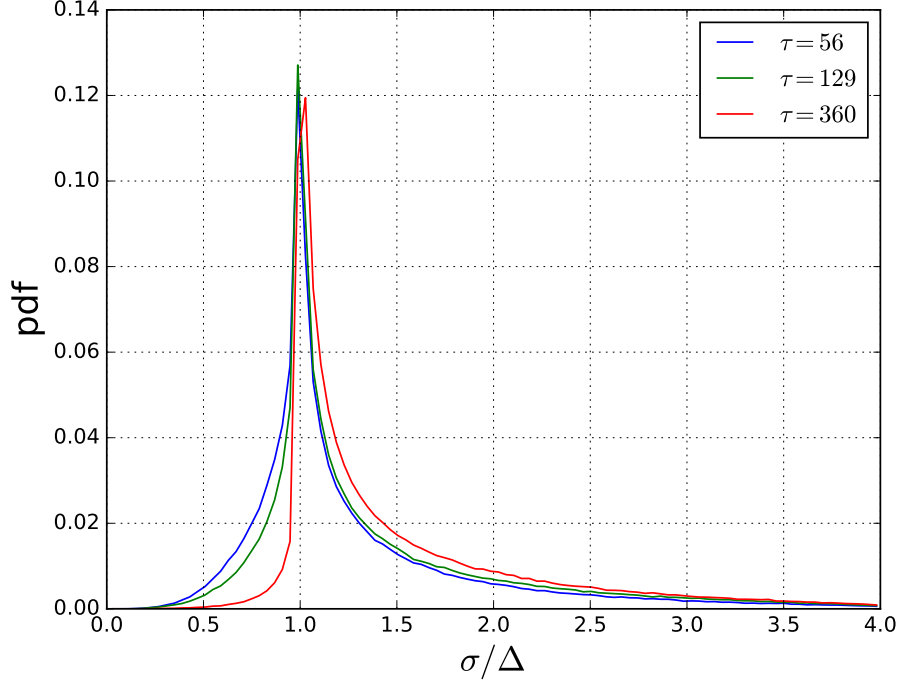
Figure 4.19: Distribution of initial scalar field

4.9 Influence of the inner interaction between vortex

As mentioned in section (2.3.2.5) the computational cost of the calculation of the velocity induced by vortex particles using Biot-Savart law is a well known limitation of the Lagrangian vortex particle method. The number of required operations is proportional to $\mathcal{O}(N^2)$ for N number of particles in each time step. Within the present approach the calculation of $\frac{\partial u_i^v}{\partial x_j}$ and the velocity induced by particle on each other $\mathbf{u}_p^v$ (Eqs. (3.32) and (3.33)) is the largest time consuming part of calculations with $\mathcal{O}(L^2 N_{pt}^2)$ operations, where L is the number of adjacent neighboring cells. Thus, it is necessary to estimate the importance of these calculations on the spatially averaged results. Fig. (4.20) shows results obtained when the inner interaction between particles is neglected and they are driven only by the grid-based flow. With this assumption the Eq. (3.13) reduces to:

$$\frac{d\boldsymbol{\omega}^v}{dt} = (\boldsymbol{\omega}^v \cdot \nabla)\mathbf{u}^g + \nu \Delta \boldsymbol{\omega}^v \tag{4.6}$$

$$\frac{d\mathbf{r}_i}{dt} = \mathbf{u}_i^g \tag{4.7}$$
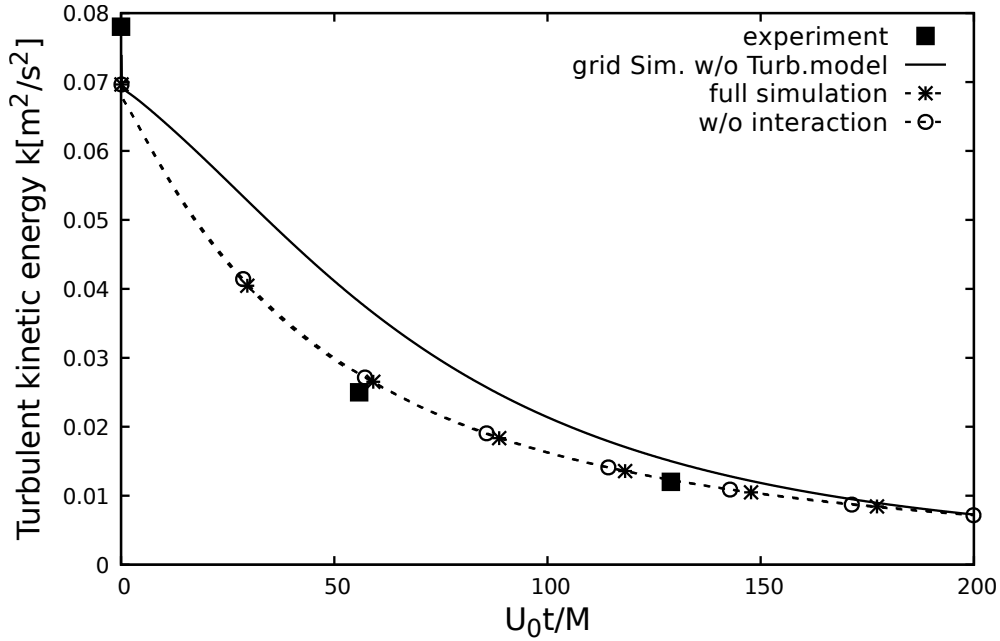
Figure 4.20: Influence of interaction between vortex particles on the spatially averaged kinetic energy

Fig. (4.20) shows that the influence of inner interactions on spatially averaged kinetic energy and scalar dissipation rate is relatively weak and can be neglected in the calculation. Thereby the computations can be done sufficiently faster without lost of accuracy. It seems to be that the vortex particles serve just as triggers of turbulence and their inner interaction does not contribute sufficiently to the flow evolution. This issue should thoroughly be studied in future works for more complex flows. The insignificance of the interaction reduces the importance of the increase of the scheme accuracy for the integration of the particle trajectory and particle strength equations. The simple Euler method can be used as the most simple and fast procedure.

4.10 Influence of the Number of particles per cell N_{pt}

One of the weaknesses of particle methods is the presence of free parameters which are often tuned to match desirable results. Strictly speaking, the number of particle per cell N_{pt} is not a freely selectable parameter within the VπLES method. It should be as large as possible. Fig. (4.21) shows the convergence of numerical results for k when N_{pt} increases. The spatially averaged kinetic energy is independent of N_{pt}. Such a saturation indicates that the numerical results become independent of N_{pt} after some relatively small threshold value $N_{pt} \approx 4$.
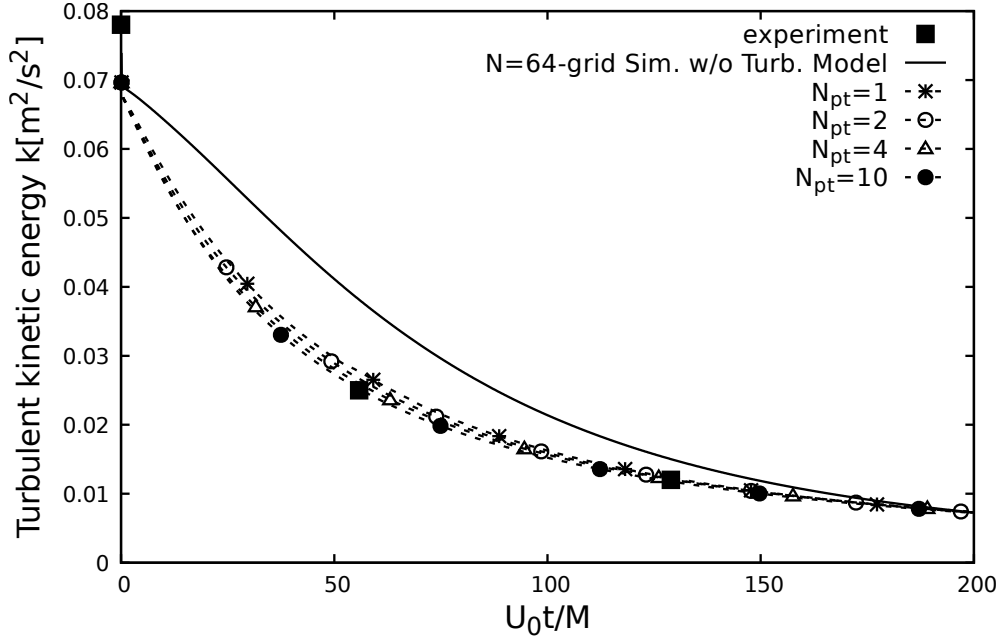
Figure 4.21: Influence of the parameter N_{pt} on the spatially averaged kinetic energy

4.11 Conclusion

This chapter presented the results of the validation of the method for a well tried benchmark test of the decaying homogeneous isotropic turbulence using the experimental data of Comte-Bellot and Corrsin (1971) [98]. A very important conclusion of validation is that the spatially averaged term $\overline{\mathbf{u}^v \times \boldsymbol{\omega}^g}$ which describes the influence of fine scales on large ones, behaves as an energy drain transferring the energy of the grid based motion into the fine scales energy. At coarse resolutions, it acts as a diffusive Large Eddy Simulation subgrid model resulting in a LES-like behavior of the whole method. When the resolution increases, the present method is consistent and converges to the DNS. It was shown that the present method is capable of resolving scales much less than the grid cell size. In such a way, very fine scales can be resolved on coarse grids. The plausibility of simulations were successfully checked for the second order statistics, i.e. for the spectral density E and the longitudinal autocorrelation coefficient. $V\pi$LES method can preserve energy at high wave number motions (small scales) while pure grid simulation (or under-resolved DNS) shows instability in numerical simulation due to the accumulation of kinetic energy. Using more diffusive numerical scheme like upwind in pure grid simulation can remove the pile-up in the energy spectral at middle range structure but results in a strong decay in energy of small scale structures (see Fig. (4.9)). The methodical study demonstrated that the inner interaction between particles can be neglected at least for the test case considered in this chapter (see Fig.(4.20)). This results in a very efficient and fast computational procedure. Next chapter validate $V\pi$LES method for the case of turbulent circular jet through comparison with several measurements of mean velocity and velocity fluctuations along the jet center line.

5 Free turbulent jet flow

In this chapter, the results of free jet flow simulation at $Re = 10^4$ with and without VπLES as well as comparison with two SGS models (Smagorinsky and dynamic Smagorinsky) are presented. Section (5.1) is entirely dedicated to the high resolution grid simulation with 6.04Mio mesh cells. The case with high resolution grid is used for accurate prediction of the free jet flow evolution and to study the effect of inflow conditions on the variation of mean and r.m.s of axial velocity along the jet centerline. LES with dynamic Smagorinsky model is used for high resolution grid-based simulation. Dynamic Smagorinsky SGS model is already proven to have a good performance in predicting the evolution of turbulent free jet flow [105]. The influence of the inflow condition such as momentum thickness at the nozzle exit and adding random fluctuations to the mean velocity profile on the jet flow evolution is investigated in details in sections (5.1.4) and (5.1.6). Validation of result is performed through comparing with experiment of [9], [7] and [10]. The influence of domain size in radial direction on the development of velocity fluctuations is also investigated. The result of section (5.1) is later used as a reference in case there is no experimental data available. In section (5.2) VπLES method is used for numerical simulation of turbulent free jet flow with coarse grid. The performance of VπLES on two coarse grids named Grid I $\approx$ 114k and Gird II $\approx$ 150k mesh cells are evaluated through comparison with two classical SGS model on the same mesh resolution. The results presented in section (5.2) show a superior performance of VπLES method in comparison with pure grid-based simulation using Smagorinsky and dynamic Smagorinsky model with relatively coarse grid.

5.1 Pure grid-based simulation

5.1.1 Inflow condition

Fig. (5.1) shows the jet inflow profile. The jet inlet velocity profile consists of a constant velocity U_j in the jet core region and a laminar Blasius profile near the wall to be consistent with experimental work of [9], [7] and [10]. Three different momentum thicknesses are applied to cover a shear layer thickness in experiment. $D/\theta = 50$, $D/\theta = 120$, $D/\theta = 180$ are considered for the boundary layer thickness where θ is an initial momentum thickness at the nozzle exit and D is the nozzle diameter. The instantaneous velocity profile at the inlet at each time step is defined as follows:

$$\mathbf{u}_{inlet}^n(\mathbf{r}, t) = \mathbf{u}_{profile}^n(\mathbf{r}, t) + \mathbf{u}_{disturbances}^n(\mathbf{r}, t) \tag{5.1}$$

In several literature the time-averaged stream-wise velocity profile given by Michalke and Hermann [106] which is known as tangent hyperbolic profile is used for $\mathbf{u}_{profile}^n(\mathbf{r}, t)$ in Eq. (5.1). In this work as already mentioned different profiles which are shown in Fig. (5.1) are applied at the inlet of computational domain following the work [105]. $\mathbf{u}_{disturbances}^n(\mathbf{r}, t)$ is a background disturbances or fluctuations which are randomly distributed in space at the jet exit. In the present study random Gaussian fluctuations with an rms (amplitude) value of 0.1% of the mean velocity ($u' = 0.001U_j$) are superimposed to the reference (mean) velocity field. This amount of disturbances is consistent with the experimental work of Russ & Strykowsky (1993) [7]. Unfortunately, both in experiment of [7] and LES of [105] there are no quantitative information about the integral lengths and spectrum at the nozzle orifice which are necessary to generate inlet signal with account for the second order statistics. Since the results of simulations agree well with both measurements of Russ & Strykowsky (1993) [7] and LES simulation of Kim and Choi (2009) [105] at the same grid resolution as well as because of lack of additional inflow information no more advanced inflow generation technique was utilized.
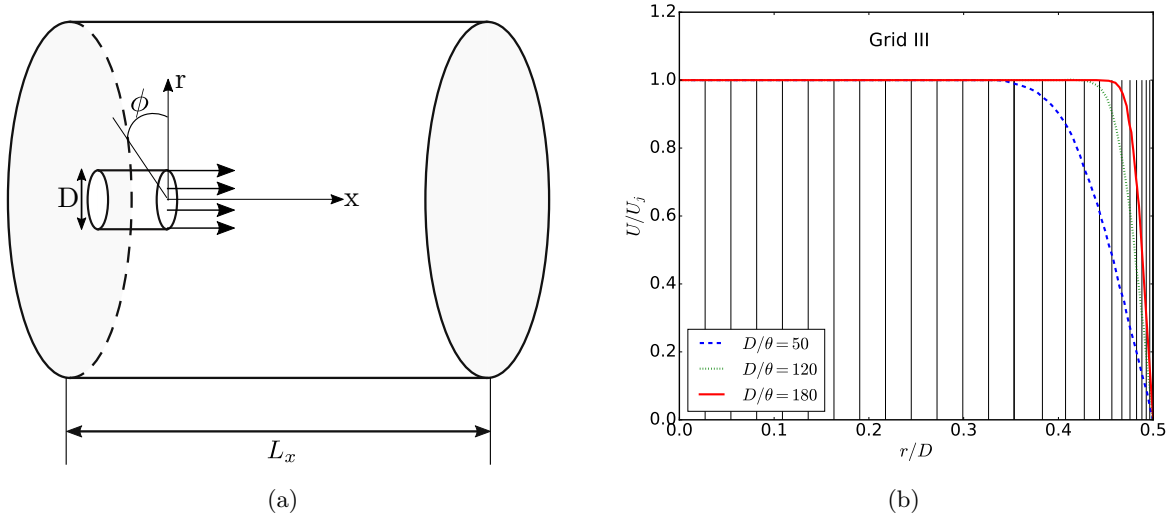
Figure 5.1: a) Schematic view of computational domain. b) Mean axial velocity profile at the nozzle exit with tree different momentum thicknesses. Vertical lines show the grid lines of the Grid III

5.1.2 Numerical set up

The choice of the computational domain, grid and numerical setup are based on the work of [105]. Totally six different non-uniform grids were generated for this investigation (see table 2). Two coarse grids named Grid I $\approx$ 114k and Gird II $\approx$ 150k mesh cells are considered to evaluate the performance of VπLES method. One high resolution grid Grid III $\approx$ 6.04 Mio is also considered to be reference for comparison with coarse grid results. Next three grids IV-VI are used for the grid convergence study in pure grid simulations. Non-uniform grid is distributed in axial and radial directions. In order to resolve velocity gradient in shear layer the concentration of grid points in shear layer are higher than in other locations in radial direction (see Fig. (5.2)). Also in axial direction grids are clustered at the nozzle exit. In circumferential direction the grids are uniform. The high resolution grid named here Grid III with LES dynamic Smagorinsky model is used throughout section (5.1) to study the flow details of free jet flow at $Re = 10^4$. The spatial discretization of the convective term (see Eq. (2.2)) was performed using the second order central difference scheme (CDS) or linear scheme in OpenFOAM. For the time discretization a mixed scheme based on the Euler (10 percent) and Crank-Nicolson (90 percent) schemes was used. The Courant number was kept less than 0.3 in all simulations. To get stable and robust results the simulation is started with a more diffusive upwind scheme for the convective term. As soon as the simulation becomes stable (after $\approx$ 3 sec) the CDS scheme is applied to the convection term. The time averaged values are calculated from 5 sec to 25 sec when the second order scheme has been utilized for convection discretization.

Grid	Grid points in streamwise x, radial r and circumferential ϕ directions	Total number of grid cells	$\Delta r_{min}/D$	$\Delta x_{min}/D$
I	$128(x) \times 31(r) \times 28(\phi)$	114,716	0.0100	0.0598
II	$128(x) \times 41(r) \times 28(\phi)$	149,436	0.0068	0.0598
III	$460(x) \times 132(r) \times 106(\phi)$	6,040,112	0.0030	0.0167
IV	$234(x) \times 68(r) \times 66(\phi)$	1,000,000	0.0083	0.0327
V	$328(x) \times 94(r) \times 92(\phi)$	2,800,000	0.0044	0.0233
VI	$552(x) \times 160(r) \times 128(\phi)$	10,600,000	0.0025	0.0137

Table 2: Grid parameters.
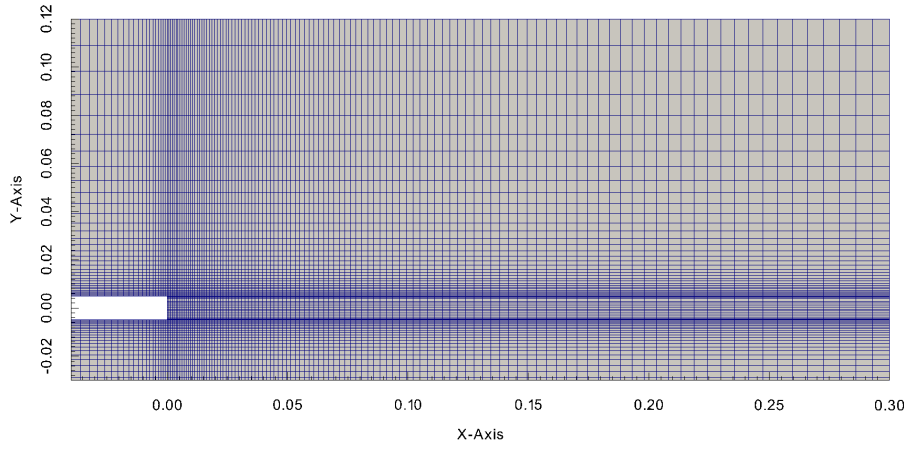
Figure 5.2: Distribution and clustering of the grid close to nozzle exit, Gird II.

5.1.3 Influence of domain size on the evolution of r.m.s of velocity fluctuation

In order to have proper domain size in radial direction three different domain extension in radial direction are examined. Fig. (5.3) shows that the extension of computational domain to $r/D = 15$ keeps the surrounding walls far enough from the jet centerline to diminish the wall effect. In this case the evolution of axial fluctuation follows well the experimental result. Computational domain with $r/D = 15$ and $x/D = 30$ was chosen for further numerical study in this chapter.
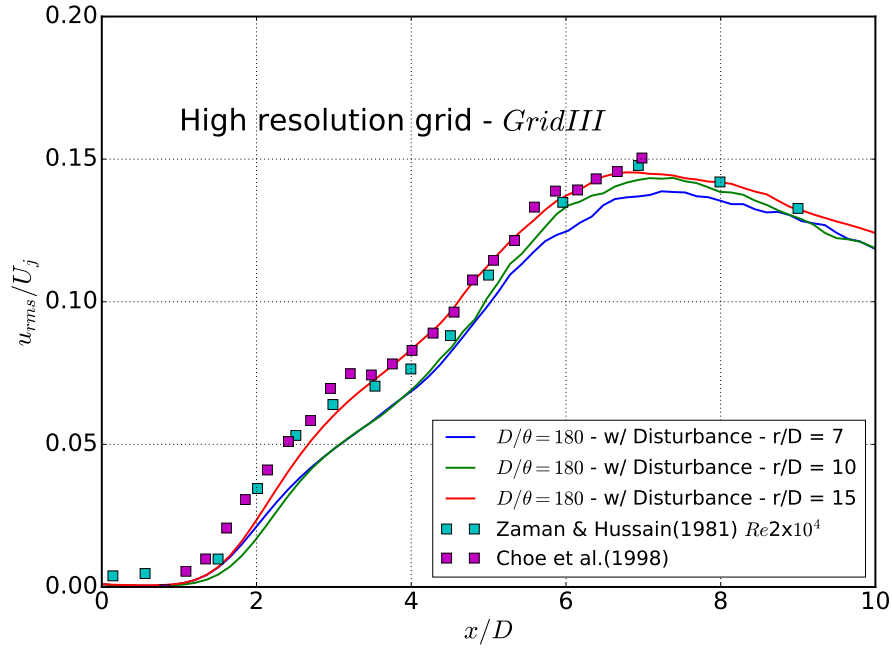
(a) Influence of domain size on the evolution of r.m.s of velocity fluctuations

Figure 5.3: r.m.s of axial velocity fluctuations along the jet centerline

5.1.4 Influence of momentum thickness on mean axial velocity and velocity fluctuations

To evaluate the degree of jet mixing one can refer to the evolution of jet centerline velocity as an important identification factor for the jet mixing. Fig. (5.4) shows the decay of time averaged stream-wised velocity along the jet center line. By increasing the momentum thickness a more

rapid decay happens from $D/\theta = 50$ and $D/\theta = 180$. This is due to the earlier formation of large scale structure as shown in Figs (5.7) and (5.8). Similar dependence of mean axial velocity decay on the initial momentum thickness at $Re = 10^4$ was reported and discussed by Kim & Choi (2009) [105]. So inflow condition such as momentum thickness is an important factor in determining the jet mixing and decay rate of mean axial velocity.
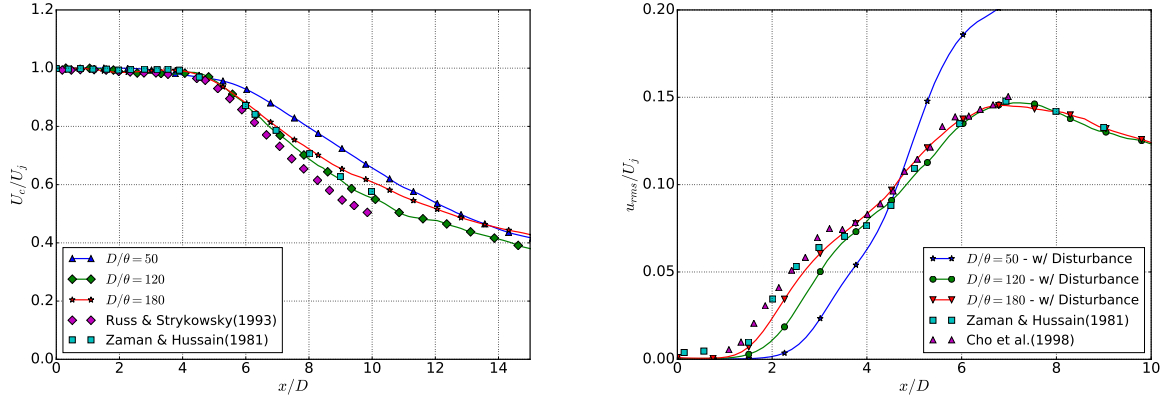
(a) Influence of momentum thickness on mean axial velocity - $Re10^4$

(b) Influence of momentum thickness on the evolution of r.m.s of velocity fluctuations

Figure 5.4: Variation of mean and r.m.s of axial velocity fluctuations, comparing with experiments of Russ & Strykowski (1993) [7] $Re = 10^4$ and $D/\theta = 110$, Zaman & Hussain (1981) [8] $Re = 2 \times 10^4$ and $D/\theta = 120$ [9], Choa et al. (1998) [10] $Re = 2 \times 10^4$ and $D/\theta = 200$.

5.1.5 Influence of grid resolution

In order to study the grid convergence several OpenFOAM simulations with Dynamic Smagorinsky model are carried out for four grids with $D/\theta = 180$. Fig. (5.5) shows the results for decay of time-averaged axial velocity and the r.m.s of velocity fluctuation. The result are converged already for the Grid III with 6.04Mio mesh cells and further refinement does not have important influence on results. Therefore, pure grid-based simulations with Grid III and $D/\theta = 180$ are used further as a reference to evaluate the efficiency of the VπLES method.
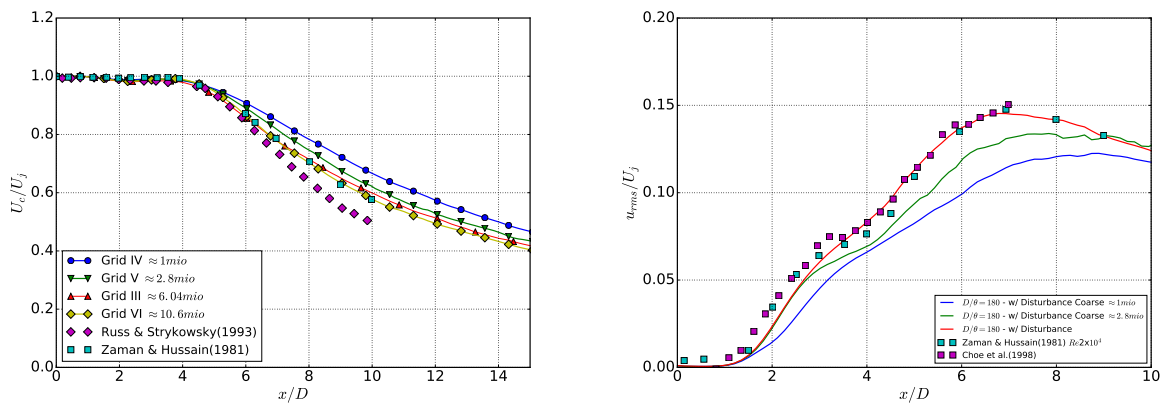
(a) Time-averaged axial velocity along the jet centerline

(b) r.m.s of axial velocity fluctuations along the jet centerline

Figure 5.5: Influence of grid resolution on mean axial velocity and r.m.s - $Re10^4$

5.1.6 Influence of background disturbances on the evolution of mean axial velocity and r.m.s of velocity fluctuation

Figs (5.6) shows the influence of superimposed velocity fluctuation ($\mathbf{u}^n_{disturbances}(\mathbf{r}, t)$ in Eq. (5.1)) on the evolution of free jet flow. In the absence of background disturbances strong coherent ring like structures are created behind the nozzle and propagates without visible breakdown to a long distance downstream. They induce large velocity fluctuations. On the other hand, forced background disturbance results in the formation of small ring close to nozzle exit and finer structures in downstream. This high frequency perturbations at the inlet leads to an earlier saturation (breakdown) of vortex ring as shown in Figs. (5.7) and (5.8) consequently smaller r.m.s values in downstream locations are obtained. Fig. (5.6) shows that by imposing disturbances at the nozzle exit (inlet of computational domain) evolution of velocity fluctuations along the jet center line reproduces the result of experiment more accurately.
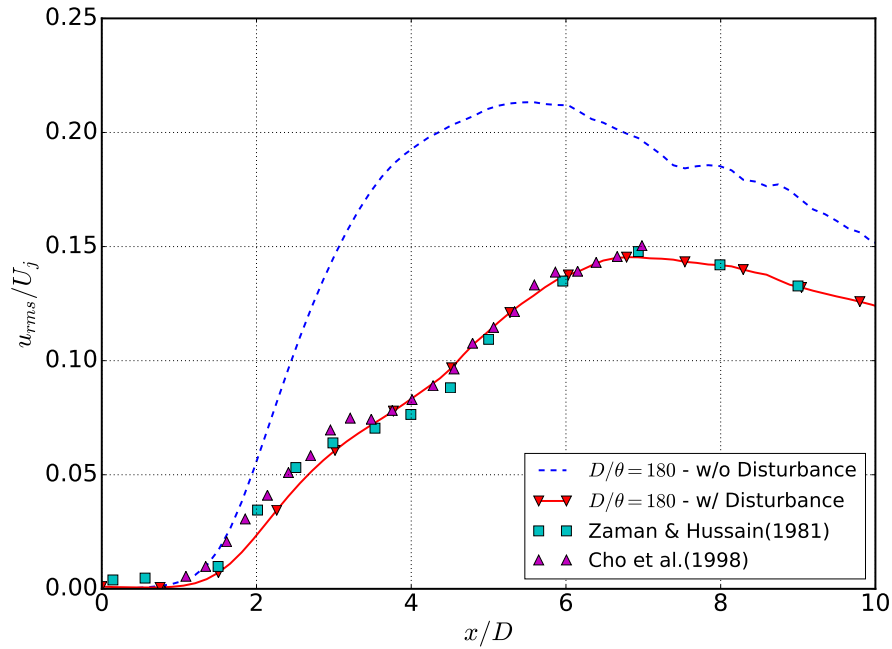
Figure 5.6: Influence of background disturbances on the evolution of r.m.s of velocity fluctuations

5.1.7 Influence of momentum thickness on evolution of vortical structures

As shown in Figs. (5.7) and (5.8) with increasing D/θ the formation of vortex ring occurs earlier. This happens due to the higher instability of the thin shear layer ($D/\theta = 180$) at the nozzle exit. This result is consistent with observation of Kim and Choi (2009) [105].
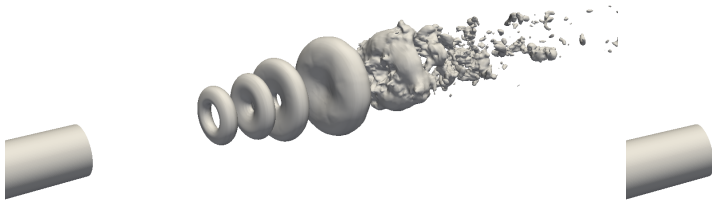
(a) $Re = 10^4, D/\theta = 50$ w/o background disturbances
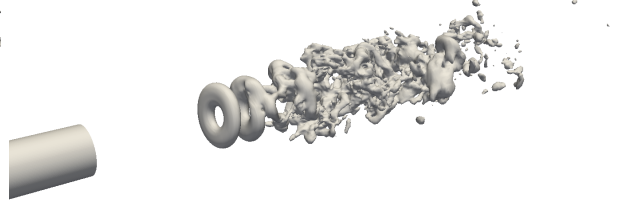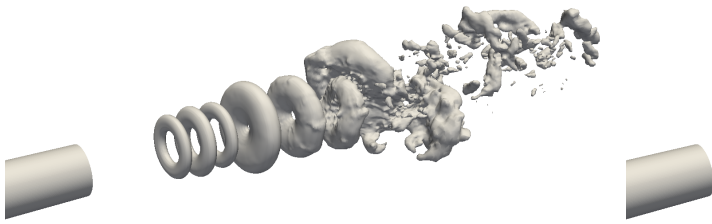
(b) $Re = 10^4, D/\theta = 50$ w/ background disturbances

(c) $Re = 10^4, D/\theta = 120$ w/o background disturbances
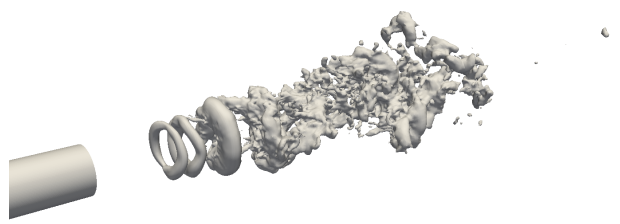
(d) $Re = 10^4, D/\theta = 120$ w/ background disturbances
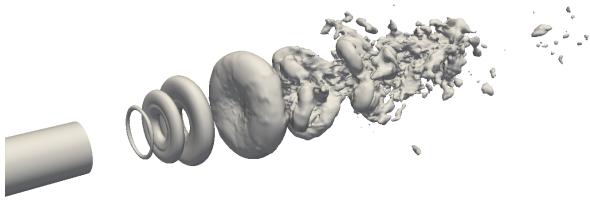
(e) $Re = 10^4, D/\theta = 180$ w/o background disturbances
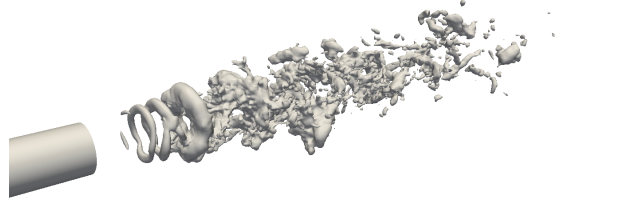
(f) $Re = 10^4, D/\theta = 180$ w/ background disturbances

Figure 5.7: Instantaneous vortical structure of Iso-surface of pressure $p/\rho U_j{}^2 = -0.3$, $Re = 10^4$
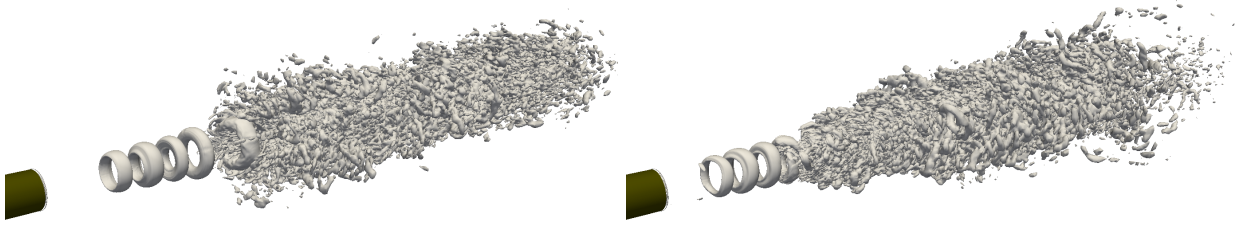
(a) $Re = 10^4, D/\theta = 50$ w/o background disturbances
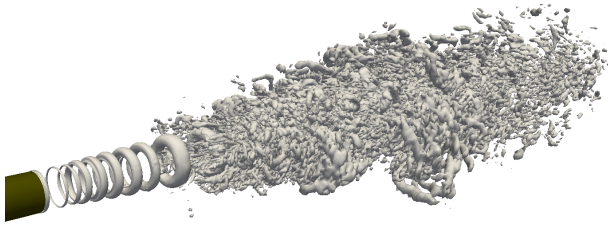
(b) $Re = 10^4, D/\theta = 50$ w/ background disturbances

(c) $Re = 10^4, D/\theta = 120$ w/o background disturbances

(d) $Re = 10^4, D/\theta = 120$ w/ background disturbances
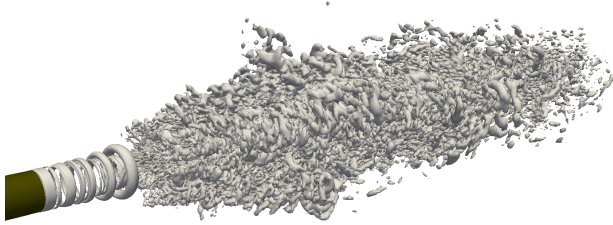
(e) $Re = 10^4, D/\theta = 180$ w/o background disturbances

(f) $Re = 10^4, D/\theta = 180$ w/ background disturbances

Figure 5.8: Instantaneous vortical structure visualized by Q criterion, $Re = 10^4$

5.2 VπLES ; Hybrid grid-based grid-free simulation

In this section the performance of newly developed hybrid grid-based grid-free method called VπLES is being investigated. VπLES method was applied on Grid I and Grid II in order to solve the dynamic of small scale motions through computational vortex method and two-way coupling with dynamic of large scale ones. Two pure grid-based simulations were also performed using Smagorinsky and dynamic Smagorinsky to model the effect of small scale motion on large structures. The result of these two different approaches in treatment of small scales effect are presented in the following sections. All VπLES results were obtained with $N_{pt} = 4$. In section (4.10) the definition and importance of N_{pt} was already discussed. Section (5.1.4) shows that the inflow conditions such as initial momentum thickness and the background disturbances has a great influence on the evolution of axial velocity fluctuations along the jet centerline. As conclusion the initial momentum thickness

of the value of $D/\theta = 180$ shows more accurate agreement with experiment. In the simulation of free jet flow with VπLES the initial momentum thickness is considered as $D/\theta = 180$ at nozzle exit. It should me mentioned that in case of the simulation with VπLES method, turbulence is developed without initial perturbation (background disturbances). The small scale vortices modeled by vortex method are proved to be capable to trigger the turbulence.

5.2.1 Hybrid method - evolution of mean axial velocity and r.m.s of velocity fluctuation along the jet centerline - Grid I

Fig. (5.9.a) shows the decay of mean axial velocity using Grid I with three different SGS models and one case without using any turbulence model (DNS on coarse grid). As can be seen the rate of decay with VπLES is more physical in comparison to other methods. It is due to the smaller length of potential core which itself is the result of more proper prediction of the jet instability. Smagorinsky with $C_s = 0.17$ is very diffusive and predict very long and stable potential core. In the current work the $C_s = 0.06$ was considered for Smagorinsky constant in the simulations. Fig. (5.15) shows that the Smagorinsky model has longer potential core length and consequently slow decay of mean axial velocity (see Fig. (5.9)) and a very low value for fluctuation at the near jet exit region. Fig. (5.9.b) shows a very good agreement between VπLES method and experimental result until $x/D = 5$ whereas other SGS models show very big discrepancy in the region near to nozzle exit. As can be seen in Fig. (5.15) the smaller length of potential core in case of VπLES method results in occurring an earlier instability and higher value of fluctuating at the near jet exit. Since VπLES method differs from the case of without SGS model (under-resolved DNS) only in the presence of the coupling term $\overline{\mathbf{u}^v \times \boldsymbol{\omega}^g}$, difference between two simulations directly illustrates the effect of this coupling term. Coupling term $\overline{\mathbf{u}^v \times \boldsymbol{\omega}^g}$ in VπLES provokes a more earlier jet breakdown and a correct formation of fluctuations starting directly from the nozzle. By refining Grid I in a shear layer a new grid called Grid II is being used in next section for evaluating the VπLES method.

(a) mean axial velocity

(b) r.m.s of axial velocity fluctuation
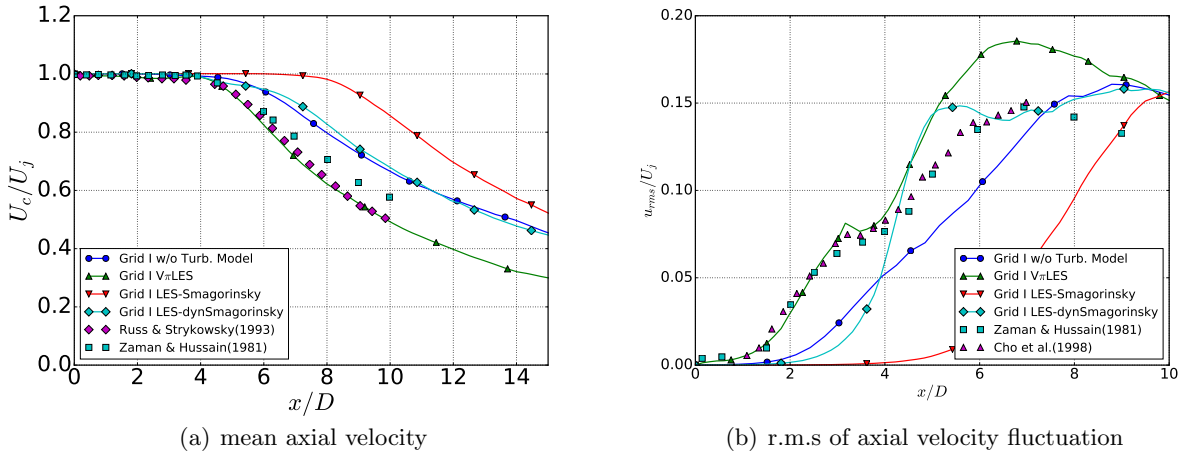
Figure 5.9: Comparison of performance of the new hybrid method and LES with two SGS models

5.2.2 Hybrid method - Grid I vs. Grid II

By increasing the mesh resolution in the shear layer the evolution of axial velocity fluctuation is remarkably improved (see Fig. (5.10.b)) while the result of LES with both standard and dynamic Smagorinsky mode still shows a strong deviation from experiment specifically in the region near the nozzle exit ($\frac{x}{D} < 4$) (see Fig. 5.11).
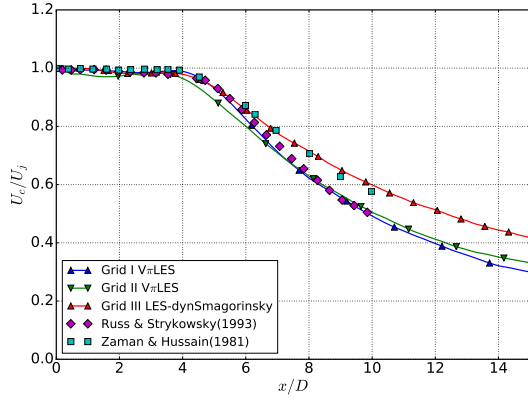
(a) mean axial velocity
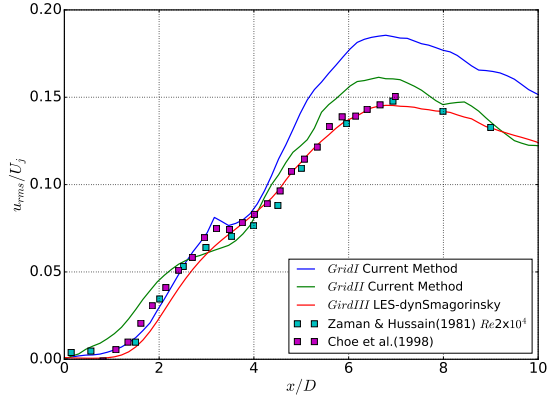
(b) r.m.s of axial velocity fluctuation

Figure 5.10: Comparison of VπLES result on Grid I and Grid II with experiment and high resolution grid III result
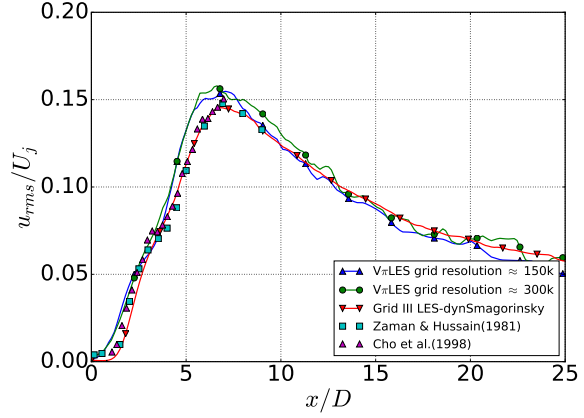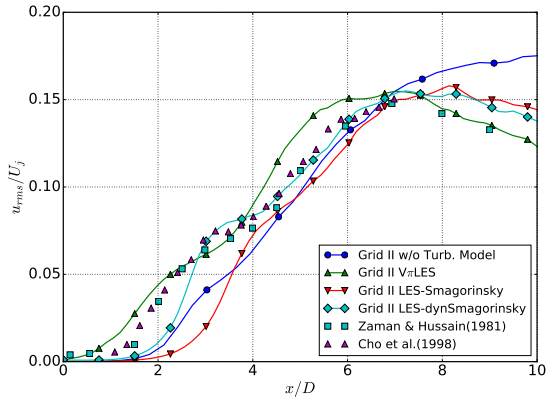
Figure 5.11: Comparison of performance of VπLES method and LES with two SGS models

5.2.3   Hybrid method - Influence of number of particle per cell N_{pt}, Grid II

Fig. (5.12) shows that by increasing the number of allowed particles per cell N_{pt} there is a slightly improvement in prediction of u_{rms} especially in the far field. This improvement can be a result of slightly increase in energy drain from large scale structure through the term $u^g \overline{u^v \times \omega^g}$ (see section (3.3)).
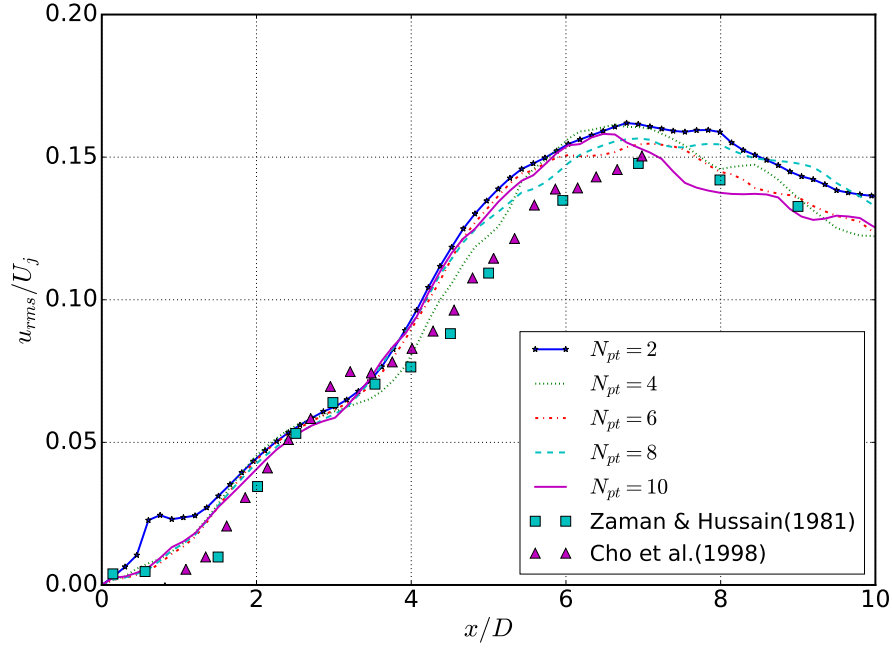
Figure 5.12: Influence of number of particle per cell N_{pt} on the evolution of u_{rms} along the jet centerline, Grid II, $Re = 10^4$

5.2.4 Hybrid method - Radial profile of mean axial velocity, Grid I and Grid II

Figs. (5.13) and (5.14) show the radial velocity profile of mean and r.m.s of axial velocity for two coarse grids with VπLES method and LES with two SGS models. The result of Grid III is considered as reference point for comparison. As can be seen in Figs. (5.13) and (5.14) although the discrepancy between target results and VπLES are still substantial, the qualitative agreement is pretty good. Specifically at the nozzle exit in the near field ($\frac{x}{D} < 4$) the discrepancy of two classical SGS models with reference result is not acceptable while VπLES simulation shows very good performances.
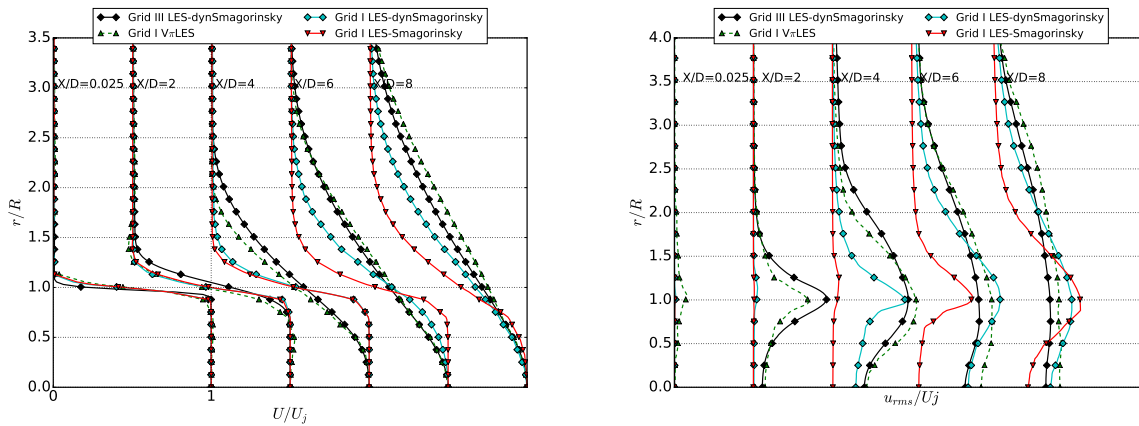
Figure 5.13: Radial profile of mean and r.m.s of velocity fluctuations at five locations along the jet centerline for the Grid I
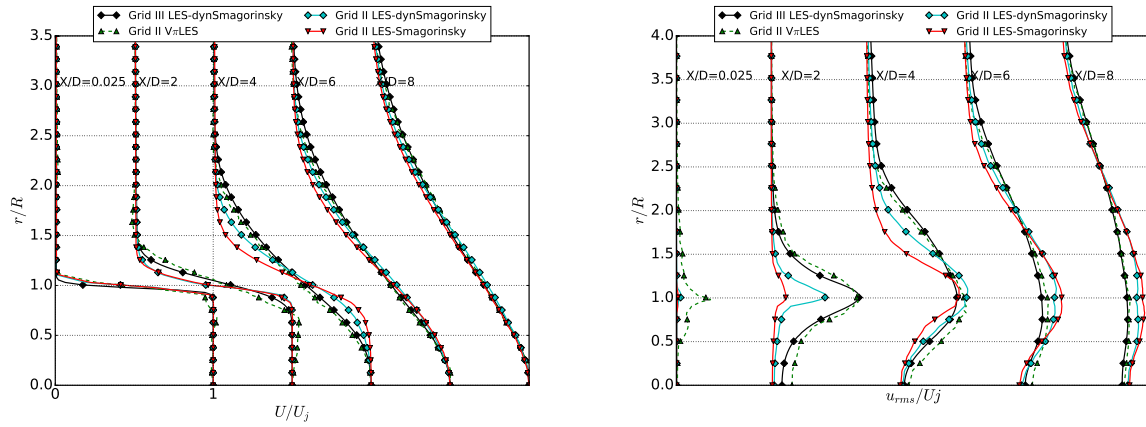
Figure 5.14: Radial profile of mean and r.m.s of velocity fluctuations at five locations along the jet centerline for the Grid II

5.2.5 Contour of instantaneous velocity field, Grid I

By looking at contour of instantaneous velocity field in Fig. (5.16) and (5.15) one can compare the length of potential core for different SGS models. While the Smagorinsky model shows stable and longer length of potential core, VπLES results in a shorter potential core and consequently more proper physical result. The result of high resolution grid (Grid III) was also presented in the last subfigure of Fig. (5.16).
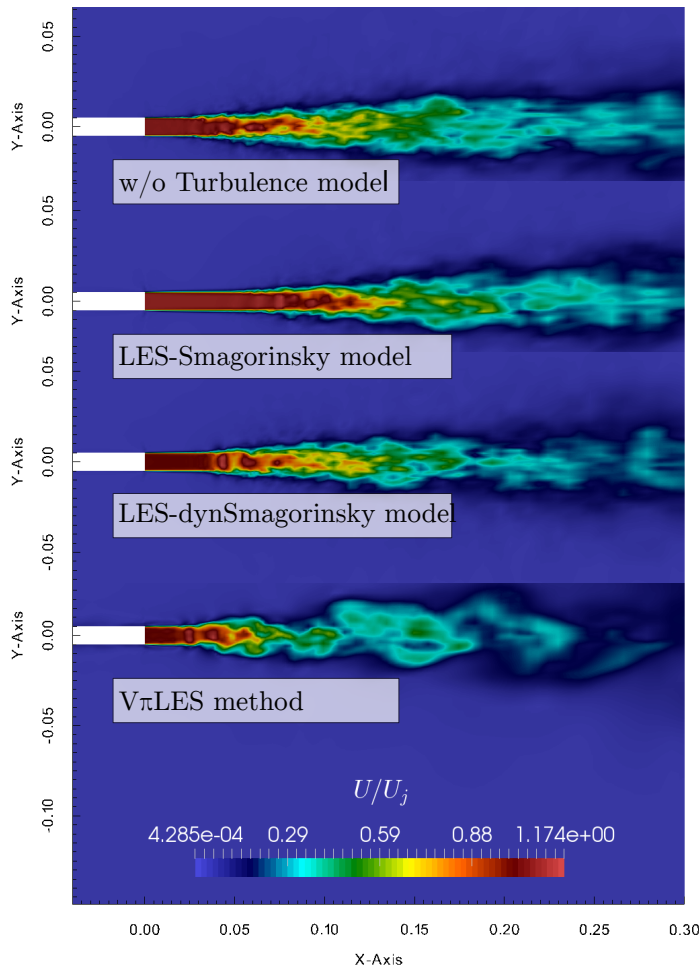
Figure 5.15: Grid I - Instantaneous velocity field - $Re = 10^4$

76
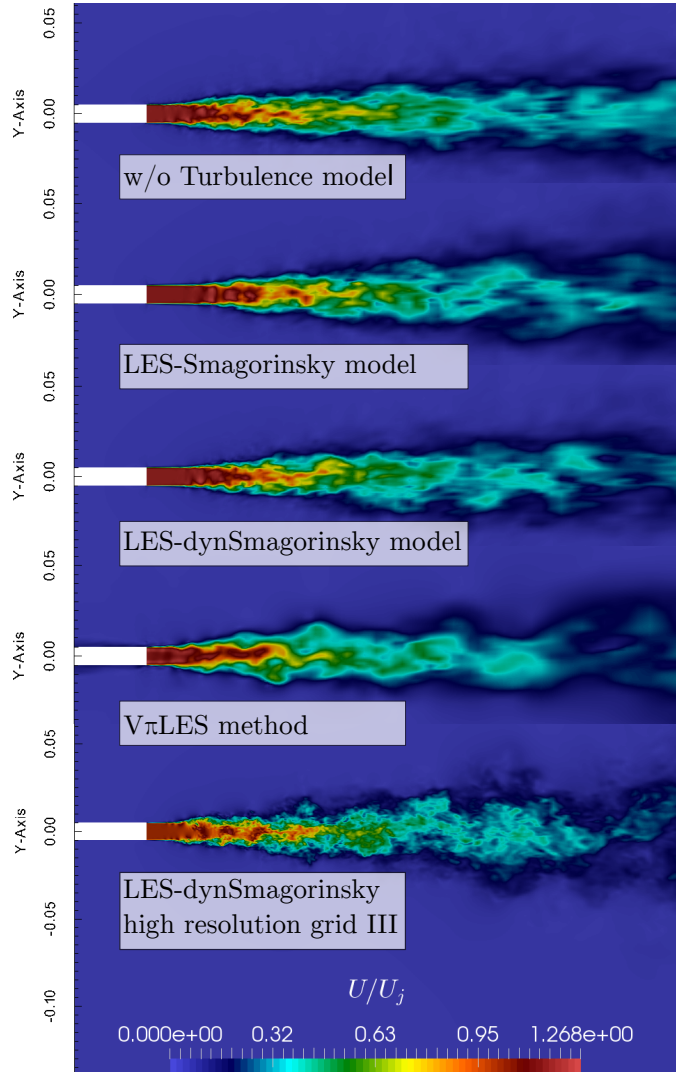
Figure 5.16: Grid II - Instantaneous velocity field - $Re = 10^4$. Last picture shows instantaneous velocity of high resolution grid (Grid III) using dynSmagorinsky model

5.2.6 Vortical structure shown by Q criterion, Grid II

To extract the region where rotation is assumed to dominate plane strain one can use a Q function. Obviously the transition to turbulence and jet breakdown is still delayed in pure grid-based simulations as can be revealed in the vortical structures displayed by Q criterion in Fig. (5.17). Analysis of results for the Grids I and II reveals similar trends. The simple Smagorinsky model is very diffusive and sufficiently delays the formation of the jet breakdown in comparison with the no-model especially at a very coarse resolution (Grid I). On the contrary, the dynamic Smagorinsky approach provokes earlier instability than the no-model and provides more satisfactory results at the distance $x/D > 6$. The turbulence intensification by vortex particles in VπLES is proved to be sufficient to trigger the turbulence already at small x/D.

LES-Smagorinsky model

LES-dynSmagorinsky model

VπLES method
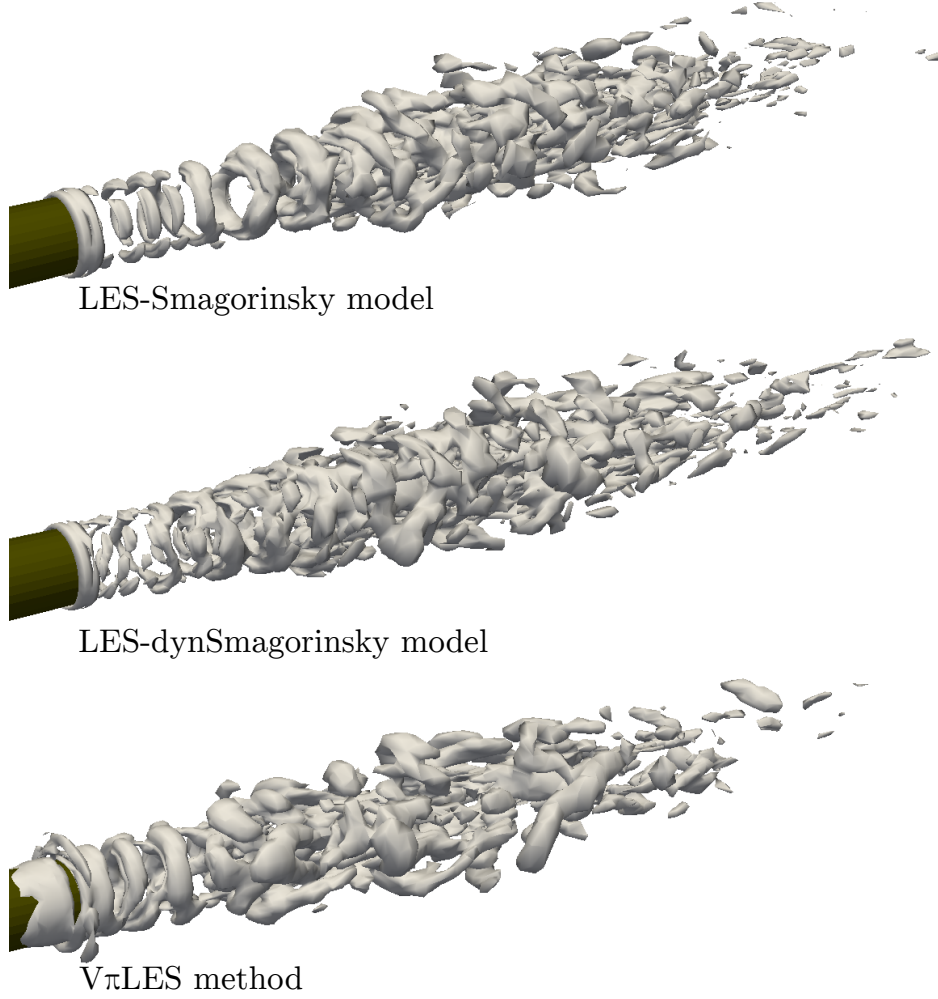
Figure 5.17: Grid II - Instantaneous vortical structure - Q criterion - $Re = 10^4$.

5.2.7 Model reduction

As shown in section (4.9) the Eqs. (3.30) and (3.13) can sufficiently be reduced by neglecting inner interaction between vortex particles without a significant loss of the simulation accuracy. The reduced equations take the form of Eqs. (4.6) and (4.7). This model is further referred to as the passive vortices model. Within the next simplification step the influence of the grid based solution on the evolution of vortex particles strengths is neglected. In other words, the stretching and rotation of fine vorticity caused by grid velocities is neglected. The equations describing the vortex particle evolution take the simplest form:

$$\frac{d\mathbf{r_i}}{dt} = \mathbf{u}_i^g \tag{5.2}$$

$$\frac{\partial \boldsymbol{\omega}^v}{\partial t} + (\mathbf{u}^g \cdot \nabla)\boldsymbol{\omega}^v = \nu \Delta \boldsymbol{\omega}^v \tag{5.3}$$

Fig. (5.18) demonstrates results for the r.m.s. of the axial velocity obtained using the full model Eqs. (3.13) and (3.30), passive vortices model Eqs. (4.6) and (4.7) and the model without influence of the grid based flow on vortex particles strengths Eqs. (5.2) and (5.3). The difference between results is negligible pointing out that vortex particles serve just as triggers or intensifiers of turbu-

lence and their inner interaction does not contribute sufficiently to the flow evolution. Hence the name of the method is the LES intensified by the vortex particles or VπLES.
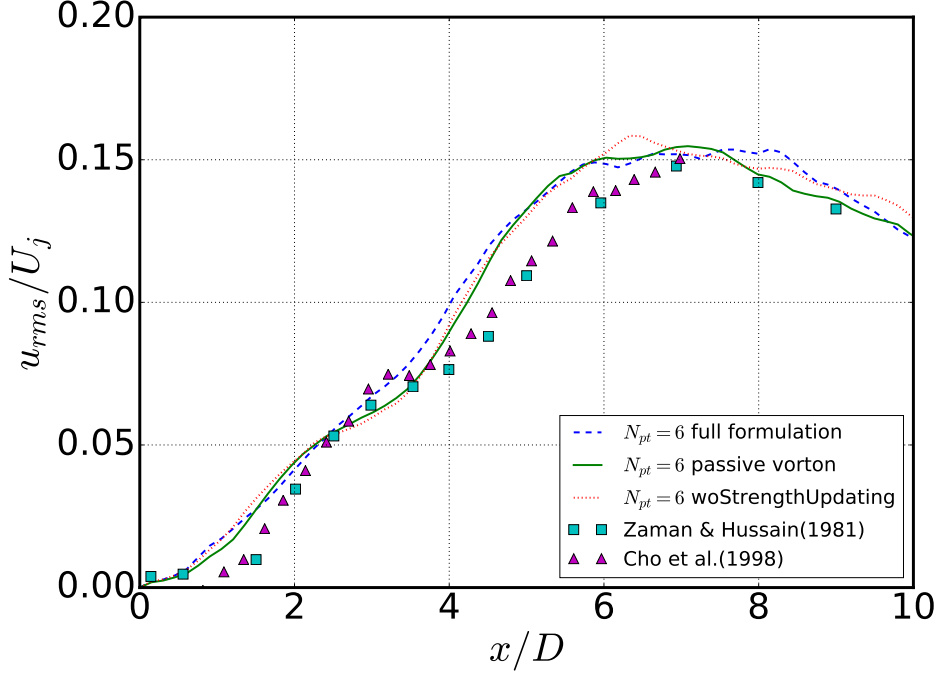
Figure 5.18: Influence of the interaction between vortex particles and grid on u_{rms}.

5.2.8 Properties of VπLES subgrid model represented by the term $\overline{\mathbf{u}^v \times \boldsymbol{\omega}^g}$

Since a deterministic prediction of a turbulent flow as mentioned in the definition of the turbulent motion by [107] is practically impossible, the task of every SGS model is to reproduce the subgrid motion only in the statistical sense. The following features of the subgrid motion should be captured by a proper subgrid model: non-equilibrium effects including laminar-turbulent zones, energy backscatter and anisotropy of fine scale motion.

5.2.8.1 Contribution of the term $\overline{u^v \times \omega^g}$ in kinetic energy transport equation

The term $\mathbf{u}^g \overline{\mathbf{u}^v \times \boldsymbol{\omega}^g}$ describes the contribution of fine scales to the energy of the large structures motion in the grid solution. This phenomenon is similar to the energy backward cascade process or the energy backscatter known from LES. If $\mathbf{u}^g \overline{\mathbf{u}^v \times \boldsymbol{\omega}^g}$ is positive the energy of fine scales is transferred from fine scale motion to the large one. We use the same terminology in context of VπLES . However, it should be noted, that the backscatter phenomenon is a inherent part of modeling and strongly depends on the way of scale decomposition including, for instance, filtering problems. In the other words, different definitions of the scale decomposition in the model and/or in its numerical implementation result in different relations for backward and forward energy transfers for the same flow. Since VπLES uses an own concept of decomposition, a certain difference of qualitative and quantitative characters between LES and VπLES energy transfers is to be expected. Fig. (5.19) shows the time averaged distribution of $\mathbf{u}^g \overline{\mathbf{u}^v \times \boldsymbol{\omega}^g}$ at the short distance $x/D = 2$ from the nozzle. The energy transfer from small scales to large ones occurs in the mixing layer at the jet border. It has maximum at the beginning of the jet and decreases downstream. The ring-like energy backscatter area encircles the ring-like area of a strong forward energy flux from large to small scales which is two orders larger than the backward one. In [108] an extended analysis of the mechanism of energy exchanges between different scales and a comparison with a LES backscatter with plane jet was given.
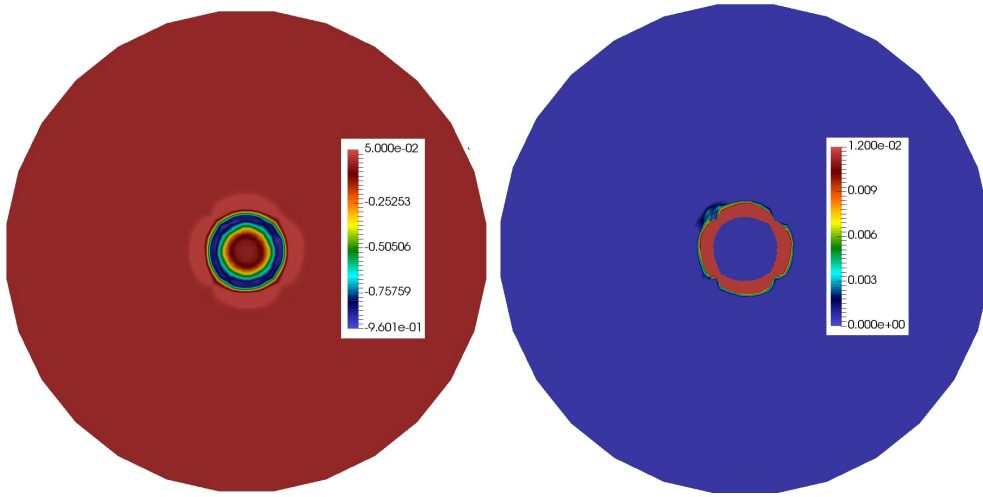
Figure 5.19: Time averaged energy contribution $\mathbf{u}^g\overline{\mathbf{u}^v \times \boldsymbol{\omega}^g}$ at $x/D = 2$. Left: full range, Right: energy backscatter $\mathbf{u}^g\overline{\mathbf{u}^v \times \boldsymbol{\omega}^g} > 0$. V$\pi$LES simulations on the Grid II.

5.2.8.2 Consistency of the model for laminar flows

Fig. (5.20) shows the velocity decay on the centerline of jet at a very small Re number $Re = 100$. From comparison of results for the simulation without model and VπLES simulations it follows that the influence of the coupling term $\overline{\mathbf{u}^v \times \boldsymbol{\omega}^g}$ is negligible when the flow is laminar. Generally, such a result could be due to the two following reasons. First, it could be due to reduction of vortex particles population and weakening their strengths in the smooth laminar velocity fields. Second, it could be just a mistake of the numerical setup when the same setup is applied for laminar and turbulent flows. Indeed, for $Re = 100$ the mean value of $\lambda_{ci,mean}$ used for the detection of vortex particles is almost two orders smaller than for $Re = 10^4$. Erroneous application of the same threshold $\lambda_{ci,min}$ for both cases would result in a drastic reduction of the number of generated vortex particles and weakening their influence. To clear this question, two simulations with $\lambda_{ci,min} = 0.002$ which is about 5% of the mean λ_{ci} and $\lambda_{ci,min} = 0.1 \approx 3\lambda_{ci,mean}$ have been performed. Although around 5×10^4 particles are generated each time instant in the first case and only 3×10^3 ones in the second case there is no visible difference between two simulations. This is a clear indication that the particles strengths and the term $\overline{\mathbf{u}^v \times \boldsymbol{\omega}^g}$ are negligible for the $Re = 100$ case and the term switches off in laminar flows. This happens because the difference between filtered and non filtered velocities in Eq. (3.16) becomes smaller for smooth velocity fields in laminar flows.
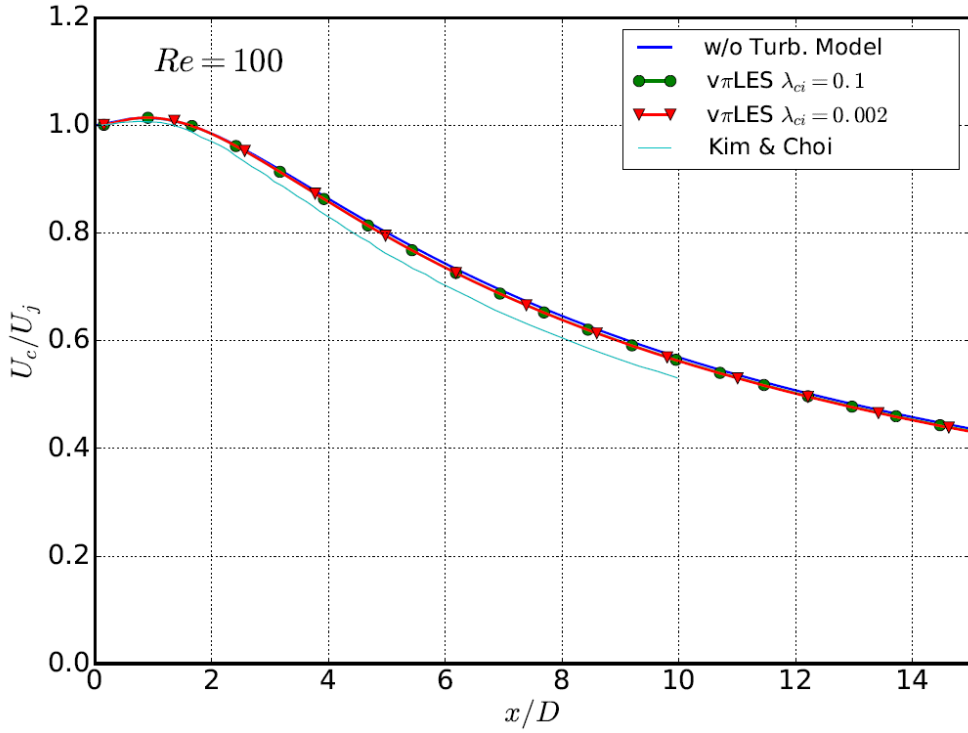
Figure 5.20: Decay of axial velocity along the jet centerline at $Re = 100$. Computations with the Grid II.

5.2.8.3 Anisotropy of small scale motions induced by vortex particles

The total flow shows a well pronounced anisotropy with the dominance of the axial fluctuations on the jet centerline (see Fig. (5.21)). Reynolds stress components R_{ij}^v of the velocity field $\mathbf{u}^v$ show also a clear strong anisotropy which is space-dependent. Relations between the Reynolds stress components induced by the vortex particles and their orientation, strengths and spatial distribution is still remaining unclear and will be studied in future works.
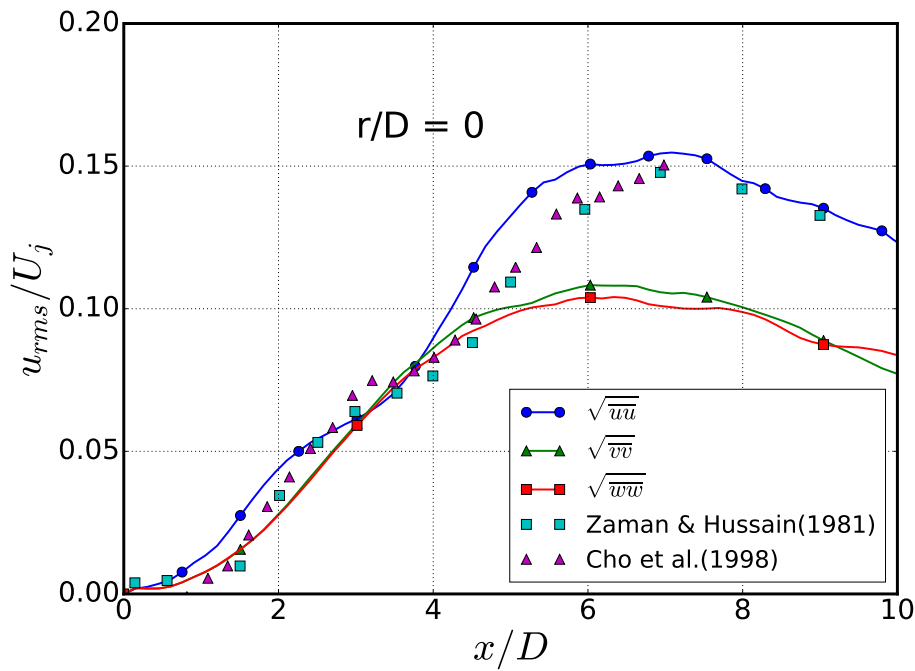
Figure 5.21: Distribution of the diagonal Reynolds stress components for the total velocity ($\mathbf{u}^v + \mathbf{u}^g$) along the jet axis

5.3 Choice of free parameter

One of the weaknesses of many particle based Lagrangian methods is the presence of free parameters which are often tuned to match desirable results if the latter are known before simulations. Strictly speaking, scheme parameters are an inherent part of every numerical technique including grid based ones. Their presence does not cause objections if there exists certain rules for their choice. $V\pi LES$ has two parameters which choice could cause difficulties. The first parameter is the number of particles per cell N_{pt}. Theoretically, N_{pt} should be as large as possible. Practically, it is restricted to perform the solution in a reasonable computational time. Fortunately, Figs. (4.21) and (5.12) show that increase of N_{pt} does not change the results significantly. More precisely, in Fig. (5.12) there is a slight improvement in prediction of u_{rms} especially in the far field. This improvement is a result of a small increase in energy drain from large scale structures through the term $\overline{\mathbf{u}^v \times \boldsymbol{\omega}^g}$. The same conclusions were drawn for the decaying homogeneous isotropic turbulence (HIT) in cubical box (see section 4.10). The value $N_{pt} = 4$ seems to be sufficient to attain a proper accuracy. The second important parameter is the threshold $\lambda_{ci,min}$ used for the vortex particle identification. The recommendation is to set $\lambda_{ci,min}$ being equal to $\approx 5\%$ of the mean λ_{ci}, i.e. $\lambda_{ci,min} = 0.05\lambda_{ci,mean}$. Fig. (5.22) illustrates the number of newly generated vortex particles depending on $\lambda_{ci,min}$ calculated at a certain time instant when the jet flow is well developed. The λ_{ci} criterion attains the maximum value $\lambda_{ci,max} = 128.61$ with $\lambda_{ci,mean}$ being equal to 1.76. The picture has a clear physical interpretation. If $\lambda_{ci,min} = 0$ the number of vortex particles with $\lambda_{ci} \geq 0$ is equal to the total number of cells $N = 1.5 \times 10^5$. They form a single cluster which is eliminated and the number of injected particles is zero. The function λ_{ci} is a rapidly growing function at the places with vorticity.

Therefore, a small change of $\lambda_{ci,min}$ results in an jump-like reduction of cells with $\lambda_{ci} > \lambda_{ci,min}$ from $N = 1.5 \times 10^5$ to $N = 5.8 \times 10^4$ and in increase of injected particles from zero to $N_p = 2.2 \times 10^4$. The increase of $\lambda_{ci,min}$ leads to a further decrease of N and N_p. $N > N_{pt}$ because a part of vortex cells with $\lambda_{ci} > \lambda_{ci,min}$ are recognized as clusters with a size of a few cell sizes which are eliminated according to the algorithm described in section (3.6). However, there is a clear tendency $N_p \to N$ when $\lambda_{ci,min}$ increases because peaks of λ_{ci} distribution correspond to spots of concentrated vorticity which have small extent in space and, therefore, all of them are converted to particles. At $\lambda_{ci,min} \approx 0.06...0.07\lambda_{ci,mean} \approx 0.106...0.123$, N_{pt} is stabilized around the value of 1.1×10^4 and further does not change significantly. The value $\lambda_{ci,min} = 0.1$ was used in all $V\pi LES$ simulations for $Re = 10^4$. As follows from Fig. (5.22) increase of $\lambda_{ci,min}$ has a minor effect on N_{pt}. Smaller values $\lambda_{ci,min} < 10$ would not be advisable because the number of particles will sufficiently be increased by involving a big portion of weak vortices corresponding to small λ_{ci}. For the time step $\Delta t = 10^{-4}$ around 10^8 particles are generated within one second of real time. Most of them are eliminated by the sorting algorithm (see section 3.6) when the number of particles in cell exceeds N_{pt} so that only 1.5×10^4 N_{pt} particles are kept each time on the Grid II.
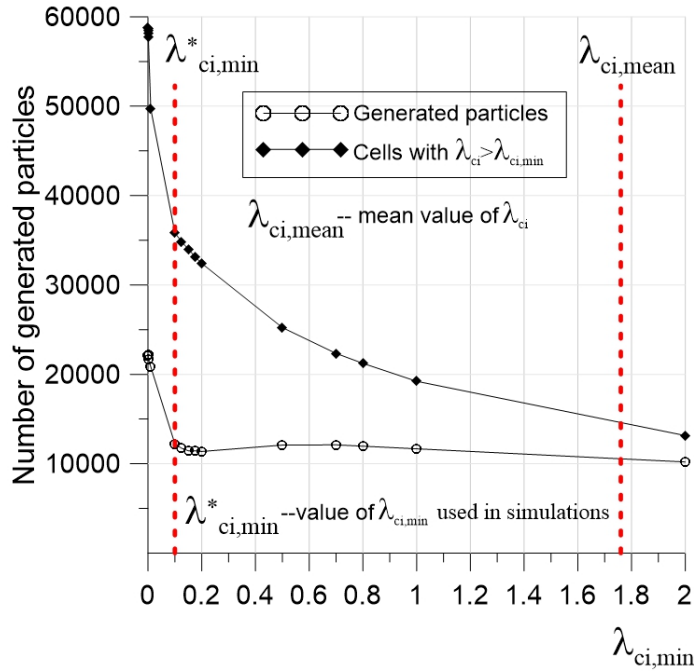
Figure 5.22: Influence of $\lambda_{ci,min}$ on the number of generated vortex particles.

5.4 Summary

After a successful validation for the case of decaying homogeneous isotropic turbulence presented in chapter (4) and published in [91] the VπLES method is applied to the turbulent circular free jet at $Re = 10^4$. Numerical results are compared with experiments of [7], [8] and [10] for mean velocities and fluctuations. It was shown that the VπLES simulation with 1.5×10^5 mesh cells can attain similar accuracy as LES with the Dynamic Smagorinsky model on the grid with 6.04×10^6 cells. For these grids, the computational time using one core is 2.69 sec for VπLES and 65 sec for LES, i.e. the speed up factor is around 24. For the same grid resolution the performance of VπLES is superior compared to a pure grid-based LES.

VπLES method is considered as a LES with direct resolution of the subgrid motion represented by vortex particles. The model of the subgrid motion reproduces the energy transfer from fine vortices represented by particles to large scale ones modeled on the grid. In terms of LES it can be interpreted as the energy back scattering which occurs in the mixing layer at the jet border. The intensification of the turbulent kinetic energy due to back scattering is proved to be very important to properly reproduce the jet breakdown and transition to turbulence close to the nozzle without any artificial turbulence forcing at the nozzle. In the laminar flows the vortex particle influence is automatically switched off because of reduction of vortex particles population and weakening their strengths in the smooth laminar velocity fields. The Reynolds stress of the velocity field induced by particles possesses the pronounced anisotropy which is space dependent. The physics behind this anisotropy is to be explained in the future works by more thorough study of vortex particles distributions and their orientations.

Choice of the scheme (free) parameters is studied and discussed. Like for the case of decay of isotropic turbulence in a box presented in chapter (4) the model for the jet case can be sufficiently reduced by neglecting the inner interaction between particles. In section (5.2.7) it was shown that the stretching and rotation of fine vortices caused by grid can also be neglected. The vortex particles serve just as a triggers of turbulence and their inner interaction does not contribute sufficiently to the flow evolution. This results in a very efficient and fast computational procedure. The result and conclusion achieved in this chapter was published in [108].

6 Wall-bounded flow

In the previous chapters the potential of VπLES method has been evaluated for the simulation of free shear flows. In unbounded flow the largest majority of turbulent kinetic energy has been carried by the large scale eddies, this concept is reverse near the wall, where small scale motions contain the most energetically productive eddies. Both these descriptions are valid in wall-bounded flow and both mechanisms contribute significantly to the overall turbulent flow field [109]. Most turbulent flows are bounded (at least in part) by one or more solid surfaces, flow through pipes and ducts, around ships' hull and atmospheric boundary layers are some examples of wall-bounded flow. One of the major reason for high cost of modeling of wall-bounded flow is the requirements of the resolution of small-scale motions in the boundary layer. The streak process is the main source for the majority of turbulence production at low to medium Reynolds numbers for wall-bounded flows. In order to achieve accurate result this structured flow must be resolved properly in LES [6].

The purpose of this chapter is to evaluate the VπLES method capability of treating near-wall flow properly. The test case in the current chapter is a fully developed channel flow in which the mean velocity vector is (or nearly is) parallel to the wall. Fully developed channel flow is considered as a flow through a rectangular duct of height 2δ, where δ is a half channel height. The channel is long ($L/\delta \gg 1$) and has a large aspect ratio ($b/\delta \gg 1$). The mean flow is in axial direction and varies in the cross stream direction. The dimension of the channel in spanwise direction must be considered large enough compared to δ so that the flow is statistically independent of z [13]. The schematic view of channel computational domain is shown in Fig. (6.1).

6.1 High resolution pure grid-based simulation using LES

6.1.1 Numerical set up

Fully developed channel flow is homogeneous in streamwise and spanwise directions. The size of computational domain was chosen as $6(m) \times 2(m) \times 3(m)$ in the streamwise, wall normal and spanwise directions respectively. In the first step the computation was carried out with a high resolutions grid with 4.6 Mio grid cells named C3. Case C3 has resolutions in streamwise and spanwise directions similar to DNS data of [110] and much larger first cell distance to the wall (see table 3). The purpose of high resolution grid study is to investigate the turbulence properties in the channel flow with LES approach using dynamic Smagorinsky model and to find the proper numerical set up through comparing the results with DNS data of [110]. The result of high resolution grid is later used as a reference to validate the performance of VπLES on coarse grid. All simulations are performed for Reynolds number of 395 which is based on the friction velocity u_τ and channel half-height δ, ($Re_\tau = \frac{u_\tau \delta}{\nu}$).

The mesh parameters are presented in table 3. Considering the size of computational domain, the grid spacing in streamwise and spanwise directions for the case C3 are $\Delta x^+ = 11.32$ and $\Delta z^+ = 6.28$ in wall unit. The distance of the first grid cell center from the wall is $y^+ = 0.41$ in wall unit and the maximum spacing at the center of the channel is $\Delta y^+ = 18$. Periodic boundaries have been applied in streamwise and spanwise directions. The boundary must be located far apart enough to include the largest eddy structures in the flow. Later discussion of two-point correlation confirms the proper choice of domain size (see section (6.1.4)). A large number of turbulence statistics is computed and compared with the existing DNS data of [110].
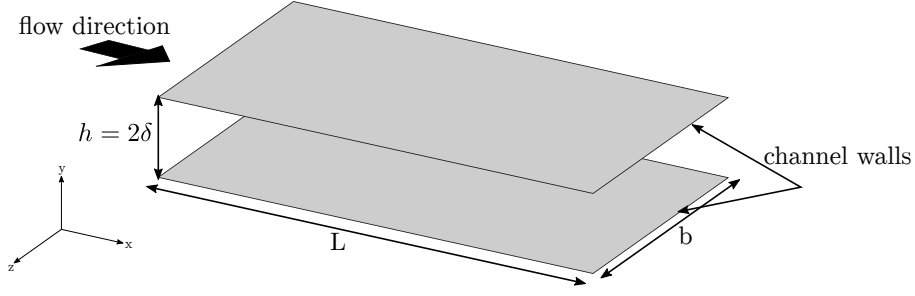
Figure 6.1: Schematic view of channel flow computational domain.

Table 3: Grid parameters

Case No	Mesh cells	y^+ (Normalized by u_τ from each simulation)	Δx^+	Δz^+
C1	30 k	5.4	63	47
C2	72 k	1.7	37	21
C3	4.6 mio	0.41	11.32	6.28
DNS	9.5 mio	0.05	10.0	6.5

6.1.2 Mean axial velocity and turbulent kinetic energy profiles

Fig. (6.2) shows the resolved streamwise velocity profile in wall unit coordinate as well as global coordinate scaled by friction velocity u_τ and bulk velocity $\mathbf{U}_b$ respectively. In LES simulation with grid C2 four points were located in the viscous sublayer ($y^+ < 5$). The viscous sublayer is resolved well enough and accurately represents the DNS data for the whole sublayer. In log-law region ($y^+ > 30$) there is a slight overprediction while in buffer region ($5 < y < 30$) the agreement with DNS data is pretty good (see Fig. (6.2.a)). All simulations normalized by the same value of u_τ from DNS.

(a) Mean velocity profile, wall coordinate

(b) Mean velocity profile, global coordinate
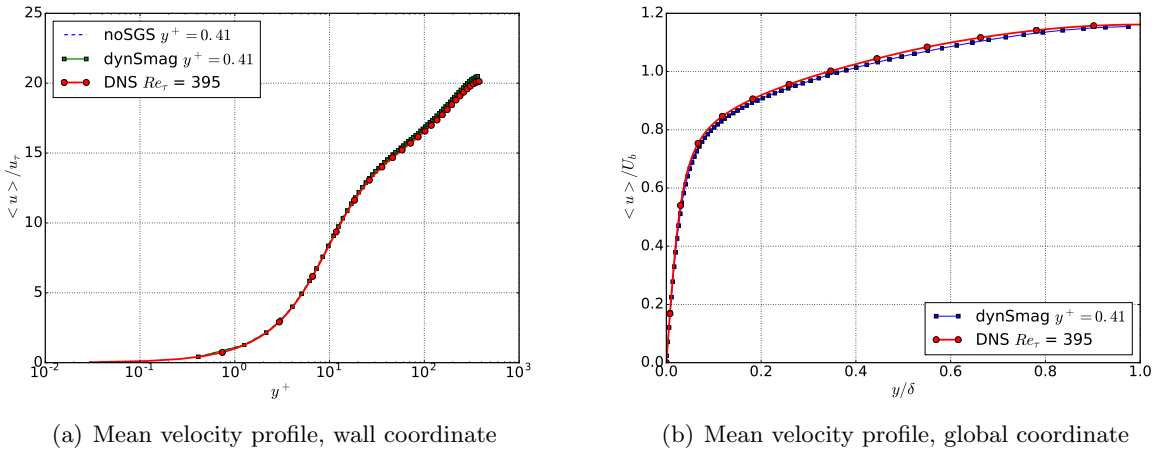
Figure 6.2: Mean velocity profiles in fully developed turbulent channel flow, Grid C3.

6.1.3 Kinetic energy and Reynolds stresses

Figs. (6.3) and (6.4) show the kinetic energy, Reynolds stress components and the negative of the correlation of velocity fluctuation components u and v ($- < uv >$). In Fig. (6.3.a) the location of peak for the predicted total kinetic energy is in a good agreement with DNS data while the value is slightly smaller. The underprediction of the kinetic energy is the result of coarse grid resolution

in buffer layer in comparison with DNS. Components of Reynolds stress tensor are the primary quantities defining the turbulent kinetic energy. $u_i'^2$ is the variance of the velocity components but it is more convenient to consider the root mean square u_i^{rms} of u_i components. Fig. (6.3.b) shows that the value and the location of the peak of u_i^{rms} is accurately match the DNS data. In the outer region u_i^{rms} profiles depend linearly on y/δ until $y/\delta \approx 0.85$. The off-diagonal component of Reynolds stress tensor (Reynolds shear stress) presented in Fig. (6.4.a) agrees well with DNS data. For $y/\delta > 0.2$ the profile is linear similarly to DNS data. It is possible to look at turbulent shear stress from another quantity by scaling it in a different way. The stress $- < uv >$ is the negative of covariance of u and v and normalizing with $u^{rms}v^{rms}$ gives the negative correlation of u and v [111]. Fig. (6.4.b) shows the comparison of the correlation coefficient of LES simulation and DNS data in grid C3. In the profile of negative correlation there is a local peak near the wall and there is also a local minimum right after that. High resolution grid C3 properly resolved these two peaks. In [110] the presence of the peak is explained by the presence of certain organized motion in that region.

(a) Kinetic energy normalized by friction velocity

(b) Reynolds stresses normalized by friction velocity
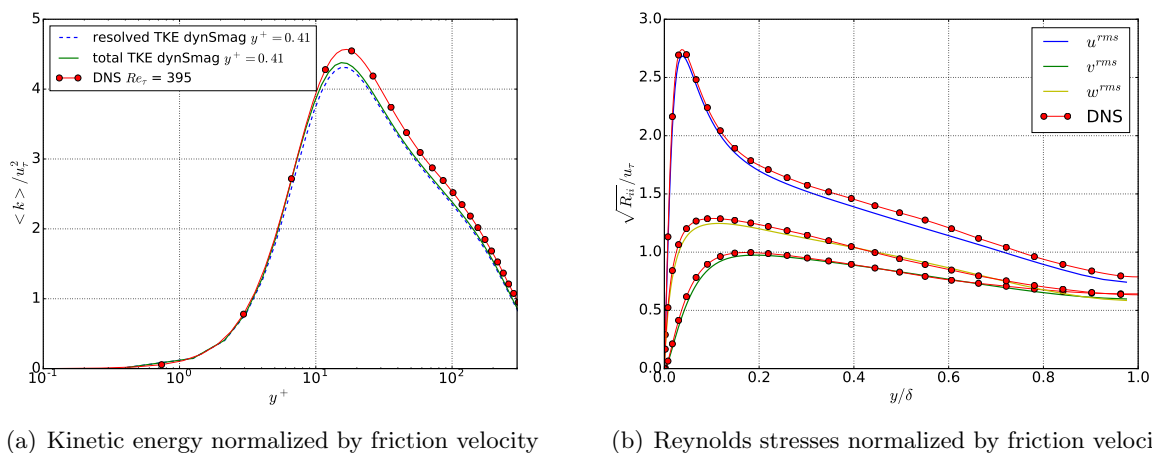
Figure 6.3: kinetic energy and Reynolds stress components, grid C3.

(a) Reynolds shear stress normalized by friction velocity

(b) Negative of the correlation coefficient of u and v
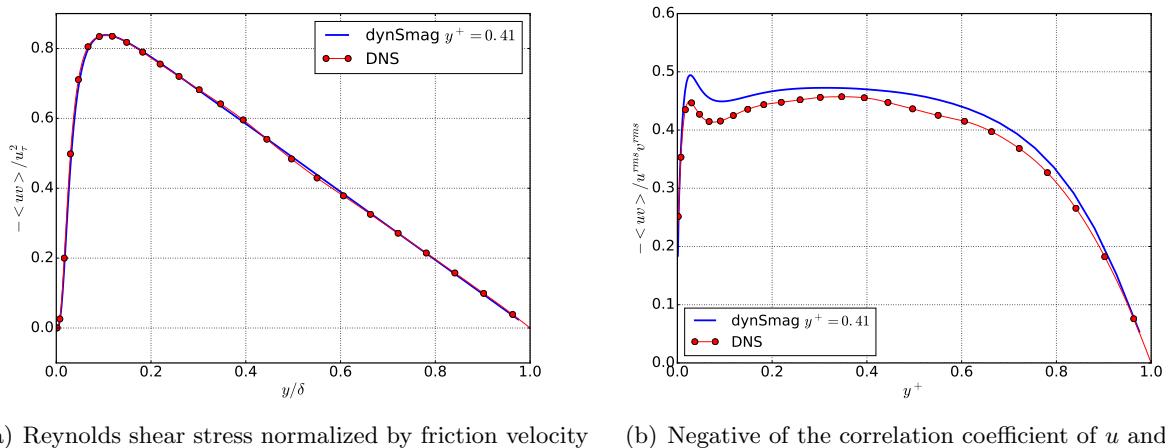
Figure 6.4: Normalized Reynolds shear stress and correlation coefficient, Grid C3.

6.1.4 Power spectral density and two point correlation

As can be seen in Fig. (6.5) the power spectral density of high frequency scales is several orders lower than the low frequency scales indicating the adequacy of grid resolution. There is no evidence of energy pile-up at high frequencies due to the resolving enough small scales for energy drain.

According to [110] it should be kept in mind that this drop-off of the energy spectra at high frequencies is not a sufficient evidence that the role of unresolved high frequencies scales on the computed result can be ignored and are negligible. Fig. (6.5) also shows that the most energetic structures exist in the region close to the wall. Close to the wall the spectrum of the vertical component of the velocity is less than that for other flow components of velocity due to the damping effect of the wall. The energy contained in the flow structures decreases by moving from $y^+ = 10$ to $y^+ = 392$. Far away from the wall the isotropy property of the flow is visible ($y^+ = 392$). The result for the two-point correlation is shown in Figs. (6.6) and (6.7). These results confirm that the size of the computational domain is properly selected. Approaching of the two-point correlation curve to zero values for large streamwise and spanwise separation shows that the computational domain is large enough so that the turbulence fluctuation becomes uncorrelated at a separation of half the domain size.

(a) $y^+ = 10$

(b) $y^+ = 40$

(c) $y^+ = 150$

(d) $y^+ = 392$
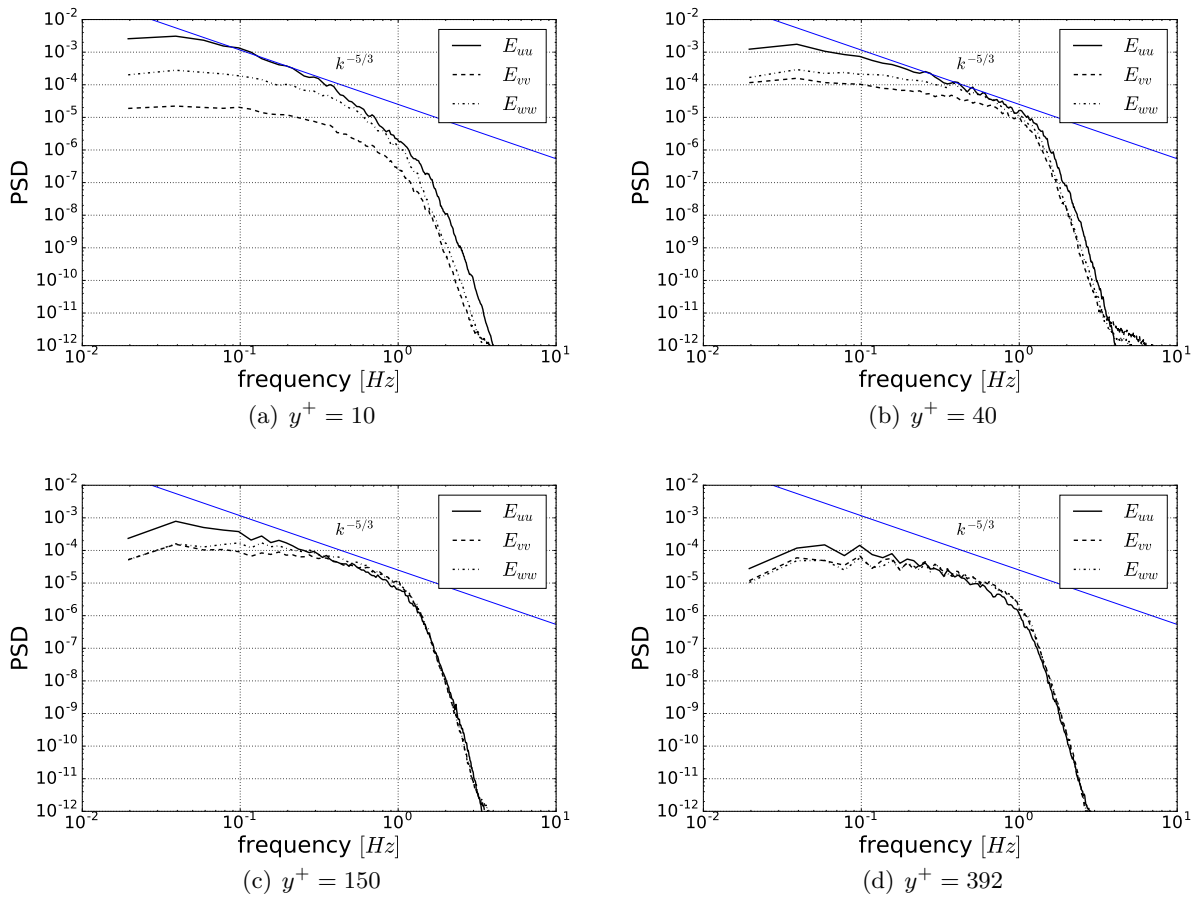
Figure 6.5: Power Spectral Density of the resolved fluctuation (Welch method), $y^+ = 0.41$, with dynamic Smagorinsky turbulence model, grid C3.
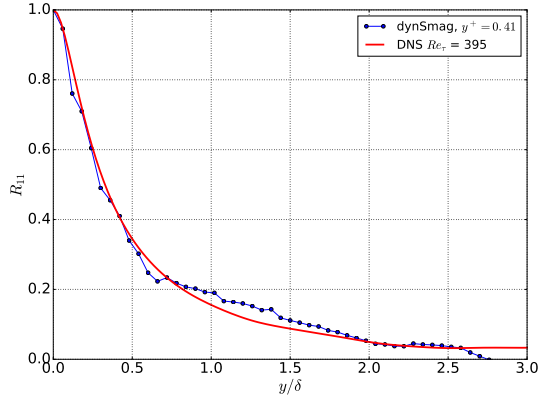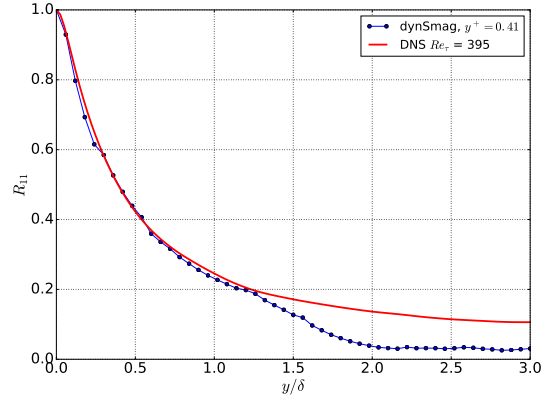
(a) Two-point correlatiosn, $y^+ = 10$ (b) Two-point correlatiosn, $y^+ = 150$

Figure 6.6: Streamwise separation: Two-point correlation falls to zero value for large separation, indicating that the computational domain is sufficiently large (uncorrelated at a separation of half period in homogeneous direction), grid C3.
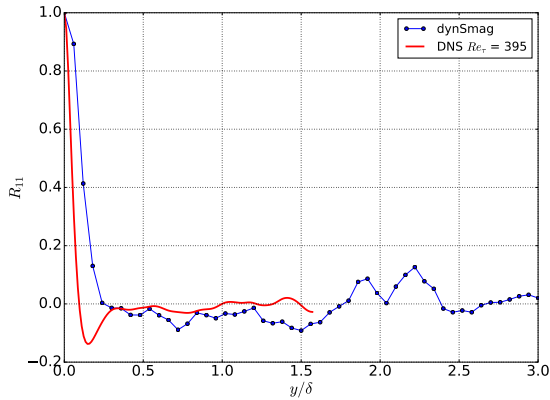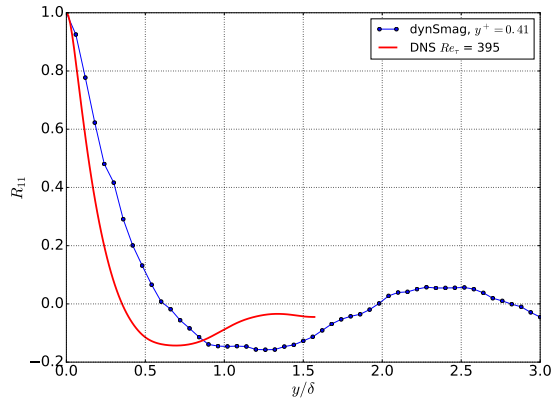
(a) Two-point correlatiosn, $y^+ = 10$ (b) Two-point correlatiosn, $y^+ = 150$

Figure 6.7: Spanwise separation: Two-point correlation falls to zero value for large separation, indicating that the computational domain is sufficiently large (uncorrelated at a separation of half period in homogeneous direction), grid C3.

6.1.5 Budget of turbulent kinetic energy

Analysis of the budget of the mean turbulent kinetic energy in Fig. (6.8) shows that the production, diffusion and dissipation terms in the budget become important close to the wall. Dissipation $\left(\nu \frac{\partial \overline{u}_i}{\partial x_j} \frac{\overline{u}_i}{\partial x_j} \right)$ is much greater than the production $\left(\overline{u'_i u'_j} \frac{\partial \overline{u}_i}{\partial x_j} \right)$ in the viscous sublayer region while they are approximately equal for $y+ > 50$ in the log-law region (turbulent equilibrium). It is also confirmed the homogeneous character of the flow at $y^+ > 50$. The viscous-diffusion rate term $\left(\frac{\partial}{\partial x_j} \left(\nu \frac{\partial \overline{k}_{res}}{\partial x_j} \right) \right)$ is small compared to the other terms except the region very close to the wall ($y^+ < 20$) and reaches the maximum at the wall. Dissipation rate has nonzero value at the wall and is almost equal to the viscous-diffusion rate. Fig. (6.8.b) shows the ratio of production and dissipation of turbulent kinetic energy. The result of LES simulation is higher than DNS data which can be due to the insufficient dissipation rate at the wall resulting from not-including the dynamical roles of all small scales in the buffer and log-law region.
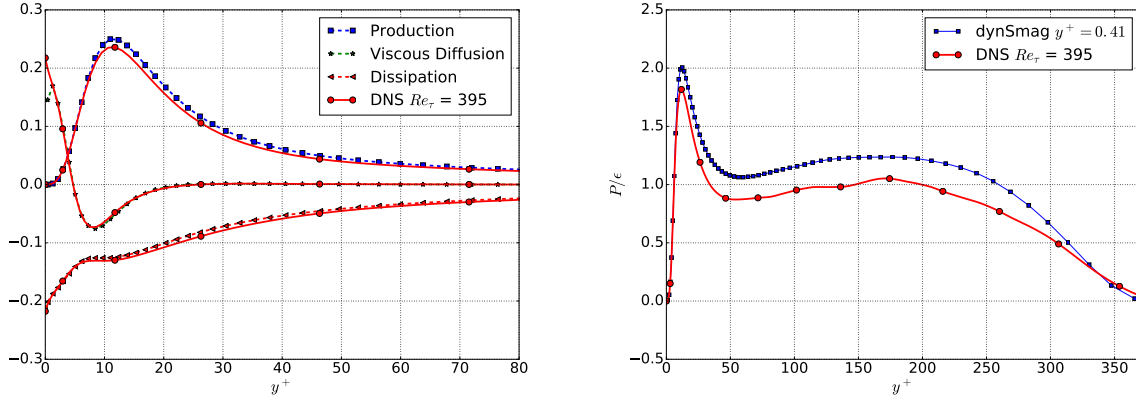
(a) Terms in the turbulent kinetic energy transport equation

(b) Ratio of production to dissipation of turbulent kinetic energy see Eg.

Figure 6.8: Budgets of turbulent kinetic energy

6.2   Under-resolved grid calculation

In order to investigate the potential of VπLES approach for the modeling of wall-bounded flow a comprehensive study of channel flow simulation has been performed. Two coarse grids have been constructed for the similar computational domain and called C1 and C2 (see table 3). The influence of different SGS models including VπLES have been investigated for these under-resolved grids through study the turbulence flow properties in the channel. Fist the results of C1 and C2 are presented in sections (6.2.1) and (6.2.2) then in sections (6.3) and (6.3.2) the results of VπLES method are also included in under-resolved grid simulation.

6.2.1   Mean axial velocity and turbulent kinetic energy profiles

Fig.(6.9) shows that grid C1 have a large deviation from DNS data for resolving mean velocity profile. This mesh is too coarse for LES resolution and even cells adjacent to the wall can not resolve the correct turbulence cycle. The difference between LES with dynamic Smagorinsky model and the cases without turbulence model is negligible. Profiles of kinetic energy in Fig. (6.9) and Reynolds stresses in Fig (6.10) show that the coarse meshes have a remarkably over-prediction of the near-wall normal components of Reynolds stress. This is a result of excessive resolved scale motion. Coarse meshes at the wall can not reproduce the fine near-wall turbulence features. This leads to the reproducing of a larger scale (as somewhat pseudo turbulence) corresponding to the larger grid size in the coarse mesh [112]. This behavior of under-resolved meshes is in agreement with the other published results [112]. Because of the increasing of the eddy size the eddy core moves further from the wall surface and the peak value of u_i^{rms} profile moves to the higher y^+ value as in Fig. (6.10).
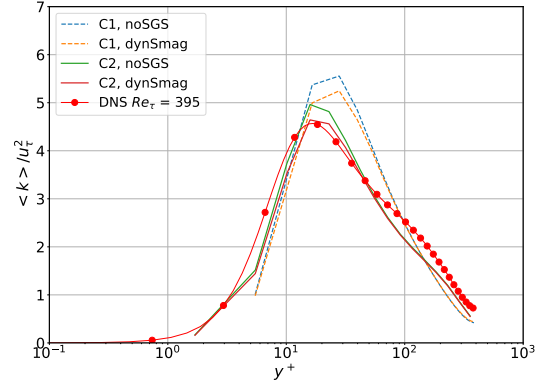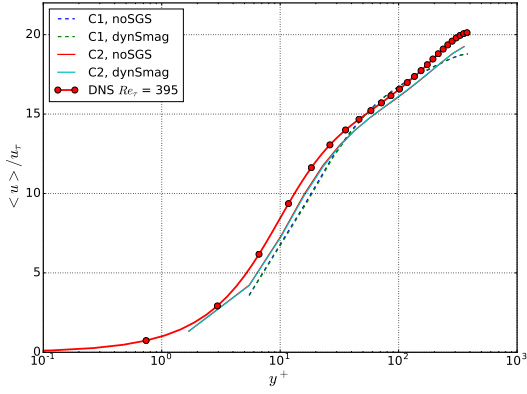
(a) Normalized mean velocity profiled in wall coordinate

(b) Kinetic energy normalized by friction velocity

Figure 6.9: Mean velocity and kinetic energy profiles in under-resolved grids C1 and C2.
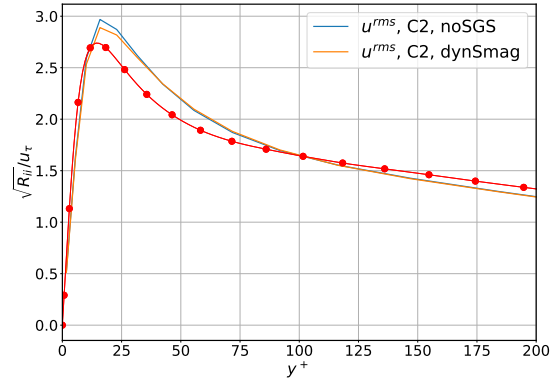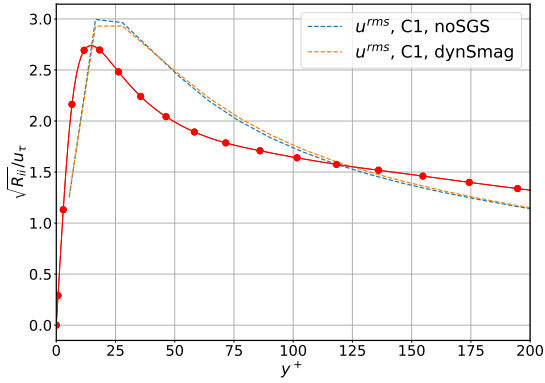
(a) Reynolds stresses normalized by friction velocity, grid C1.

(b) Reynolds stresses normalized by friction velocity, grid C2.

Figure 6.10: Reynolds stress components in under-resolved grids C1 and C2.

6.2.2 Power spectral density of resolved fluctuations with under-resolved grid

Fig. (6.11) and (6.11) show the energy spectra of the resolved fluctuations in coarse grid simulations C1 and C2 with dynamic Smagorinsky SGS model. In both grids the majority of turbulent energy is contained in the lower frequency or larger eddies compared with the fine mesh. There is an overdissipation of energy contained in the large scales because of a low resolution SGS model in C1 and C2. The results of power spectra of two under-resolved grids are very similar.

(a) $y^+ = 10$

(b) $y^+ = 40$

(c) $y^+ = 150$

(d) $y^+ = 392$
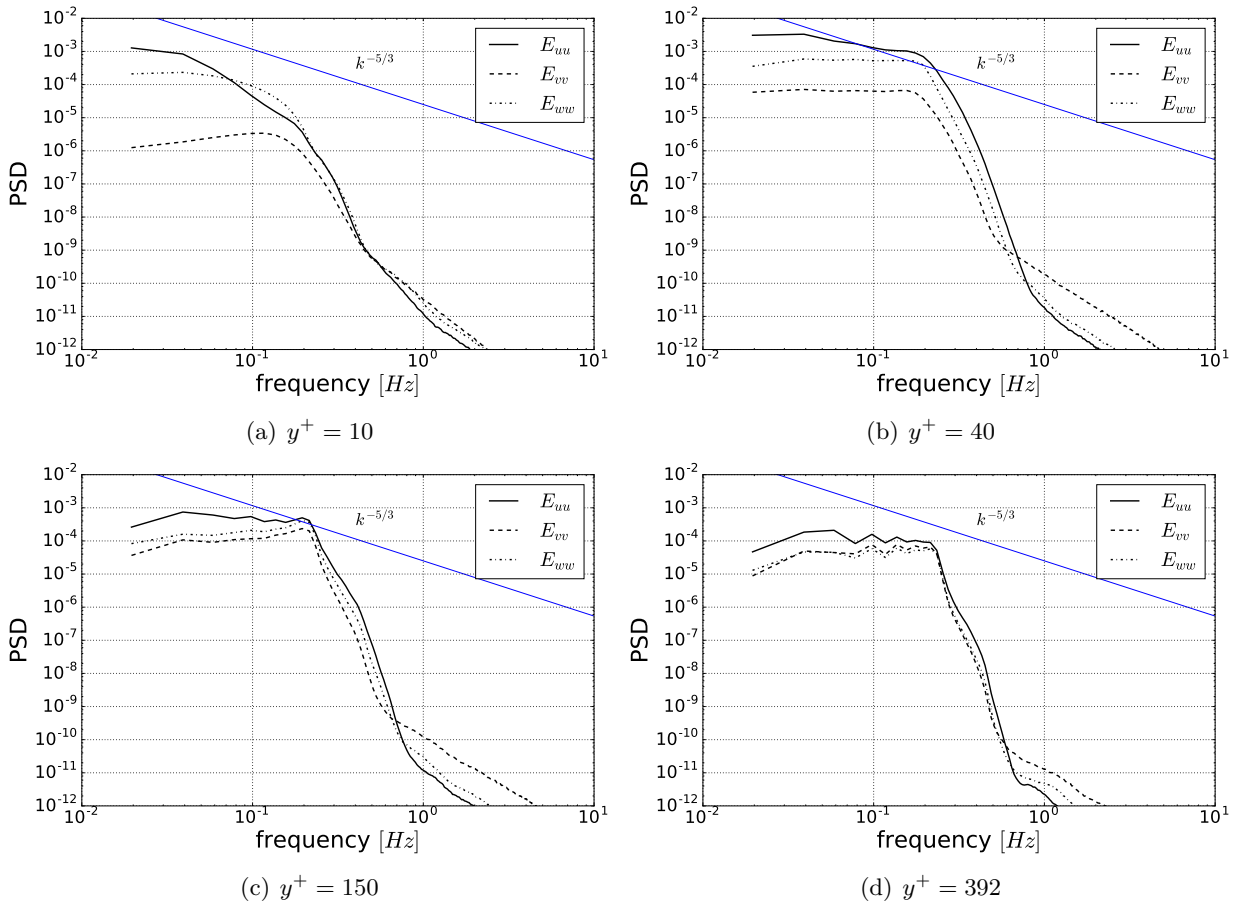
Figure 6.11: Power Spectral Density of the resolved fluctuation (Welch method), under-resolved grid C1 with LES dynamic Smagorinsky model.

(a) $y^+ = 10$ (b) $y^+ = 40$

(c) $y^+ = 150$ (d) $y^+ = 392$
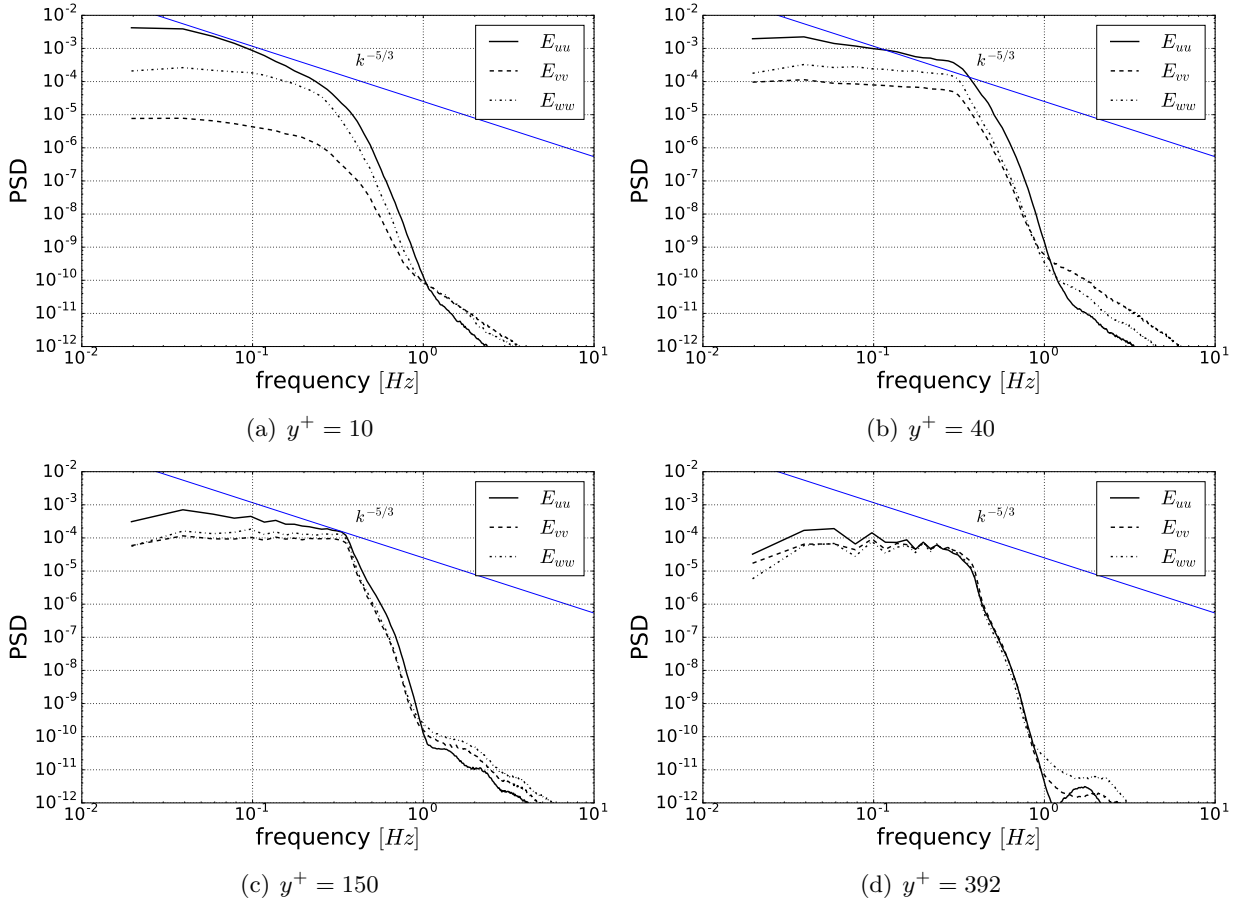
Figure 6.12: Power Spectral Density of the resolved fluctuation (Welch method), under-resolved grid C2 with LES dynamic Smagorinsky model.

6.3 VπLES with under-resolved grid calculation

6.3.1 Mean axial velocity and turbulent kinetic energy profiles

As presented in chapters (4) and (5) VπLES method could improve the results of under-resolved grid in case of decay of turbulence in box and free turbulent jet. In the same way grid C1 is chosen for further investigation using VπLES method. The aim of this study is to see if VπLES has a positive influence on the result of coarse grid C1 through resolving the small scales with Lagrangian vortex method. Fig (6.13) shows the mean velocity profiles in the case of dynamic Smagorinsky, VπLES and without turbulence model. The result of VπLES is similar to the case of dynamic Smagorinsky and without turbulence model and no improvement is achieved. In the other word the influence of the coupling term $\overline{\mathbf{u}^v \times \boldsymbol{\omega}^g}$ is very weak in the mean velocity profile. In Fig. (6.14) VπLES predicts larger value for kinetic energy and Reynolds stresses. The location of the peak is shifted to the higher value of y^+ due to the increasing of eddy size in coarse grid C1. The higher value in kinetic energy in VπLES method compared with dynamic Smagorinsky results from preserving the small scale vortex particle entities with vortex method. A remarkable amount of energy at high frequency scales shown in Fig. (6.15) also supports this fact.
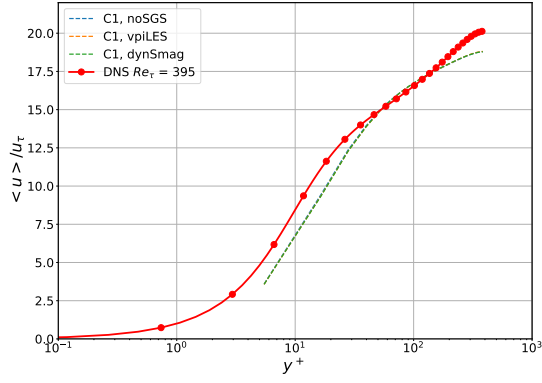
(a) Mean velocity profile, wall coordinate
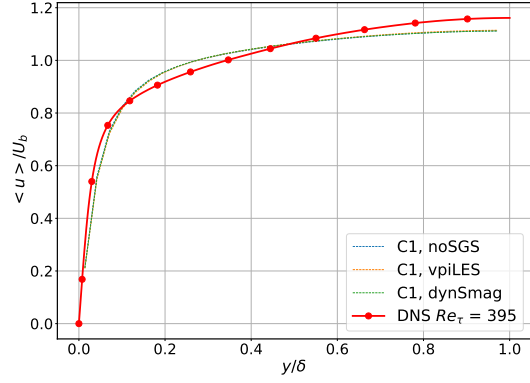
(b) Mean velocity profile, global coordinate

Figure 6.13: Validation of VπLES in comparison with dynamic Smagorinsky model and without turbulence model on grid C1.
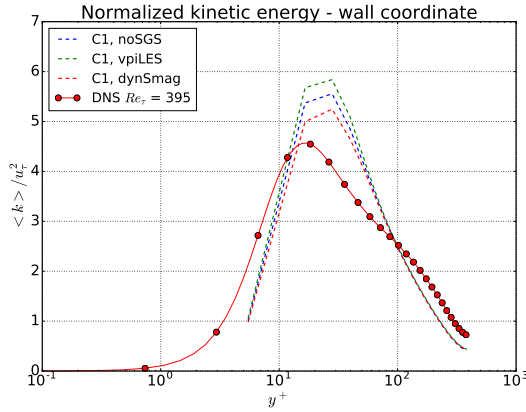
(a) Normalized kinetic energy
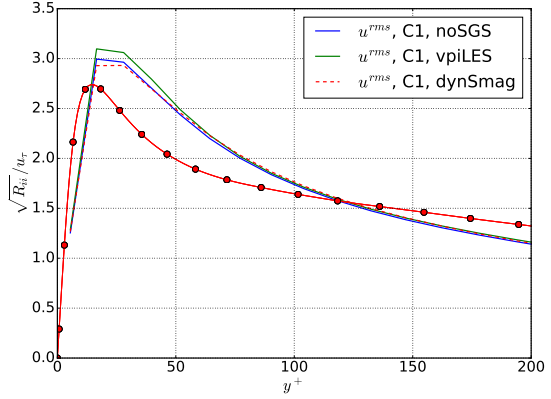
(b) Reynolds stress normalized by friction velocity

Figure 6.14: Validation of VπLES in comparison with dynamic Smagorinsky model and without turbulence model on grid C1.

6.3.2 Power spectral density of resolved fluctuations with under-resolved grid

Fig. (6.15) shows the power spectral density of the resolved fluctuations in coarse grid C1 with VπLES method (black lines) compared with LES with dynamic Smagorinsky model (red lines). It is clear that VπLES method can improve the power spectral density at high frequency scales through modeling them with Lagrangian vortex particles. The small scale entities are preserved from excessive artificial viscosity of grid C1 while in case of LES with dynamic Smagorinsky model there is a huge overdissipation of energy. In Fig. (6.15.a) the energy of fluctuations caused by vertical velocity component is larger than that in the other velocity components due to an improper vortex-wall interaction. Actually for vortex wall interaction no new model is developed in this thesis and the simple rebounding model developed in OpenFOAM for particle laden flows was used. In this case the vortex particle after collision with the wall still exists in the computational domain and keeps its entity. As we go far away from the wall the VπLES method shows the isotropic behavior in energy of velocity fluctuation components. Fig. (6.16) shows the results of energy content of different scales with VπLES method and grid C1 in comparison with high resolution LES with grid C3. At large and intermediate scales the result of VπLES is similar to LES while at very high frequency motions VπLES method preserves structures from artificial viscosity of grid. LES with

dynamic Smagorinsky model in high resolution grid C3 can resolve energy content of small scales in the cost of much higher computational cost.

(a) $y^+ = 10$

(b) $y^+ = 40$

(c) $y^+ = 150$

(d) $y^+ = 392$
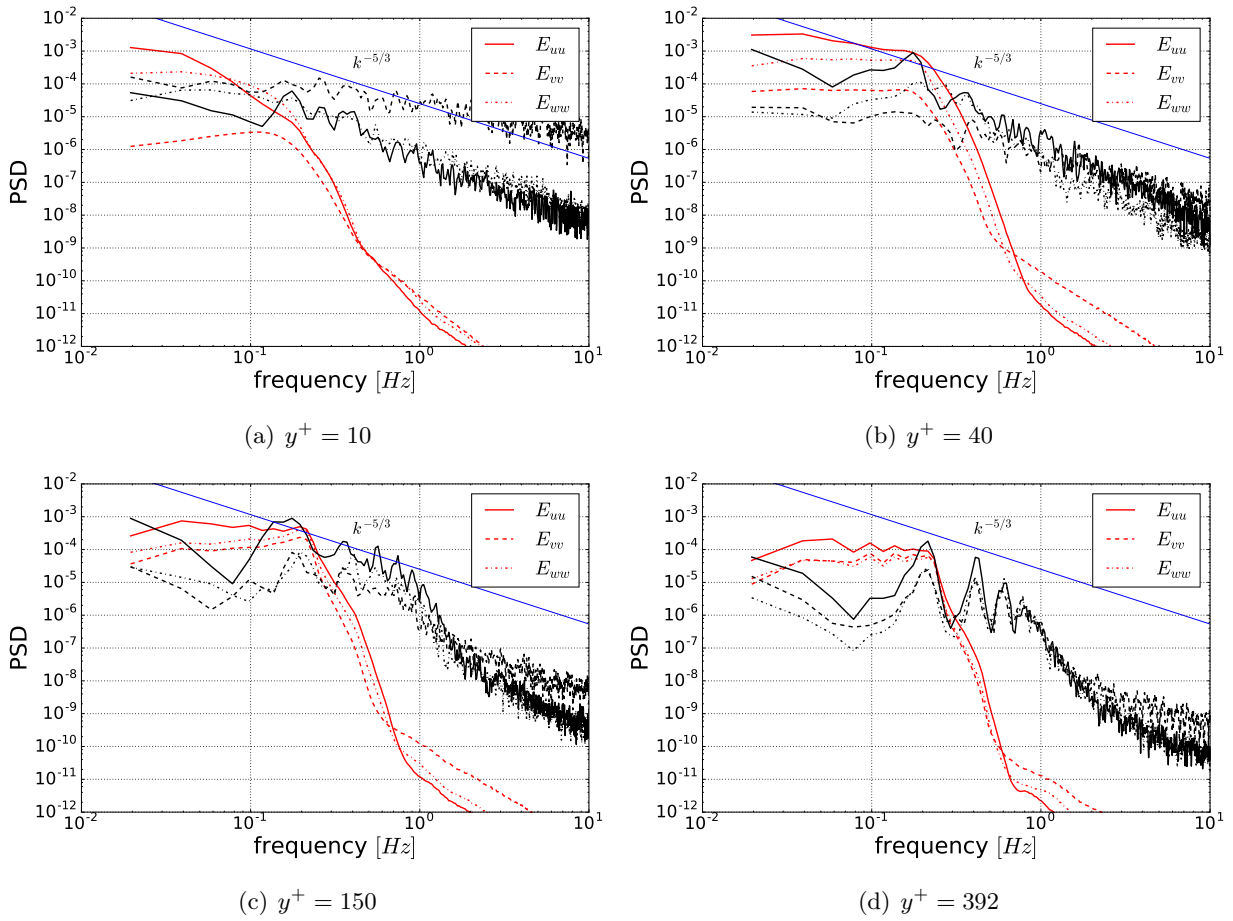
Figure 6.15: Power Spectral Density of the resolved fluctuation (Welch method), under-resolved DNS, C1. Black lines show VπLES method and red line corresponds to LES with dynamic Smagorinsky model.
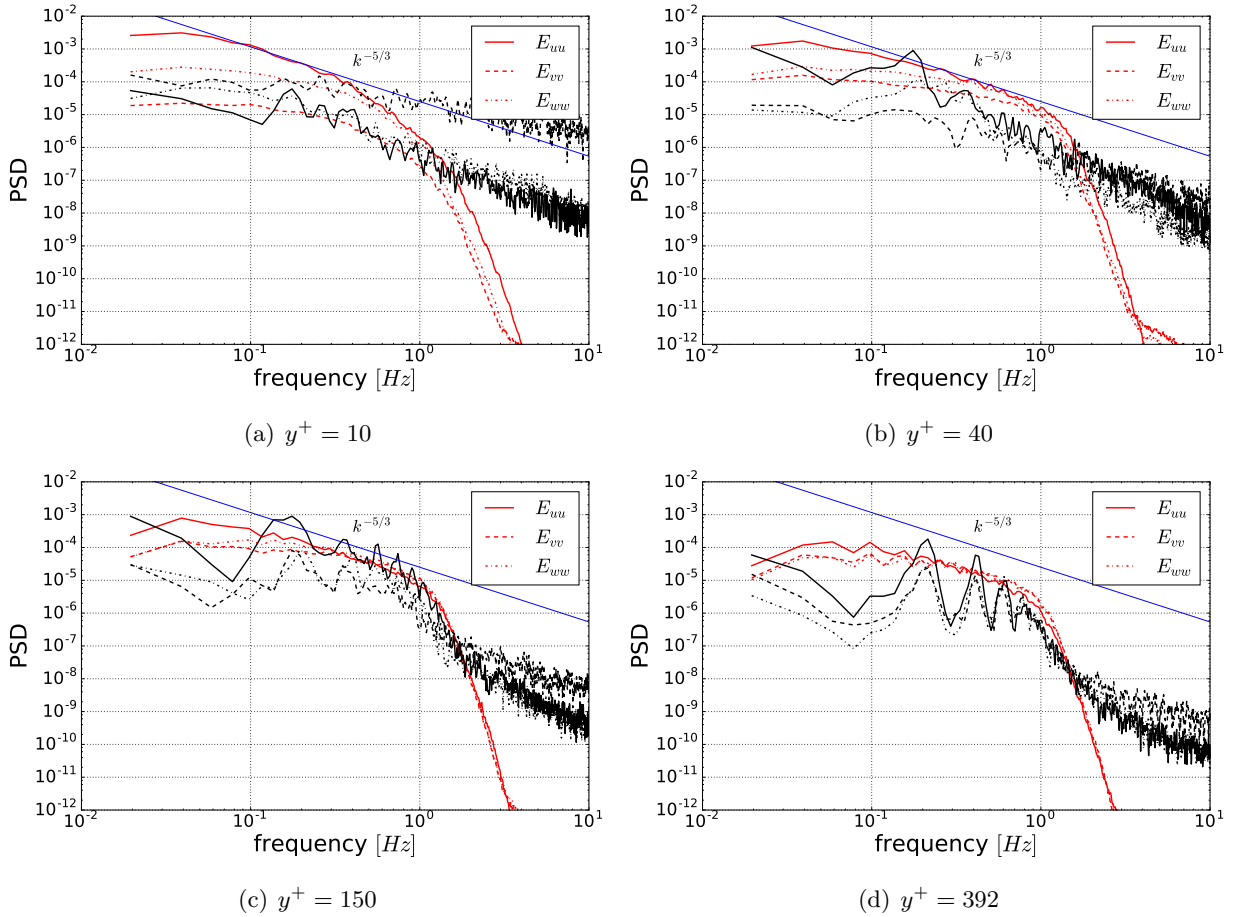
Figure 6.16: Black lines show VπLES with grid C1 and red line corresponds to high resolution LES with grid C3.

6.4 Summary

In this chapter the potential of VπLES method for simulation of wall-bounded flow has been investigated. First a high resolution grid-based simulation was performed in order to compare with DNS of [110] and to find a proper numerical set up as well as to post-process the turbulence statistics in the channel flow simulation. The validation of VπLES has been done for under-resolved grid C1. In case of mean velocity profile VπLES does not show any influence in the velocity profile. Simulations with LES dynamic Smagorinsky model as well as no turbulence model with grid C1 also have similar results. In the other world using LES or VπLES or no SGS model results in a very similar normalized velocity profile in the inner region of boundary layer. It can be concluded that the influence of coupling term $\overline{\mathbf{u}^v \times \boldsymbol{\omega}^g}$ is negligible in mean velocity profile. In case of turbulent kinetic energy, VπLES shows slightly larger value for kinetic energy and Reynolds stress components in comparison with both LES and the case without SGS model. VπLES treats small scale fluctuations in a Lagrangian way and preserves their entities resulting in larger value of kinetic energy. Fig. (6.15) and (6.15) show the superior potential of VπLES method in resolving energy content in the range of high frequencies even in the present huge overdissipation of coarse grid C1 while dynamic Smagorinsky model fails to reproduce energy at small scales. Using VπLES in applications in which the presence of small scales close to the wall play an important role would be beneficial. In order to improve the VπLES method for wall-bounded flows a physical model for vortex particle wall collision must be developed for further investigations.

7 Application of VπLES technology for LES inlet condition

Application of Large Eddy Simulation (LES) requires a turbulent content in inlet conditions for the velocity field. There are various methods to generate inlet turbulent fluctuatuons with reproduction of the first and second order statistics, integral lengths, with account for the divergence free constraint, etc. The problem arises if the typical scales of the turbulent inlet velocity field are comparable with the cell sizes of the grid in front of the area of computational interest, for instance in front of a body. In this case, the turbulent fluctuations are quickly damped (diffused) by numerical or artificial viscosity of numerical methods and the turbulence does not reach the body of interest. Section (7.1) demonstrates that the decay of the inlet turbulence depending on the ratio between the integral length of the turbulence L and the cell size Δ. It was shown that if $L \sim \Delta$ the turbulent kinetic energy decays rapidly downstream. A trivial way to overcome this difficulty is to use very fine grids starting from the inlet to the body of interest. This is surely not a proper way because the distance between the body and the inlet should be large enough to exclude the inlet boundary location influence on the body. Especially it is important if the flow experiences some transformations between the inlet and the body, for instance due to formation of waves in ship hydromechanics. In this case, the distance between the inlet and the ship should be about two ship lengths. Using high resolution gird along this distance would result in over-sized impractical grids. An alternative way is the injection of the fluctuations inside the computational domain directly in front of the body (see Fig. (7.1)). This way is quite effective and useful if the location of the inlet turbulence is known, for instance, it is distributed uniformly within the whole cross section of the computational domain or its part. If the turbulence appearing in front of the body is transformed before it meets the body this approach is not applicable. A typical sample of such a problem could be the simulation of interaction between the turbulence generated by any small bodies and a large body located downstream of small bodies.
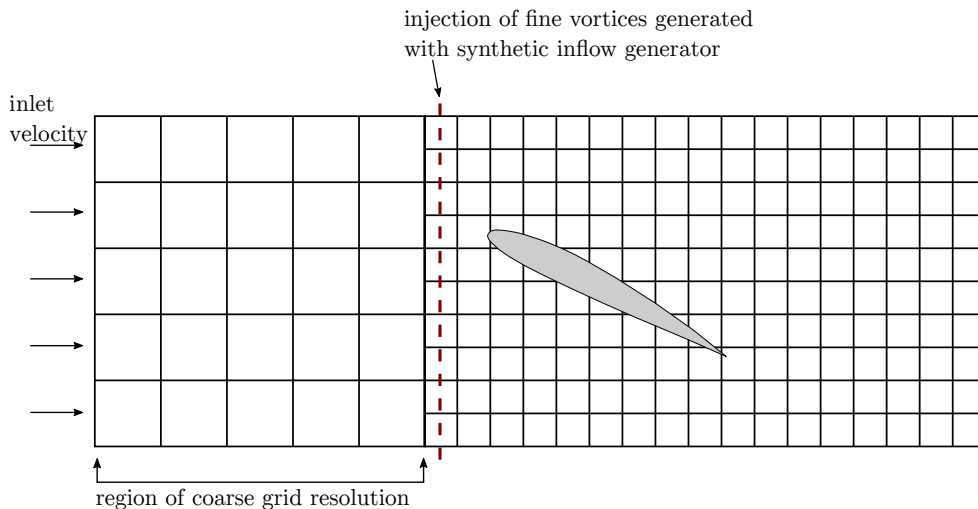
Figure 7.1: Schematic view of the injection of synthetic fluctuations inside computational domain in front of the body of interest.

7.1 Decay of fine scale inlet turbulence on coarse grids

Fig. (7.2) shows decay of the inlet isotropic turbulence downstream in a rectangular domain with cyclic boundary conditions at the lateral boundaries. The inlet velocity is $10[m/s]$. The inflow generator boundary condition is used at the inlet of computational domain (see [113] for details of inflow generator BC) and a usual pressure boundary condition is applied in the outlet. The dependence of turbulent kinetic energy decay on the ratio of integral length scale to cell size is presented in Fig. (7.2). In case of $L/\delta \leq 2$ a very pronounced initial drop in turbulence kinetic energy is observed. Increasing the length scale of synthetic fluctuation to the values above $L/\delta > 4$

is a one way to slow down the rate of the turbulence decay. This is not always a proper solution since large value for length scale may not be physical and does not fulfill the measurement conditions at the inlet. In order to preserve generated fine vortices for a longer distance inside computational domain they are represented by set of vortex particles and convected with the Lagrangian approach. To achieve this strategy it is proposed to use a VπLES method in combination with synthetic inflow generator. The next section describes the application of VπLES for convection of artificial fine vortices from location of injection to the location of interest as well as some preliminary result.
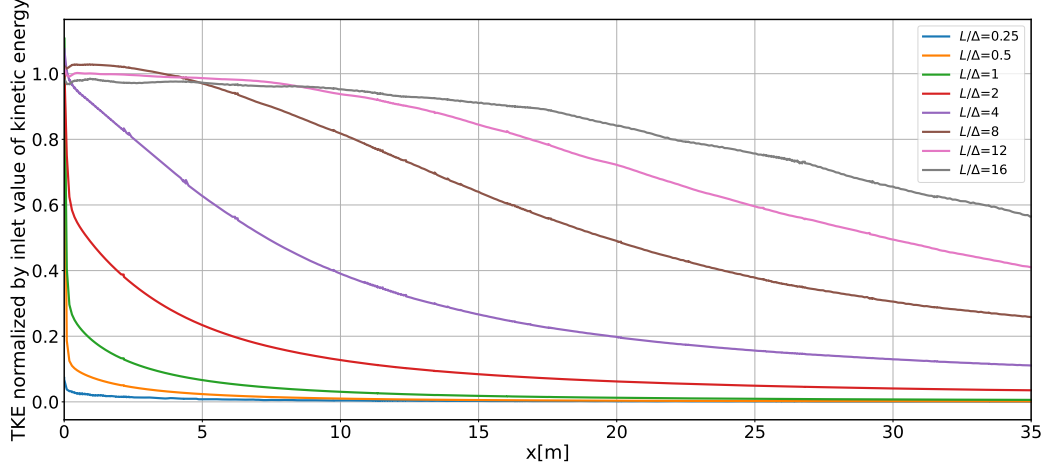
Figure 7.2: The influence of the ratio of integral length scale to cell size on the decay of turbulent kinetic energy (TKE).

7.2 Using VπLES for transport small scale structures on coarse grid

The inlet conditions are usually formulated at a real distance from the main body of interest. In the area between the inlet and the body VπLES method is applied. Fine vortices are generated on a part of the inlet using synthetic inflow generator. Fine vortices are modeled directly by vortex particles and convected toward the body of interest without disappearing due to less numerical diffusivity of VπLES . The influence of fine vortices on the grid solution is taken into account by the term $\overline{\mathbf{u}^v \times \boldsymbol{\omega}^g}$. The flow in front of the body is almost potential $\boldsymbol{\omega}^g = 0$. Therefore, the term $\overline{\mathbf{u}^v \times \boldsymbol{\omega}^g}$ is almost zero (it is not exactly zero because of approximation errors) and don't have a serious effect. In this approach the grid size in the region of computational domain in front of the immersed body can be larger than the grid around and in the wake of the body of interest. Fig. (7.3) presents an overview of the proposed algorithm. Modeling fine vortices with vortex particles and its negligible artificial viscosity makes it possible to use much coarse grid in the inlet region.
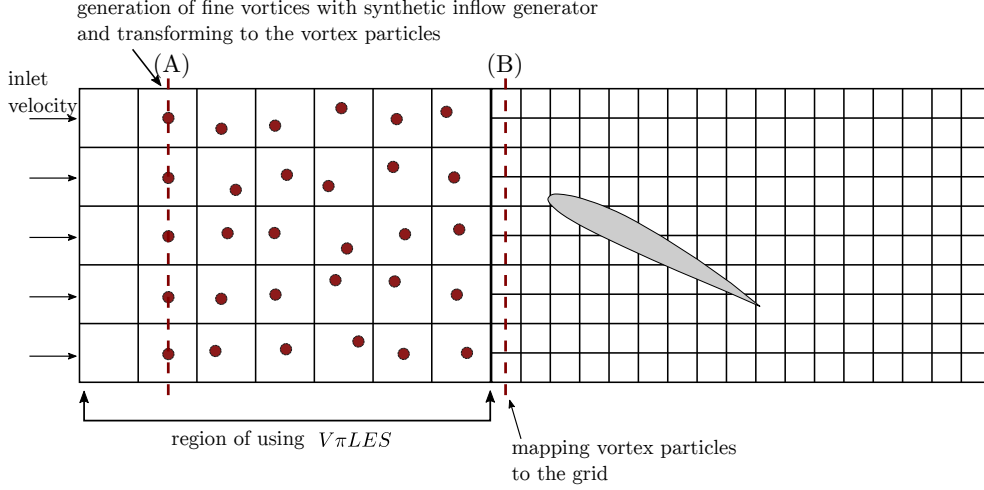
Figure 7.3: Schematic view using VπLES method alongside with synthetic inflow generator for convection of small scale turbulent structures on coarse grid.

7.3 Transporting turbulent contents to a far distance from the injected cross section

In this section the preliminary result of transporting the fine scale structures with corresponding area averaged kinetic energy equal to $1[m^2/s^2]$ from cross section A to cross section B is presented. The aim of using VπLES in this application is to transport fine scale motions with the minimum artificial viscosity imposed by grid and numerical schemes. In this configuration all random vortex particles generated in cross section A are treated in Lagrangian vortex method framework (see Eq. (3.13)) and are convected based on Eq. (3.30) to cross section B. At cross section B all vortex particles mapped back to the grid. In this algorithm mapping particles to grid includes first calculation of induced velocity by particles on surrounding cell centers then deleting them from computational domain. The influence of coupling term $\overline{\mathbf{u}^v \times \boldsymbol{\omega}^g}$ is negligible since $\boldsymbol{\omega}_g \approx 0$ in this uniform flow. This technology was implemented in to the OpenFOAM and some preliminary result was post-processed. Fig. (7.4) represents the induced velocity field of fine vortices $\mathbf{u}^v$ in cross sections A and B. The resultant turbulent kinetic energy from each velocity fluctuating filed in A and B are equal. Fig. (7.5) shows the convection of the generated fine scales in cross section A with Lagrangian vortex particles (or vortex blobs) to cross section B. At cross section B the vortex particles are deleted from computational domain. Figs. (7.6) and (7.7) shows the transporting of fine vortical structures visualized by Q criterion. The fine structures are convected from A to B without being influenced by the artificial viscosity of the grid scheme. Right after section B remarkable dissipation of fine scale structures is visible. In Fig. (7.8) the decay of TKE in grid-based and grid-free domain was shown by blue and red line respectively. It is shown that treating fine scales in the Eulerian grid-based approach results in a fast decay of turbulent kinetic energy especially when the size of fluctuating structures is close to the grid size. On the contrary application of VπLES allows one to keep the initial turbulence almost unchanged on a big distance.

98
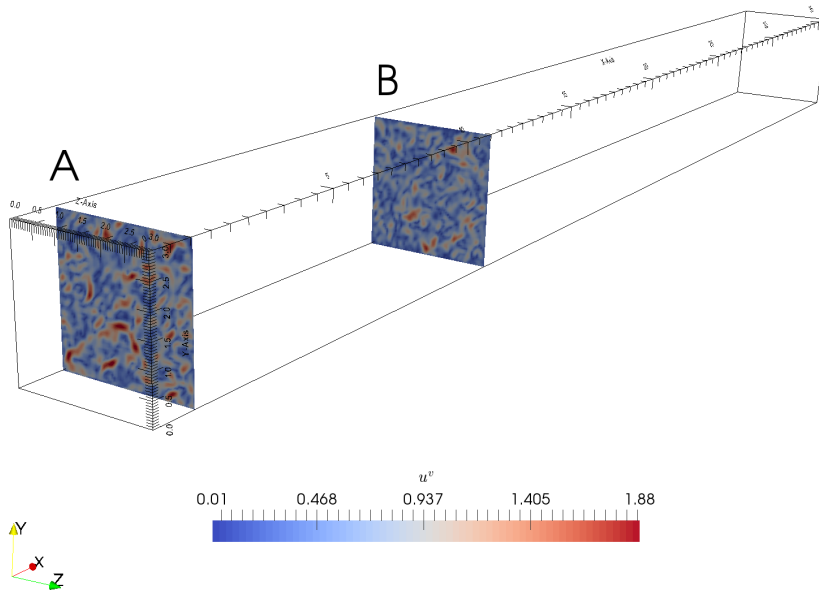
Figure 7.4: Field of velocity induced by concentrated vortex structures represented by vortex particles.
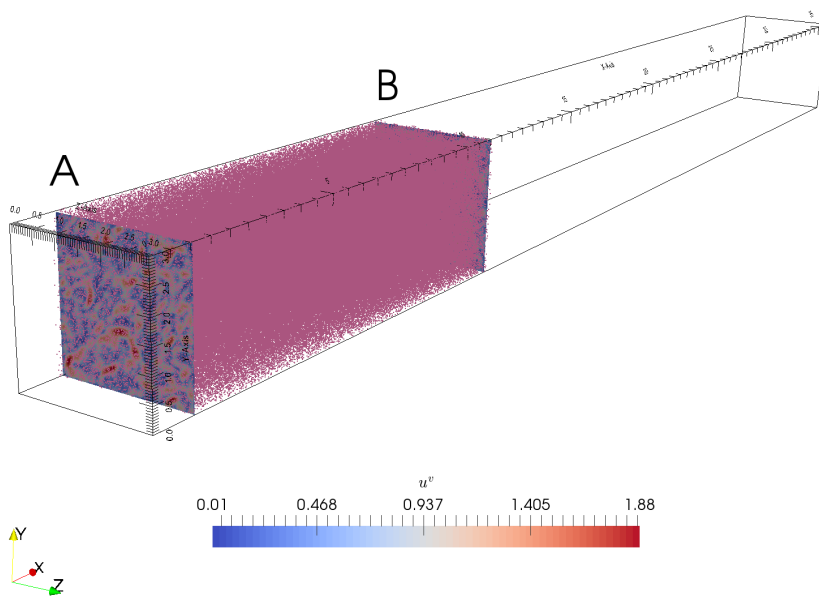
Figure 7.5: Visualization of small scale fluctuating structures in Lagrangian framework with vortex particles.
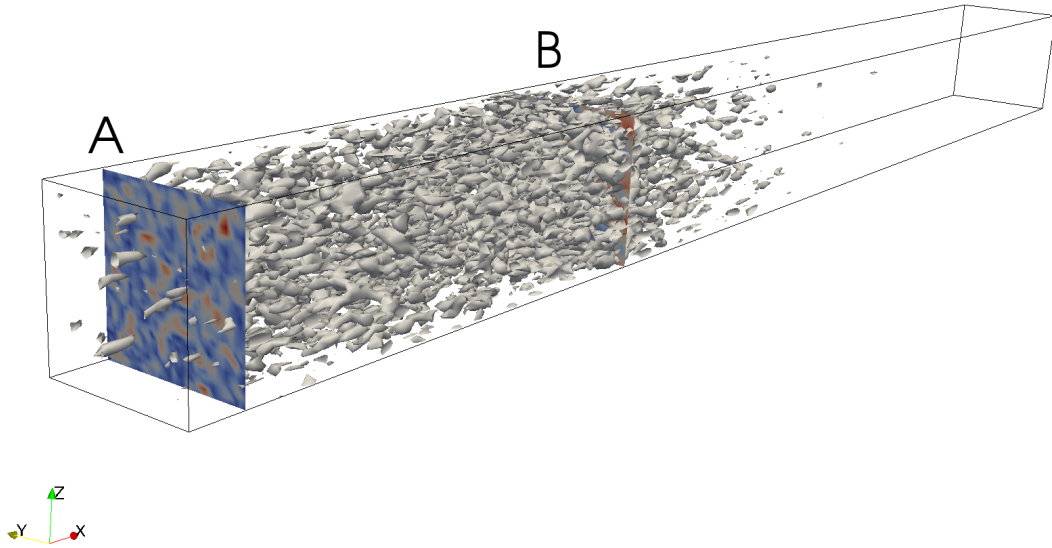
Figure 7.6: Visualization of flow structures in total velocity field ($\mathbf{u}^v + \mathbf{u}^g$) with Q criterion.
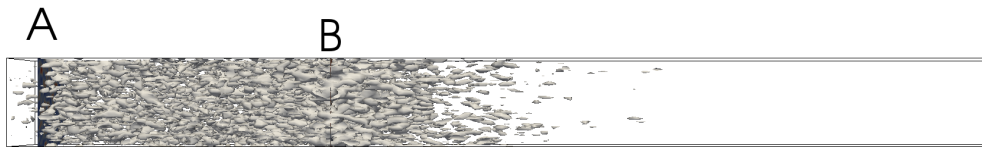
Figure 7.7: Visualization of small scale fluctuating structures. Between section A and B structures are convected in Lagrangian framework using vortex particles and from section B to the outlet only the grid-based simulation is utilized.
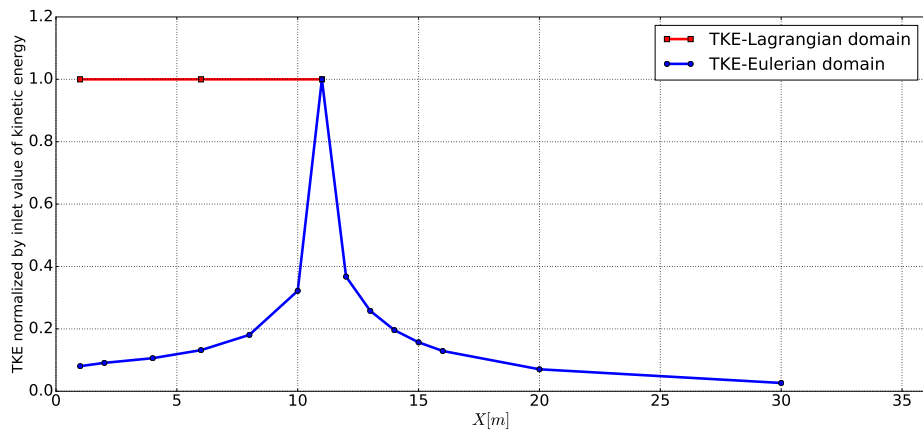
Figure 7.8: Convection of turbulent kinetic energy (TKE) in Lagrangian domain as well as Eulerian (pure grid-based) domain.

7.4   Summary

In this chapter a very short introduction as well as preliminary results of the application of VπLES for transporting the prescribed amount of turbulent contents for LES simulation in coarse grid were presented. In this algorithm Lagrangian part of VπLES method is only active in part of

100

the computational domain which is between the location of injection of synthetic turbulence and the location of interest (e.g. cross section A and B in Fig. (7.3)). The key idea of application of VπLES is preservation of the fine turbulent structures from artificial viscosity effect caused by error of discretization schemes especially for coarse grids. A continuous future work on this topic would be the study of the influence of inlet condition on the aerodynamic performance of airfoils. In this case with VπLES method the desired amount of turbulence intensity imposed at the inlet will convect without any lost of energy to the region close to the airfoil and a real condition of experiment (e.g. [114]) can be reproduced.

8 Conclusion

A novel hybrid grid-based grid-free (Eulerian-Lagrangian) method which is called VπLES was introduced and validated over several benchmark cases including decay of homogeneous isotropic turbulence in box, free turbulent jet and turbulent channel flow. VπLES splits the flow structures as large scale ones, resolved on the grid, and small scale ones, represented by vortex particles. The evolution of both scales is described by a set of two transport equations (see Eqs. (3.12) and (3.13)) which contain the terms describing the dynamic coupling between the scales. The method is simple, straightforward and utilizes advantages of grid-based and grid-free simulations. Vortex methods are suitable for modeling of fine and fast vortices because they possess a low artificial viscosity, a typical side effectof grid-based methods, keep vortex particles from excessive diffusion and has less restrictions to Courant number. Thus, a relatively high resolution of the flow can be attained at coarse grids.

The method is considered as a LES with direct resolution of the subgrid motion represented by vortex particles. The model of the subgrid motion reproduces the energy transfer from fine vortices represented by particles to large scale ones modeled on the grid. In terms of LES it can be interpreted as the energy back scattering which occurs for example in the mixing layer at the jet border. In the laminar flows the vortex particle influence is automatically switched off because of reduction of vortex particles population and weakening their strengths in the smooth laminar velocity fields. The Reynolds stress of the velocity field induced by particles possesses the pronounced anisotropy which is space dependent. The physics behind this anisotropy is to be explained in the future works of the authors by a more thorough study of vortex particles distributions and their orientations.

Choice of the scheme (free) parameters is studied and discussed in section (5.3). As already mentioned one of the weaknesses of many particle based Lagrangian methods is the presence of free parameters which are often tuned to match desirable results if the latter are known before simulations. Scheme parameters are an inherent part of every numerical technique including grid based ones. Their presence does not cause objections if there exists certain rules for their choice. VπLES has two parameters which choice could cause difficulties. The first parameter is the number of particles per cell N_{pt}. Theoretically, N_{pt} should be as large as possible. Practically, it is restricted to perform the solution in a reasonable computational time. Fortunately, Figs. (4.21) and (5.12) show that increase of N_{pt} does not change the results significantly. The value $N_{pt} = 4$ seems to be sufficient to attain a proper accuracy. The second important parameter is the threshold $\lambda_{ci,min}$ used for the vortex particle identification. The recommendation is to set $\lambda_{ci,min}$ being equal to $\approx 5\%$ of the mean λ_{ci}, i.e. $\lambda_{ci,min} = 0.05\lambda_{ci,mean}$ (more discussion is available in section (5.3)).

The VπLES model can be sufficiently reduced by neglecting the inner interaction between particles. In VπLES method the calculation of velocity induced by particle on each other $\mathbf{u}^v$ is the largest time consuming part of computational cost. The results obtained for decay of turbulence in box shows that the inner interaction between particles is neglected and they are driven only by the grid-based flow (see Fig. (4.20)). In case of free turbulent jet flow vortex particles serve just as triggers of turbulence and their inner interaction does not contribute sufficiently to the flow evolution. This results in a very efficient and fast computational procedure.

A very important conclusion of validation is that the spatially averaged term $\overline{\mathbf{u}^v \times \boldsymbol{\omega}^g}$ which describes the influence of fine scales on large ones, behaves as an energy drain transferring the energy of the grid based motion into the fine scales energy. At coarse resolutions, it acts as a diffusive LES subgrid model resulting in a LES-like behavior of the whole method. When the resolution increases, the present method is consistent and converges to the DNS. In section (4.8) it was shown that the VπLES method is capable of resolving scales much less than the grid cell size. In such a way, very fine scales can be resolved on coarse grids.

The potential of VπLES method for simulation of wall-bounded flow has been investigated in chapter (6). The resolved velocity profile in the inner region of boundary layer using VπLES method, LES with dynamic Smagorinsky and case without SGS model result in a very similar normalized mean velocity profile while VπLES shows slightly larger value for kinetic energy and Reynolds stress components in comparison with other two cases (see Fig. (6.14)). VπLES treats small scale fluctuations in a Lagrangian way and preserves their entities resulting in larger value of kinetic energy. Fig. (6.15) and (6.15) show the superior potential of VπLES method in resolving energy content in high frequency scales even in the present huge over dissipation of coarse grid while dynamic Smagorinsky model fails to reproduce energy at small scales. Using VπLES in applications in which the presence of small scales close to the wall play an important role would be beneficial. In order to improve the VπLES method for wall-bounded flows a more advanced model for vortex particle generation and interaction with wall must be developed in future works.

A preliminary result of the application of VπLES for transporting the prescribed amount of turbulent contents for LES simulation in coarse grid were also presented and discussed briefly. In this proposed algorithm Lagrangian part of VπLES method only active in part of the computational domain from the location of injection of synthetic turbulence to the location of interest. The key idea of application of VπLES method is preservation of the fine turbulent structures from artificial viscosity effect caused by error of discretization schemes especially for coarse grids. With VπLES method the desired amount of turbulence intensity imposed at the inlet will convect without any lost of energy to the region close to the object of interest and a real conditions of measurement can be reproduced.

The estimation of computational time for VπLES method was performed for the one-processor computations. For the same grid, the resolution of the subgrid motion proposed in the VπLES method increases the computational time in comparison with LES remarkably. For instance, the computational time of one time step on the grid with 32^3 points is 0.123 s for the simulation without turbulence model, 0.14s for the LES simulation with Smagorinsky model and 0.563 s for the hybrid simulation with passive vortons (without inner interaction) and two particles per cell $N_{pt} = 2$. These results look at first glance, perhaps, pessimistic. However, one has to bear in mind the following considerations. First, resolution of additional scales requires additional computational costs. As shown in Fig. (4.19) for the grid 64^3 the VπLES approacha resolved structures with sizes ten times less than the cell size, 0.1Δ. Resolution of these structures using a pure grid method using only four cells per structure would require $64^3 \times ((\Delta/(0.1\Delta))^3 \times 4^3) = 1.7 \times 10^{10}$ cells. Second, and this is a very important note, one has to compare the computational costs of two simulations with the same level of accuracy. For instance, in section the accuracy of VπLES approach with 1.5×10^5 cells is the same as that of LES with 6Mio cells (see Fig. (5.11)), whereas the LES with the same resolution is fully improper. The computational time for one time step using LES with 6 Mio is 65 s whereas VπLES method requires only 3.2 s (i.e. the speed up factor is around 20). Certainly, the parallelization will change this ratio because the finite volume method and vortex method have different parallelization efficiency.

References

[1] N. Kornev and G. Jacobi, "Development of a hybrid approach using coupled grid-based and grid-free methods," in *MARINE V: proceedings of the V International Conference on Computational Methods in Marine Engineering*, pp. 255–265, CIMNE, 2013.

[2] Ž. Tuković and H. Jasak, "A moving mesh finite volume interface tracking method for surface tension dominated interfacial fluid flow," *Computers & fluids*, vol. 55, pp. 70–84, 2012.

[3] B. Egilsson, "Hybrid vortex models in 2d: Arbitrary moving bodies," 2015.

[4] M. Ould-Salihi, G. Cottet, and M. El Hamraoui, "Blending finite-difference and vortex methods," *SIAM J. Sci. Comput.*, vol. 22, no. 5, pp. 1655–1674, 2000.

[5] J. Monaghan, "Extrapolating b splines for interpolation," *Journal of Computational Physics*, vol. 60, no. 2, pp. 253–262, 1985.

[6] L. Davidson and M. Billson, "Hybrid les-rans using synthesized turbulent fluctuations for forcing in the interface region," *International journal of heat and fluid flow*, vol. 27, no. 6, pp. 1028–1042, 2006.

[7] S. Russ and P. Strykowski, "Turbulent structure and entrainment in heated jets: The effect of initial conditions," *Physics of Fluids A: Fluid Dynamics*, vol. 5, no. 12, pp. 3216–3225, 1993.

[8] K. Zaman and A. Hussain, "Turbulence suppression in free shear flows by controlled excitation," *Journal of Fluid Mechanics*, vol. 103, pp. 133–159, 1981.

[9] A. F. Hussain and K. Zaman, "The 'preferred mode'of the axisymmetric jet," *Journal of fluid mechanics*, vol. 110, pp. 39–71, 1981.

[10] S. Cho, J. Yoo, and H. Choi, "Vortex pairing in an axisymmetric jet using two-frequency acoustic forcing at low to moderate strouhal numbers," *Experiments in Fluids*, vol. 25, no. 4, pp. 305–315, 1998.

[11] P. Sagaut, *Large eddy simulation for incompressible flows: an introduction.* Springer Science & Business Media, 2006.

[12] J. Fröhlich, *Large Eddy Simulation turbulenter Strömungen.* Springer, 2006.

[13] S. B. Pope and S. B. Pope, *Turbulent flows.* Cambridge university press, 2000.

[14] G. Cottet and P. Koumoutsakos, *Vortex Methods: Theory and Practice.* Cambridge University Press, 2000.

[15] C. Mimeau, *Conception and implementation of a hybrid vortex penalization method for solid-fluid-porous media: application to the passive control of incompressible flows.* PhD thesis, Université Grenoble Alpes (ComUE), 2015.

[16] C. Mimeau and I. Mortazavi, "A review of vortex methods and their applications: From creation to recent advances," *Fluids*, vol. 6, no. 2, p. 68, 2021.

[17] k. Kuji and K. Fukuda, "Numerical investigation on unsteady motion and deformation of vortical structures on an accelerated decelerated airfoil using a grid-free vortex method," in *7th Int. Conf. Vortex Flows and Vortex Models*, Rostock, Germany, 2016.

[18] A. Setukha, "On the vortex method for modeling a separated flow of an inviscid fluid," in *9th Int. Conf. Vortex Flow Mechanics*, Patras, Greece, 2021.

[19] I. K. Marchevsky and G. A. Shcheglov, "Efficient semi-analytical integration of vortex sheet influence in 3d vortex method," in *PARTICLES V: proceedings of the V International Conference on Particle-Based Methods: fundamentals and applications*, pp. 703–714, CIMNE, 2017.

[20] K. Kuzmina, I. Marchevsky, I. Soldatova, and Y. Izmailova, "On the scope of lagrangian vortex methods for two-dimensional flow simulations and the pod technique application for data storing and analyzing," *Entropy*, vol. 23, no. 1, p. 118, 2021.

[21] G. Dynnikova, "Calculation of pressure, force, and moment in meshless vortex methods," in *9th Int. Conf. Vortex Flow Mechanics*, Patras, Greece, 2021.

[22] S. Santoso, J.-B. Lagaert, G. Balarac, and G.-H. Cottet, "An hybrid particle/finite-volume method for the study of differential diffusion," 2021.

[23] D.-G. Caprace, G. Winckelmans, and P. Chatelain, "Assessment of the vortex particle-mesh method for efficient les of hovering rotors and their wakes," in *AIAA Scitech 2021 Forum*, p. 0738, 2021.

[24] P. Koumoutsakos, "Multiscale flow simulations using particles," *Annu. Rev. Fluid Mech.*, vol. 37, pp. 457–487, 2005.

[25] P. Chatelain, A. Curioni, M. Bergdorf, D. Rossinelli, W. Andreoni, and P. Koumoutsakos, "Billion vortex particle direct numerical simulations of aircraft wakes," *Computer Methods in Applied Mechanics and Engineering*, vol. 197, no. 13-16, pp. 1296–1304, 2008.

[26] A. Gharakhani, "A high-order flux reconstruction method for 2-d vorticity transport," in *Fluids Engineering Division Summer Meeting*, vol. 85284, p. V001T02A018, American Society of Mechanical Engineers, 2021.

[27] A. Selle, N. Rasmussen, and R. Fedkiw, "A vortex particle method for smoke, water and explosions," *Journal ACM Transactions on Graphics (TOG) - Proceedings of ACM SIGGRAPH*, vol. 24, no. 3, pp. 910–914, 2005.

[28] A. J. Chorin and P. S. Bernard, "Discretization of a vortex sheet, with an example of roll-up," *Journal of Computational Physics*, vol. 13, no. 3, pp. 423–429, 1973.

[29] A. J. Chorin, "Vortex sheet approximation of boundary layers," *Journal of computational physics*, vol. 27, no. 3, pp. 428–442, 1978.

[30] M. Coquerelle and G.-H. Cottet, "A vortex level set method for the two-way coupling of an incompressible fluid with colliding rigid bodies," *Journal of Computational Physics*, vol. 227, no. 21, pp. 9121–9137, 2008.

[31] C. Mimeau, I. Mortazavi, and G.-H. Cottet, "A vortex penalization method for low and moderate reynolds number flows," in *Int. Conf. Vortex Flows and Vortex Models*, Rostock, Germany, 2016.

[32] C. Bernier, M. Gazzola, and R. Ronsse, "Coupling a vortex particle-mesh method to a multibody system solver for the simulation of articulated swimmers," in *7th Int. Conf. Vortex Flows and Vortex Models*, Rostock, Germany, 2016.

[33] J. Wu, "Numerical boundary conditions for viscous flow problems," *AIAA Journal*, vol. 14, no. 8, pp. 1042–1049, 1976.

[34] P. Koumoutsakos, A. Leonard, and F. Pepin, "Boundary conditions for viscous vortex methods," *Journal of Computational Physics*, vol. 113, no. 1, pp. 52–61, 1994.

[35] K. S. Kuzmina and I. K. Marchevsky, "On the efficiency of tangential components of the velocity boundary condition satisfaction in vortex method for 2d flows simulation," in *7th Int. Conf. Vortex Flows and Vortex Models*, Rostock, Germany, 2016.

[36] I. K. Marchevsky and G. A. Shcheglov, "The numerical scheme for tangential components of the velocity boundary condition satisfaction on 3d bodies in vortex method," in *7th Int. Conf. Vortex Flows and Vortex Models*, Rostock, Germany, 2016.

[37] A. A. Aparinov and A. V. Setukha, "Solution of aerodynamic problems of moving objects with vortex method," in *7th Int. Conf. Vortex Flows and Vortex Models*, Rostock, Germany, 2016.

[38] G. Daeninck, *Developments in hybrid approaches: vortex method with known separation location; vortex method with near-wall Eulerian solver; RANS-LES coupling.* PhD thesis, UCL-Université Catholique de Louvain, 2006.

[39] M. Stock, A. Gharakhani, and C. Stone, "Modeling rotor wakes with a hybrid overflow-vortex method on a gpu cluster," in *28th AIAA applied aerodynamics conference*, p. 4553, 2010.

[40] G. Winckelmans, P. Chatelain, Y. Marichal, P. Parmentier, M. Duponcheel, D.-G. Caprace, , and T. Gillis, "Recent developments in vortex particle-mesh (vpm) methods and applications," in *7th Int. Conf. Vortex Flows and Vortex Models 2016*, p. 16, 2016.

[41] G.-H. Cottet and P. Poncet, "Advances in direct numerical simulations of 3d wall-bounded flows by vortex-in-cell methods," *Journal of Computational Physics*, vol. 193, no. 1, pp. 136–158, 2004.

[42] M. El Ossmani and P. Poncet, "Efficiency of multiscale hybrid grid-particle vortex methods," *Multiscale modeling & simulation*, vol. 8, no. 5, pp. 1671–1690, 2010.

[43] A. J. Chorin, "Constrained random walks and vortex filaments in turbulence theory," *Communications in mathematical physics*, vol. 132, no. 3, pp. 519–536, 1990.

[44] S. Reboux, B. Schrader, and I. F. Sbalzarini, "A self-organizing lagrangian particle method for adaptive-resolution advection–diffusion simulations," *Journal of Computational Physics*, vol. 231, no. 9, pp. 3623–3646, 2012.

[45] C. Häcki, S. Reboux, and I. F. Sbalzarini, "A self-organizing adaptive-resolution particle method with anisotropic kernels," *Procedia IUTAM*, vol. 18, pp. 40–55, 2015.

[46] G.-H. Cottet and P. Koumoutsakos, "High order semi-lagrangian particle methods," in *Spectral and High Order Methods for Partial Differential Equations ICOSAHOM 2016*, pp. 103–117, Springer, 2017.

[47] G. Winckelmans, P. Chatelain, Y. Marichal, P. Parmentier, M. Duponcheel, D.-G. Caprace, and T. Gillis, "Recent developments in vortex particle-mesh (vpm) methods, and applications," in *7th International Conference on Vortex Flows and Vortex Models (ICVFM 2016)*, 2016.

[48] B. Chen, Z. Wang, and T. Uchiyama, "Numerical simulation of bubble cluster induced flow by three-dimensional vortex-in-cell method," *Journal of Fluids Engineering*, vol. 136, no. 8, 2014.

[49] Y. N. Grigoryev, V. A. Vshivkov, and M. P. Fedoruk, *Numerical" Particle-in-Cell" Methods.* de Gruyter, 2012.

[50] D. C. Wilcox *et al.*, *Turbulence modeling for CFD*, vol. 2. DCW industries La Canada, CA, 1998.

[51] N. Kornev and I. Cherunova, "Lectures on computational fluid dynamics and heat transfer with applications to human thermodynamics," 2014.

[52] L. Davidson, "Fluid mechanics, turbulent flow and turbulence modeling," 2015.

[53] C. G. Speziale, "Analytical methods for the development of reynolds-stress closures in turbulence," *Annual review of fluid mechanics*, vol. 23, no. 1, pp. 107–157, 1991.

[54] G. Biswas and V. Eswaran, *Turbulent flows: Fundamentals, experiments and modeling*. CRC Press, 2002.

[55] B. E. Launder and D. B. Spalding, "The numerical computation of turbulent flows," in *Numerical prediction of flow, heat transfer, turbulence and combustion*, pp. 96–116, Elsevier, 1983.

[56] F. R. Menter, "Performance of popular turbulence model for attached and separated adverse pressure gradient flows," *AIAA journal*, vol. 30, no. 8, pp. 2066–2072, 1992.

[57] H. K. Versteeg and W. Malalasekera, *An introduction to computational fluid dynamics: the finite volume method*. Pearson education, 2007.

[58] K. Hanjalic, "Turbulence and transport phenomena. modelling and simulation," *Lecture Note*, 2005.

[59] C. L. Rumsey, *NASA Langley Research Center, Turbulence Modeling Resource*.

[60] S. Jakirlić and R. Maduta, "Extending the bounds of 'steady'rans closures: Toward an instability-sensitive reynolds stress model," *International Journal of Heat and fluid flow*, vol. 51, pp. 175–194, 2015.

[61] J. Smagorinsky, "General circulation experiments with the primitive equations: I. the basic experiment," *Monthly weather review*, vol. 91, no. 3, pp. 99–164, 1963.

[62] H. Jasak, "Error analysis and estimation for the finite volume method with applications to fluid flows.," 1996.

[63] J. H. Ferziger, M. Perić, and R. L. Street, *Computational methods for fluid dynamics*, vol. 3. Springer, 2002.

[64] F. Moukalled, L. Mangani, and M. Darwish, "The finite volume method in computational fluid dynamics, fluid mechanics and its applications," *Cham: Springer*, vol. 113, 2016.

[65] K. E. Gustafson and J. A. Sethian, *Vortex methods and vortex motion*, vol. 19. SIAM, 1991.

[66] A. Leonard, "Vortex methods for flow simulation," *Journal of Computational Physics*, vol. 37, no. 3, pp. 289–335, 1980.

[67] L. A. Barba, *Vortex Method for computing high-Reynolds number flows: Increased accuracy with a fully mesh-less formulation*. California Institute of Technology, 2004.

[68] A. J. Chorin, *Vorticity and turbulence*, vol. 103. Springer Science & Business Media, 2013.

[69] K. Kuwahara and H. Takami, "Numerical studies of two-dimensional vortex motion by a system of point vortices," *Journal of the Physical Society of Japan*, vol. 34, no. 1, pp. 247–253, 1973.

[70] L. F. Rossi, "Resurrecting core spreading vortex methods: A new scheme that is both deterministic and convergent," *SIAM Journal on Scientific Computing*, vol. 17, no. 2, pp. 370–397, 1996.

[71] R. Yokota, T. Sheel, and S. Obi, "Calculation of isotropic turbulence using a pure Lagrangian vortex method," *J. Comp. Phys.*, vol. 226, pp. 1589–1606, 2007.

[72] A. J. Chorin, "Estimates of intermittency, spectra, and blowup in developed turbulence," 1981.

[73] L. Greengard and V. Rokhlin, "A fast algorithm for particle simulations," *Journal of computational physics*, vol. 73, no. 2, pp. 325–348, 1987.

[74] R. Yokota, T. Narumi, R. Sakamaki, S. Kameoka, S. Obi, and K. Yasuoka, "Fast multipole methods on a cluster of gpus for the meshless simulation of turbulence," *Computer Physics Communications*, vol. 180, no. 11, pp. 2066–2078, 2009.

[75] O. M. Knio and A. F. Ghoniem, "Numerical study of a three-dimensional vortex method," *Journal of Computational Physics*, vol. 86, no. 1, pp. 75–106, 1990.

[76] G.-H. Cottet, "Particle-grid domain decomposition methods for the navier-stokes equations in exterior domains," *Lect. Appl. Math.Ser. Am. Math. Soc. N. Y*, pp. 100–118, 1991.

[77] G.-H. Cottet, P. Koumoutsakos, and M. L. O. Salihi, "Vortex methods with spatially varying cores," *Journal of Computational Physics*, vol. 162, no. 1, pp. 164–185, 2000.

[78] I. Christiansen, "Numerical simulation of hydrodynamics by the method of point vortices," *Journal of Computational Physics*, vol. 13, no. 3, pp. 363–379, 1973.

[79] R. Cocle, G. Winckelmans, and G. Daeninck, "Combining the vortex-in-cell and parallel fast multipole methods for efficient domain decomposition simulations," *Journal of Computational Physics*, vol. 227, no. 21, pp. 9091–9120, 2008.

[80] L. Manickathan, "Hybrid eulerian-lagrangian vortex particle method: A fast and accurate numerical method for 2d vertical-axis wind turbine," 2014.

[81] A. Magni and G.-H. Cottet, "Accurate, non-oscillatory, remeshing schemes for particle methods," *Journal of Computational Physics*, vol. 231, no. 1, pp. 152–172, 2012.

[82] N. Kornev, V. Zhdanov, and E. Hassel, "Study of scalar macro – and microstructures in a confined jet," *International Journal of Heat and Fluid Flow*, vol. 29, pp. 665–674, 2008.

[83] J. T. Beale and A. T. Layton, "A velocity decomposition approach for moving interfaces in viscous fluids," *Journal of Computational Physics*, vol. 228, no. 9, pp. 3358–3367, 2009.

[84] K. A. Bagrinovskii and S. K. Godunov, "Difference schemes for multidimensional problems.," vol. 115, pp. 431–433, 1957.

[85] G. I. Marchuk, "Splitting and alternating direction methods," *Handbook of numerical analysis*, vol. 1, pp. 197–462, 1990.

[86] D. W. Peaceman and H. H. Rachford, Jr, "The numerical solution of parabolic and elliptic differential equations," *Journal of the Society for industrial and Applied Mathematics*, vol. 3, no. 1, pp. 28–41, 1955.

[87] E. Weinan, *Principles of multiscale modeling.* Cambridge University Press, 2011.

[88] N. Kornev, "Hybrid method based on embedded coupled simulation of vortex particles in grid based solution," *Computational Particle Mechanics*, vol. 5, no. 3, pp. 269–283, 2018.

[89] P. Chakraborty, S. Balachandar, and R. J. Adrian, "On the relationships between local vortex identification schemes," *Journal of fluid mechanics*, vol. 535, pp. 189–214, 2005.

[90] N. Kornev and N. Abbas, "Vorticity structures and turbulence in the wake of full block ships," *Journal of Marine Science and Technology*, vol. 23, no. 3, pp. 567–579, 2018.

[91] N. Kornev and S. Samarbakhsh, "Large eddy simulation with direct resolution of subgrid motion using a grid free vortex particle method," *International Journal of Heat and Fluid Flow*, vol. 75, pp. 86–102, 2019.

[92] G. Taylor, "Production and dissipation of vorticity in a turbulent fluid," *Proc. Royal Soc. A.*, vol. 164, no. 916, pp. 15–23, 1938.

[93] K. Fukuda and K. Kamemoto, "Application of a redistribution model incorporated in a vortex method to turbulent flow analysis," *Proc. ICVFM2005, Yokohama, Japan*, pp. 131–136, 2005.

[94] G. Winckelmans and A. Leonard, "Contributions to vortex particle methods for the computation of three-dimensional incompressible unsteady flows," *Journal of Computational Physics*, vol. 109, no. 2, pp. 247–273, 1993.

[95] M. Mosher, "A method for computing three dimensional vortex flows," *Zeitschrift für Flugwissenschaften*, vol. 9, no. 3, pp. 125–133, 1985.

[96] O. Knio and A. Ghoniem, "Numerical study of a three- dimensional vortex method," *J. Comp. Phys.*, vol. 86, pp. 75–106, 1990.

[97] D. Feder, M. Dhone, N. Kornev, and M. Abdel Maksoud, "Comparison of different approaches tracking a wing-tip vortex," *Ocean Engineering*, vol. 147, no. 1, pp. 659–675, 2018.

[98] G. Comte-Bellot and S. Corrsin, "Simple eulerian time correlation of full-and narrow-band velocity signals in grid-generated,'isotropic'turbulence," *Journal of fluid mechanics*, vol. 48, no. 2, pp. 273–337, 1971.

[99] V. Sohm, *Hybrid Turbulence Simulation to Predict Cyclic Variations.* Cuvillier Verlag, 2007.

[100] D. Dietzel, D. Messig, F. Piscaglia, A. Montorfano, G. Olenik, O. T. Stein, A. Kronenburg, A. Onorati, and C. Hasse, "Evaluation of scale resolving turbulence generation methods for large eddy simulation of turbulent flows," *Computers & Fluids*, vol. 93, pp. 116–128, 2014.

[101] R. H. Kraichnan, "Diffusion by a random velocity field," *The physics of fluids*, vol. 13, no. 1, pp. 22–31, 1970.

[102] M. Billson, L.-E. Eriksson, and L. Davidson, "Jet noise prediction using stochastic turbulence modeling," in *9th AIAA/CEAS aeroacoustics conference and exhibit*, p. 3282, 2003.

[103] L. Davidson, "Using isotropic synthetic fluctuations as inlet boundary conditions for unsteady simulations," in *Advances and applications in Fluid Mechanics*, Citeseer, 2007.

[104] T. Saad, D. Cline, R. Stoll, and J. C. Sutherland, "Scalable tools for generating synthetic isotropic turbulence with arbitrary spectra," *AIAA journal*, vol. 55, no. 1, pp. 327–331, 2017.

[105] J. Kim and H. Choi, "Large eddy simulation of a circular jet: effect of inflow conditions on the near field," *Journal of Fluid Mechanics*, vol. 620, pp. 383–411, 2009.

[106] A. Michalke and G. Hermann, "On the inviscid instability of a circular jet with external flow," *Journal of Fluid Mechanics*, vol. 114, pp. 343–359, 1982.

[107] M. Lesieur, *Turbulence in fluids: stochastic and numerical modelling*, vol. 488. Nijhoff Boston, MA, 1987.

[108] S. Samarbakhsh and N. Kornev, "Simulation of a free circular jet using the vortex particle intensified les (vπles)," *International Journal of Heat and Fluid Flow*, vol. 80, p. 108489, 2019.

[109] D. Chung and D. Pullin, "Large-eddy simulation and wall modelling of turbulent channel flow," *Journal of fluid mechanics*, vol. 631, pp. 281–309, 2009.

[110] J. Kim, P. Moin, and R. Moser, "Turbulence statistics in fully developed channel flow at low reynolds number," *Journal of fluid mechanics*, vol. 177, pp. 133–166, 1987.

[111] T. Mukha and M. Liefvendahl, "Large-eddy simulation of turbulent channel flow," tech. rep., Technical Report, 2015.

[112] E. De Villiers, "The potential of large eddy simulation for the modeling of wall bounded flows," *Imperial College of Science, Technology and Medicine*, 2006.

[113] H. Kröger and N. Kornev, "Generation of divergence free synthetic inflow turbulence with arbitrary anisotropy," *Computers & Fluids*, vol. 165, pp. 78–88, 2018.

[114] S. L. Herbst, C. J. Kähler, and R. Hain, "Influence of large-scale free-stream turbulence on an sd7003 airfoil at low reynolds numbers.," in *2018 Applied Aerodynamics Conference*, p. 3490, 2018.

Statutory declaration in lieu of an oath

I hereby declare in lieu of an oath that I have completed the present dissertation entitled "Development and validation of hybrid grid-based and grid-free computational VπLES method" independently and without illegitimate assistance from third parties. I have use no other than the specified sources and aids. In case that the dissertation is additionally submitted in an electronic format, I declare that the written and electronic versions are fully identical. The dissertation has not been submitted to any examination body in this, or similar, form.

Rostock, 23 May 2022   Sina Samarbakhsh